

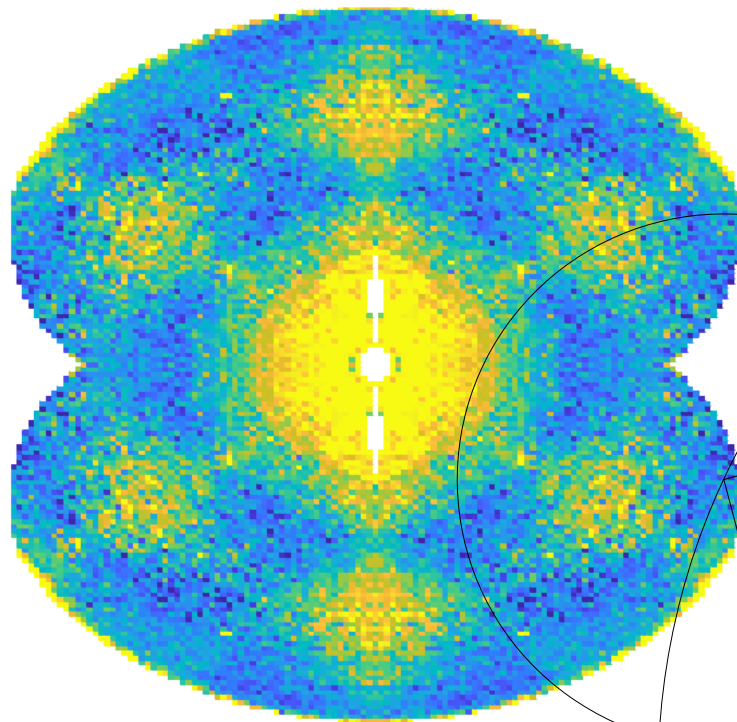


**Master's Thesis in Physics**

Morten Lunn Haubro

---

**Neutron Scattering Studies of Spin Ice  
Material  $\text{Ho}_2\text{Ti}_2\text{O}_7$  Under Uniaxial  
Pressure**



*Supervisors:*

Kim Lefmann, NBI

Pascale Deen, ESS, NBI

*Submitted:* November 30, 2020

---

# Abstract

In this thesis I describe the design process of a uniaxial pressure cell for use in neutron scattering experiments. The cell is optimized for measuring the broad and diffuse magnetic scattering signals that are characteristic of magnetically frustrated compounds. Furthermore, the room temperature and low temperature calibration, of a load gauge for in situ pressure determination, is presented. Neutron measurements demonstrate that the pressure cell has a homogeneous and largely non-magnetic background. The result is a pressure cell with in-situ pressure determination, accurate within 10 %, that is functional up to 3 GPa.

Neutron experiments are performed on the spin ice material  $\text{Ho}_2\text{Ti}_2\text{O}_7$  under uniaxial pressure. Spin ice materials gained interest in the late 20th century for their substantial zero-point entropy and the apparent emergence of magnetic monopole excitations. Previous work has shown that the magnetic susceptibility of the very similar  $\text{Dy}_2\text{Ti}_2\text{O}_7$  has a significant pressure response. New theoretical work suggest that this response is a result of the uniaxial pressure lifting the ground state degeneracy, reducing the size of the ground state manifold.

I show results that, with low statistical significance, are consistent with theory. The peak intensity of the spin flip scattering shows an increased intensity of  $4 \pm 4$  %. Furthermore, the pinch point scattering shows a significant increase as a function of pressure. This change is not predicted by the theoretical model.

# Contents

<b>1</b>	<b>Introduction</b>	<b>1</b>
<b>2</b>	<b>Magnetism</b>	<b>3</b>
2.1	Magnetic Order . . . . .	5
2.1.1	Spin Waves . . . . .	6
2.2	Frustrated Magnetism . . . . .	7
2.3	Spin Ice Materials . . . . .	8
2.3.1	Magnetic Monopoles . . . . .	10
2.3.2	Spin Ice Under Uniaxial Pressure . . . . .	12
2.3.3	Ho <sub>2</sub> Ti <sub>2</sub> O <sub>7</sub> Sample . . . . .	17
<b>3</b>	<b>Neutron Scattering</b>	<b>18</b>
3.1	The Neutron . . . . .	18
3.2	Scattering Theory . . . . .	19
3.3	Nuclear Scattering . . . . .	20
3.4	Magnetic Scattering . . . . .	23
3.4.1	Polarization Analysis . . . . .	26
3.5	D7 - Diffuse Scattering Spectrometer . . . . .	29
<b>4</b>	<b>Uniaxial Pressure Cell</b>	<b>31</b>
4.1	Material Properties . . . . .	31
4.2	Cell Version 1 . . . . .	33
4.3	Cell Version 2 . . . . .	35
4.4	Cell Version 3 . . . . .	37
4.5	Load Gauge . . . . .	39
4.5.1	Room Temperature Calibration . . . . .	41
4.6	Temperature Calibration . . . . .	43
4.6.1	LN <sub>2</sub> Calibration . . . . .	44
4.6.2	CCR Calibration . . . . .	46
4.6.3	High Temperature Drift . . . . .	50

<b>5</b>	<b>Neutron Measurements on HTO with Cell v1</b>	<b>53</b>
5.1	The Simulation . . . . .	55
5.1.1	Fitting . . . . .	57
5.2	Correcting the Data . . . . .	59
5.2.1	Paramagnetic data . . . . .	59
5.2.2	Low Temperature Spin Flip Data . . . . .	60
5.3	Comparing with Theory . . . . .	61
<b>6</b>	<b>Neutron Measurements on HTO with Cell v2</b>	<b>63</b>
6.1	Measuring the Cell Background . . . . .	64
6.2	Low Temperature Spin Flip Data . . . . .	66
6.3	Low Temperature Non Spin Flip Data . . . . .	69
6.4	Paramagnetic Data . . . . .	70
<b>7</b>	<b>Discussion and Outlook</b>	<b>72</b>
7.1	Uniaxial Pressure Cell . . . . .	72
7.1.1	The Load Gauge . . . . .	74
7.2	Ho <sub>2</sub> Ti <sub>2</sub> O <sub>7</sub> Under Pressure . . . . .	74
7.2.1	Magnetisation Measurements . . . . .	75
7.3	Future Projects . . . . .	77
<b>8</b>	<b>Conclusion</b>	<b>79</b>
	<b>Appendices</b>	<b>86</b>
<b>A</b>	<b>List of Publications</b>	<b>86</b>
<b>B</b>	<b>CuBe Properties</b>	<b>87</b>
<b>C</b>	<b>Cell Drawings</b>	<b>88</b>
<b>D</b>	<b>Resistance Calibration</b>	<b>94</b>

# Acknowledgements

First of all I would like to thank my supervisors Pascale Deen and Kim Lefmann for guidance and encouragement throughout the project. Your passion for science is contagious. Second, a huge thank you should also go to Lise Sandberg for inviting me onto the project and being the best co-supervisor/collaborator I could have asked for.

My work has been dependent on a large amount of technical assistance and a large thank you should also go to Malcolm Guthrie and Alexander Holmes at the ESS. For your technical assistance with the testing of the pressure cell and for your patience with my never ending questions, I am very grateful.

At the workshop at NBI, Jan Oechsle, Dennis Wistisen and Keld Theodor has worked tirelessly to improve the cell design, thank you for all your hard work.

I would also like to thank Ingrid Marie Bakke Fjellvåg, Richard Edberg and Patrik Henelius for fruitful discussions at our weekly meetings.

A special thank you should also go to all my office mates from the scattering group for great discussions as well as much needed coffee breaks.

Lastly, a large thank you should go to the Siemens foundation for supporting my project.

# Chapter 1

## Introduction

For more than a century, the study of solid state physics have yielded spectacular result. The discovery of superconductivity [1] and the quantum theory of magnetism [2] heralded in a new era. One where macroscopic phenomena, needed to be understood via quantum interactions at the microscopic scale. The diversity that solid state systems offer, in terms of stable quantum states and emergent phenomena, makes them ideal for testing our understanding of the fundamental principles of our universe.

In more recent years, developments in synthesis methods and measuring techniques has meant that design of quantum devices has become possible. The prospect of quantum computing has driven progress in spintronics and quantum transport [3].

In the world of magnetic research, a lot of work has gone into the investigation of *frustrated magnetism*. Magnetic systems that due to their geometry, has a suppressed ordering temperature. Due to the lack of order, these materials offer a unique opportunity to study short range quantum interactions. They originally gained interest for their suspected connection to high temperature superconductivity [4, 5], Since then, continued studies have revealed that the competing interactions may give rise to long range entanglement and topological states [6].

Around the turn of the 21st century, a number of papers were published on the so called *spin ice* - materials. Frustrated systems that show no long range order down to mK temperatures. The measurement of the substantial, zero point entropy [7] and subsequent evidence of magnetic monopole excitations [8], means that *spin ice* compounds has garnered a lot of attention from the scientific community over the past 20 years [9–11]. In this project I aim to build on this work by studying the spin ice compound  $\text{Ho}_2\text{Ti}_2\text{O}_7$  under uniaxial pressure.

The use of pressure in the study of condensed matter physics has in the past yielded significant results. Pressure as a tuning parameter offers a unique opportunity to change

the structure of a solid at the atomic scale, leading to new phases of matter. Applying pressure can turn insulators metallic or even superconducting. Recently, E. Snider et al. showed evidence of superconductivity at 285 K in a Hydrogen-Sulphur compound at 267 GPa [12]. In the field of magnetism, pressure offers an exciting opportunity to tune the coupling between magnetic moments and induce new phases.

As a probe for studying condensed matter systems, few tools are as versatile as neutron scattering. The unique combination of magnetic moment, no electric charge and an energy scale that matches fundamental excitations makes neutron scattering a powerful tool in material science.

In neutron scattering, high pressure research is dominated almost exclusively by hydrostatic pressure experiments. This is experimentally simpler to realise than uniaxial pressure, as there is no need to consider the Poisson effect and thus the risk of breaking the sample is much smaller. The drawback of this is that hydrostatic pressure is applied symmetrically and is thus, in most cases, incapable of changing the relative distances in the system.

Availability of uniaxial pressure would make it possible to break symmetries and tune the dimensionality of the magnetic or conductive properties of the sample.

In relation to frustrated magnets, uniaxial pressure could prove an extremely powerful tuning parameter. As frustration is a result of competing interactions, being able to tune these interactions independently of each other might lead to new, interesting phases of matter.

Scattering from magnetically frustrated materials is characterized by being broad and diffuse. As a consequence of this a uniaxial pressure cell designed for studying these materials will have to obey a strict set of criteria:

- The pressure cell needs to have a low and homogeneous background.
- It has to be constructed from materials with no magnetic correlations to enable polarization analysis.
- It needs to be possible to scan a broad  $Q$ -range to map the broad features characteristic of magnetically frustrated systems.

The purpose of this project has been twofold. First, I will present the design, and calibration process of a uniaxial pressure cell optimized for use in neutron scattering experiments on frustrated magnetic systems. Second, I will present neutron measurements of spin ice material  $\text{Ho}_2\text{Ti}_2\text{O}_7$  under uniaxial pressure. In addition, I will discuss possible improvements and future applications of the uniaxial pressure cell. I will, however, begin with a brief introduction to the theory of magnetism in condensed matter systems and to the technique of neutron scattering.



# Chapter 2

## Magnetism

This chapter provides a brief introduction to the study of magnetism in solid matter. For a much more thorough introduction to the field, see [13, 14].

Macroscopic magnetism is an emergent feature deriving from quantum mechanical interactions on the atomic scale. It arises as a consequence of electrons in solids carrying orbital angular momentum,  $\mathbf{L}$ , and inherent angular momentum, spin,  $\mathbf{S}$ . In many elements this does not result in a net angular momentum. Electrons are filled into shells by minimizing the total energy of the atom, this process can be approximated by a set of empirically determined rules, Hunds rules [13]. In some cases, these energy minimization rules will lead to an only partially filled outer electron shell, giving the ion a net total angular momentum  $\mathbf{J} = \mathbf{S} + \mathbf{L}$ . For some ions a strong crystal field interaction, causes the angular momentum to be quenched leading to the state with lowest energy to be one with  $\mathbf{L} = 0$ . Thus the total angular momentum is  $\mathbf{J} = \mathbf{S}$  and the resulting magnetic moment is given as

$$\boldsymbol{\mu} = g\mu_B\mathbf{S}, \quad (2.1)$$

where  $\mu_B$  is the Bohr magneton. As magnetism arise from ensembles of ions, we need to consider how spins interact with each other. From electromagnetism we know that magnetic dipoles in a vacuum interact via the magnetic dipole interaction. For two isolated dipoles separated with distance  $\mathbf{r}$  and with magnetic moments  $\boldsymbol{\mu}_1, \boldsymbol{\mu}_2$  and, such as two spins, the energy of this interaction is

$$E = \frac{\mu_0}{4\pi r^3} \left[ \boldsymbol{\mu}_1 \cdot \boldsymbol{\mu}_2 - \frac{3}{r^2} (\boldsymbol{\mu}_1 \cdot \mathbf{r})(\boldsymbol{\mu}_2 \cdot \mathbf{r}) \right]. \quad (2.2)$$

Given a typical inter atomic distance in a physical lattice,  $r = 1 \text{ \AA}$  and magnetic moments  $\mu = \mu_B$  this interaction energy can be estimated to  $\frac{\mu^2}{4\pi r^3} \approx 1 \text{ K}$ . While this can be a significant contribution in systems with very large magnetic moments, it is never large

enough to explain the existence of room temperature magnetism. To explain this, we need to consider the *exchange interaction*.

Consider two electrons ( $S = \frac{1}{2}$ ) with spatial wavefunctions ( $\psi_a, \psi_b$ ). When brought close to each other the spins can either form a triplet ( $S = 1$ ) or a singlet ( $S = 0$ ). To obey fermionic exchange statistics the total wavefunction must be anti-symmetric. The triplet state is symmetric and the singlet is anti-symmetric and this constrains the spatial part of the wavefunctions and yields two possible total wavefunctions, given by

$$|\Psi_S\rangle = \frac{1}{\sqrt{2}} [\psi_a(\mathbf{r}_2)\psi_b(\mathbf{r}_1) + \psi_a(\mathbf{r}_1)\psi_b(\mathbf{r}_2)] \chi_S, \quad (2.3a)$$

$$|\Psi_T\rangle = \frac{1}{\sqrt{2}} [\psi_a(\mathbf{r}_2)\psi_b(\mathbf{r}_1) - \psi_a(\mathbf{r}_1)\psi_b(\mathbf{r}_2)] \chi_T. \quad (2.3b)$$

Estimating the energy difference between these states results in

$$J = \frac{1}{2} \left( \langle \Psi_S | \mathcal{H} | \Psi_S \rangle - \langle \Psi_T | \mathcal{H} | \Psi_T \rangle \right) = \int \psi_a^*(\mathbf{r}_1)\psi_b^*(\mathbf{r}_2) \mathcal{H} \psi_a(\mathbf{r}_2)\psi_b(\mathbf{r}_1) d\mathbf{r}_2 d\mathbf{r}_1. \quad (2.4)$$

Where  $\mathcal{H}$  is the Hamiltonian associated with the Coulomb repulsion between the electrons. This result indicates that the spin interactions are entirely governed by the electrostatic interactions between the electrons and the system will essentially pick any spin state that minimizes the Coulomb energy. The value of  $J$  can vary from a few mK to hundreds of K and as it turns out is the main mechanism behind most magnetic phenomena.

Generalising to an ensemble of  $N$  magnetic particles it is possible to show that the interaction energy of such an ensemble is given as the Heisenberg Hamiltonian,

$$\mathcal{H}_H = - \sum_{\langle i,j \rangle}^N J_{i,j} \mathbf{S}_i \cdot \mathbf{S}_j. \quad (2.5)$$

In this case the interaction is truncated to nearest neighbour interaction, this is denoted by the angled brackets. Determining  $J_{i,j}$  analytically can be very difficult. The value of  $J_{i,j}$  is affected by the geometry of the lattice, the bond length and by neighbouring non-magnetic ions. It is however possible to determine experimentally in a number of ways e.g by measuring the spin wave dispersion (2.8).

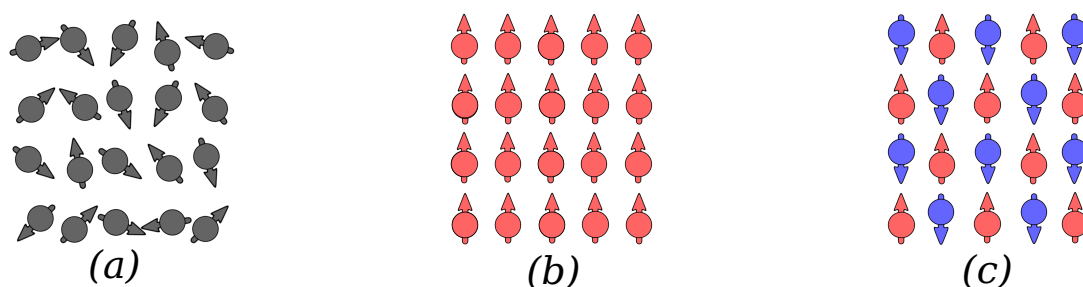
## 2.1 Magnetic Order

Let us consider what would happen in one of the simplest geometries, the cubic lattice. Intuitively, the square lattice is simpler but according to the Mermin-Wagner theorem no long range order can occur in one or two dimensional lattices at finite temperature [15]. At temperatures that are high compared to the exchange interaction  $J$ , thermal fluctuations will dominate the system and spins will be pointing in random directions. This is known as the paramagnetic phase, (figure 2.1a). "Para" meaning with or along, alluding to the fact that in this phase the magnetic properties are limited to the ability to be magnetized by an external magnetic field ( $\mathbf{B}$ ) described by the *Zeeman* Hamiltonian

$$\mathcal{H}_Z = g\mu_B \sum_i \mathbf{S}_i \cdot \mathbf{B}. \quad (2.6)$$

When the system is then cooled below some ordering temperature defined by the exchange interaction, it will order. For  $J > 0$  the state with the lowest energy is one where the spins are aligned with their nearest neighbours as seen in figure 2.1b, this is known as the *ferromagnetic* ground state. In the same manner, for  $J < 0$  the energy is minimized when all of the spins are anti-aligned with their nearest neighbours, yielding the *antiferromagnetic* ground state, shown in figure 2.1c.

A puzzling feature of this ordering is the fact that the spins seem to *choose* a preferred direction, although there is apparently no underlying preference for any specific direction.



**Figure 2.1:** Above the ordering temperature the system is in the *paramagnetic* phase, the system is completely isotropic as the spins are oriented randomly. When cooled below the ordering temperature, the system will order into the *Ferromagnetic* state (b) if  $J > 0$  or *Antiferromagnetic* state (c) for  $J < 0$ .

For a mathematically perfect lattice, there is in fact no preferred direction and the ground state is actually just a metastable state as the state with (Though random transition between the different ground states is virtually impossible). In real systems however, an anisotropic crystal field or even impurities will result in a preferred direction.

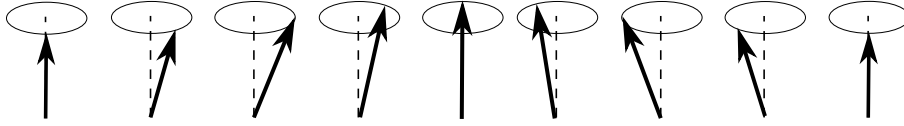
The ordering temperature can be estimated by fitting the high temperature susceptibility

with the *Curie-Weiss law* [13]

$$\chi \propto \frac{1}{T - |\Theta_{CW}|}. \quad (2.7)$$

This estimate is known as the Curie-Weiss temperature,  $|\Theta_{CW}|$ . The Curie-Weiss law derives from a mean-field approximation of the magnetisation. It can therefore be quite inaccurate when there are competing interactions or geometries that are not described in the mean field model. Therefore, the ordering temperature is better measured experimentally by looking for divergences in the magnetic susceptibilities or by measuring the magnetic Bragg scattering, present only in the case of long range order (Section 3.4). For a ferromagnet the ordering temperature is called the *Curie* temperature ( $T_C$ ), whereas the antiferromagnetic ordering temperature is known as the *Néel* temperature ( $T_N$ ).

### 2.1.1 Spin Waves



**Figure 2.2:** Spin wave in an isotropic ferromagnet, the perturbation causes the spins to precess around the equilibrium axis.

In the temperature range between ordering at  $T_C/T_N$  and  $T = 0$  K, there is still plenty of thermal energy present to create excitations, the most well known of which are the spin waves, or magnons.

For an isotropic ferromagnetic spin chain with a large magnetic moment  $S > \frac{1}{2}$  at  $T = 0$  K. The system will be in the ferromagnetic ground state, all spins pointing in the same direction (figure 2.1b). One spin is then perturbed slightly away from the equilibrium position. This perturbation could be caused by exchanging energy with the lattice vibrations or by scattering with a neutron. The spin will start precessing around the equilibrium axis, this precession then propagates through the spin chain in the manner shown in figure 2.2. Formalizing this through the time evolution of the spin operator it is possible to calculate the ferro- and antiferromagnetic spin wave distributions [13]

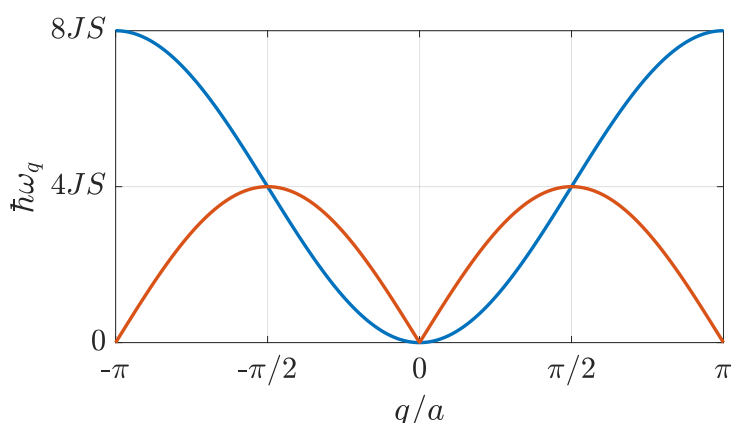
$$\text{Ferromagnet : } \hbar\omega_q = 4JS(1 - \cos qa), \quad (2.8)$$

$$\text{Antiferromagnet : } \hbar\omega_q = 4JS|\sin qa|. \quad (2.9)$$

Both of them are plotted in figure 2.3.

Spin waves are exclusively a product of long range order. Thus, they can not exist above

the ordering temperature or in systems with only short range order.



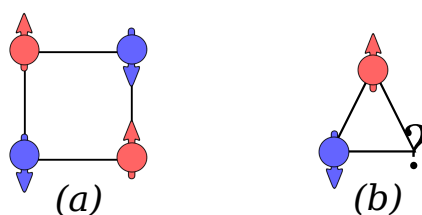
**Figure 2.3:** Ferromagnetic spin wave dispersion (blue) and antiferromagnetic spin wave dispersion (orange). As they both go to zero continuously, there exists spin wave modes that cost no energy to excite with  $q = 0, \pi$ .

## 2.2 Frustrated Magnetism

Frustrated materials refers to a subset of magnetic materials where the ordering temperature is suppressed due to a large ground state degeneracy [16]. This most commonly occurs due to geometrical constraints. Consider the *Ising* interaction

$$\mathcal{H} = -J \sum_{\langle i,j \rangle} S_i^z S_j^z. \quad (2.10)$$

This is a simplified version of the Heisenberg Hamiltonian where only the z-components of the spins interact. This is used to describe a system with a strong easy axis anisotropy, which may occur as a consequence of an asymmetric crystal field [13]. If  $J < 0$ , the ground state of this Hamiltonian should be one where all the spins are anti-aligned with their nearest neighbours and along the z-axis. This is indeed the case for the square lattice (figure 2.4a.), but turns out to be impossible for the triangular lattice (figure 2.4b.).



**Figure 2.4:** The antiferromagnetic Ising state on the square lattice results in a stable ground state (a). The same nearest neighbour exchange interaction on the triangular lattice results in a degenerate ground state manifold (b).

Anti-aligning two spin leaves the third spin "undecided". As flipping the third spin doesn't change the total energy, the resulting ground state is degenerate [13].

By generalizing this principle to larger lattices it quickly becomes clear that a physical lattice will host a massively degenerate ground state manifold. This will result in a system that has no ordered phase but instead fluctuates between the many spin configurations of the ground state manifold.

In general, frustrated systems are dominated by short range correlations, this is known as *cooperative paramagnetism*. In many real systems other interactions will break the degeneracy at low temperatures resulting in a suppressed ordering temperature and cooperative paramagnetism between  $|\Theta_{CW}|$  and the ordering temperature  $T_N$ . The actual ground state of the 2D triangular lattice has been a subject of much research.

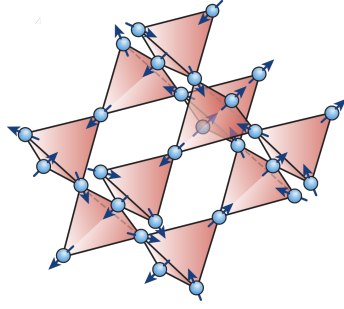
In 1973 Anderson proposed that it is the so called RVB state [4, 17]. He showed that the energy of a state where the spins couple two and two in singlet states have a lower energy than the Néel state. This discovery and its believed connection to high temperature superconductivity [5] became the basis of the entire field of quantum spin liquids [6, 10]. A phase of matter that can only exist at  $T = 0$  K as it is dominated by long range quantum entanglement.

As frustrated systems show no long range order, excitations can not manifest in the form of spin waves. Excitations will instead manifest themselves in other ways. The form they take varies a lot, but in general they will be short range in nature. Fundamentally, frustrated systems are difficult to describe, this is because the global symmetries that allow us to describe ordered magnetic systems are not upheld. This in turn is also one of the things that makes magnetic frustration interesting.

The example presented in figure 2.4 is a 2D lattice, there are however multiple real world examples of 3D frustrated lattices, such as the hyperkagomé [18] or pyrochlore lattice. The latter of which has been the focus of this project.

## 2.3 Spin Ice Materials

In this thesis I will deal with a subclass of magnetically frustrated materials, the so called *Spin Ice* materials [19]. They have the chemical composition  $A_2^{3+}B_2^{4+}O_7$ , where A is a magnetic rare earth ion, such as Holmium, Dysprosium or Ytterbium and B is a non-magnetic transition metal ion. Spin ice have the pyrochlore lattice structure shown in figure 2.5, the magnetic ions are on corner sharing tetrahedra. Classical spin ice, characterized



**Figure 2.5:** Spin ice is characterized by the magnetic ions being on corner sharing tetrahedra. The strong local  $\langle 111 \rangle$  Ising anisotropy gives rise to the two-in-two-out spin structure, depicted. Figure from [10].

by its very large magnetic moment<sup>1</sup>, is modelled by using the dipolar spin ice model (DSM), the associated Hamiltonian is [20]

$$\mathcal{H}_{DSM} = J_{nn} \sum_{\langle i,j \rangle} \mathbf{S}_i^{z_i} \cdot \mathbf{S}_j^{z_j} + Dr_{nn}^3 \sum_{i>j} \frac{\mathbf{S}_i^{z_i} \cdot \mathbf{S}_j^{z_j}}{|r_{ij}|^3} - \frac{3(\mathbf{S}_i^{z_i} \cdot \mathbf{r}_{ij})(\mathbf{S}_j^{z_j} \cdot \mathbf{r}_{ij})}{|r_{ij}|^5}. \quad (2.11)$$

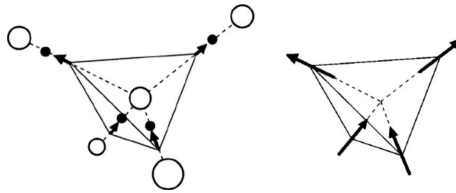
The first term in (2.11) corresponds to the nearest neighbour exchange interaction (nn). As we are only dealing with classical spins we would expect a nearest neighbour term identical to the one in (2.5). However, there is a strong local  $\langle 111 \rangle$ -Ising anisotropy which essentially forces the spins to point along the local  $\langle 111 \rangle$ -axis, running between the centres of neighbouring tetrahedra. This means that even though the magnetic moment in these materials is large, the spin behaves like an Ising spin.

The second term in (2.11) corresponds to the dipolar term, this is relevant due to the very large magnetic moment of the magnetic ions,  $D$  denotes the magnitude of this interaction. Given the long range nature of the dipolar term, one would think that it would lead to long range order at low temperature. However, it turns out that the dipolar interaction almost perfectly self-screens [21], cancelling and resulting in the same ground state as would be found with only the nn interaction. Namely, the spins pointing along the  $\langle 111 \rangle$ , easy-axis, two towards and two away from the centre of each tetrahedron as depicted in figure 2.5.

This configuration is what gives spin ice its name. The "two-in-two-out" structure, referred to as the *ice rule*, resembles the placement of the hydrogen ions relative to the oxygen ions in water ice. Figure 2.6 shows a comparison between the two.

---

<sup>1</sup>lower moments is a subject in and of it self, an introduction can be found in [9].



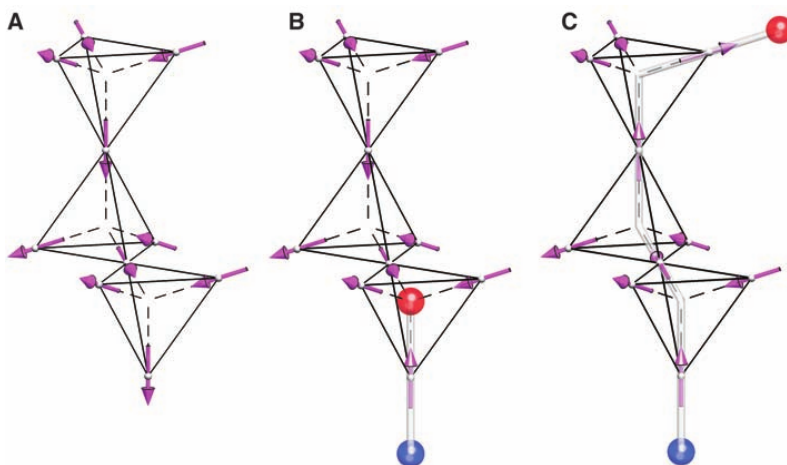
**Figure 2.6:** Comparison between water ice (left) and spin ice (right). In water ice, the hydrogen ions (closed circles) are organized in a tetrahedral structure, with two of them being close to the oxygen ion (open circles) in the centre of the tetrahedron and two of them further away. Figure from [19].

This resemblance with water ice goes even further. According to thermodynamics, the entropy of any system should go to zero as it settles in to its ground state. In 1935 Linus Pauling showed that due to the degeneracy of the state shown in figure 2.6, water ice will have a residual zero point entropy of

$$S_0 = \frac{1}{2} R \ln \left( \frac{3}{2} \right), \quad (2.12)$$

per hydrogen ion at  $T = 0$  K. The same thing should be true for the spin entropy of a spin ice system, if the mapping described above is accurate. In 1999 this was indeed found to be the case, when the residual entropy of the spin ice  $\text{Dy}_2\text{Ti}_2\text{O}_7$  was measured experimentally by Ramirez et al. [22].

### 2.3.1 Magnetic Monopoles

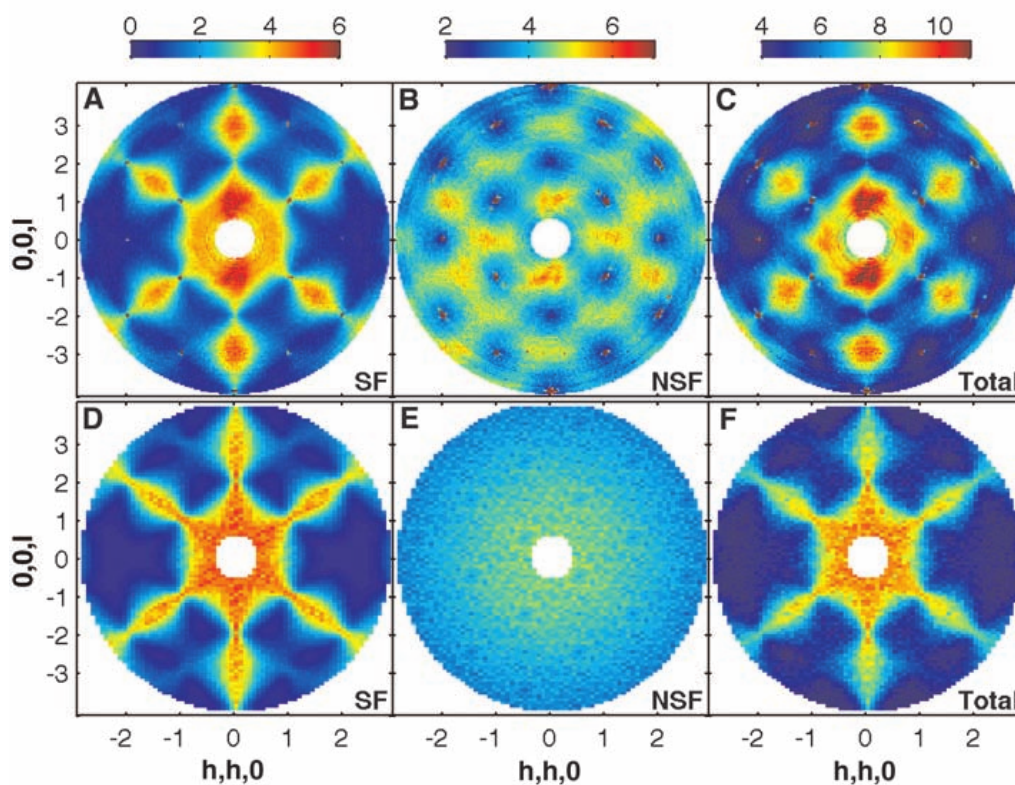


**Figure 2.7:** Excitations in spin ice. Flipping one spin introduces a local defect of opposite magnetic charge in the tetrahedra connected by the spin. Flipping another spin in either of the tetrahedra restores the ice rule in the original tetrahedron, moving the defects away from each other. These excitations can be described as magnetic monopoles. Figure from [8].



### 2.3. Spin Ice Materials

Due to the lack of long range order, there are no spin waves in spin ice systems, there are however long range interactions. Suppose the system is in one of the magnetic ground states, all tetrahedra have two spins pointing toward the centre and two pointing away (figure 2.7A). The lowest possible excitation would then, naturally, be flipping one spin (figure 2.7B). This introduces a differing magnetic "charge" in the two neighbouring tetrahedra. It is then apparent that flipping another spin in one of these tetrahedra does not change the total energy of the system as long as it restores the ice rule in that first tetrahedron. This effectively moves the magnetic "charges" away from each other (figure 2.7C) [7].



**Figure 2.8:** Diffraction scattering pattern of  $\text{Ho}_2\text{Ti}_2\text{O}_7$ , experiment (A-C) and theory (D-F). The total scattering (C, F) is the sum of the spin flip (SF) and non spin flip signal (NSF). Figure from [8].

As they interact very weakly they can be modelled as magnetic monopoles, free to move throughout the lattice with no additional energy cost. The series of flipped spins connecting the two monopoles of opposite charge is known as a Dirac string.

In 2009 polarized neutron scattering was used to measure the scattering from the spin ice  $\text{Ho}_2\text{Ti}_2\text{O}_7$ . This was done by Fennell et al. [8] and at the same time by Morris et al. [23]. Figure 2.8 shows the spin flip scattering pattern measured by Fennell et al. compared to simulations. The details of neutron scattering is explained in chapter 3. The spin flip

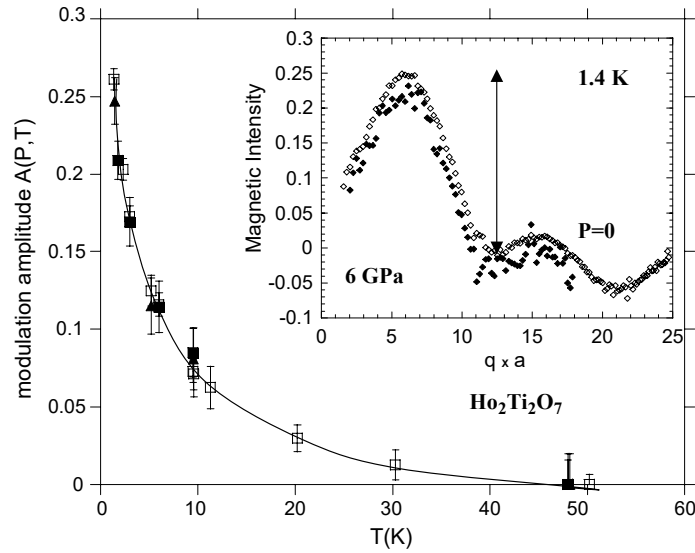
scattering denotes the part of the scattering that flipped the spin of the neutron. Whereas the opposite is true for the non-spin flip case. The total is the sum of the two.

The broad features in the scattering pattern corresponds to short range correlations, this is consistent with the degenerate nature of the ground state. Broad features are in general characteristic for the scattering pattern of magnetically frustrated systems. A much more unique feature are the *pinch-points*, referring to the regions where the broad features narrow and become almost point like. These are considered evidence for the Dirac strings connecting the magnetic monopoles discussed above.

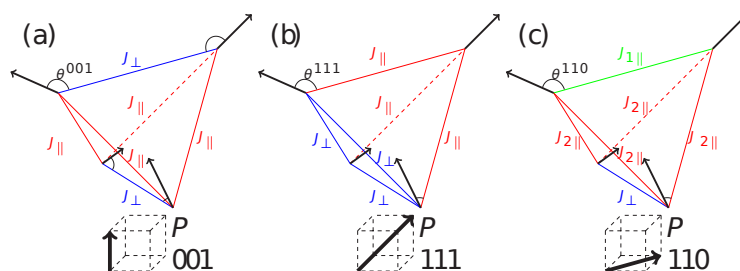
There are a few discrepancies between theory and data. Most significantly, the experiment shows quite a large magnetic contribution in the NSF data, which is not present in the theoretical scattering pattern.

### 2.3.2 Spin Ice Under Uniaxial Pressure

For some time, it has been theorized that perturbing a spin ice system using pressure, would induce a new phase of matter. Neutron experiments performed by Mirebeau et al. [24] on  $\text{Ho}_2\text{Ti}_2\text{O}_7$  under hydrostatic pressure of up to 6 GPa, however, show no deviation from the scattering pattern at ambient pressure. As shown in figure 2.9, the modulation amplitude does not vary with hydrostatic pressure. The modulation amplitude is defined as  $I_{max} - I_{min}$  in the  $Q$ -window shown in the inset of the figure.

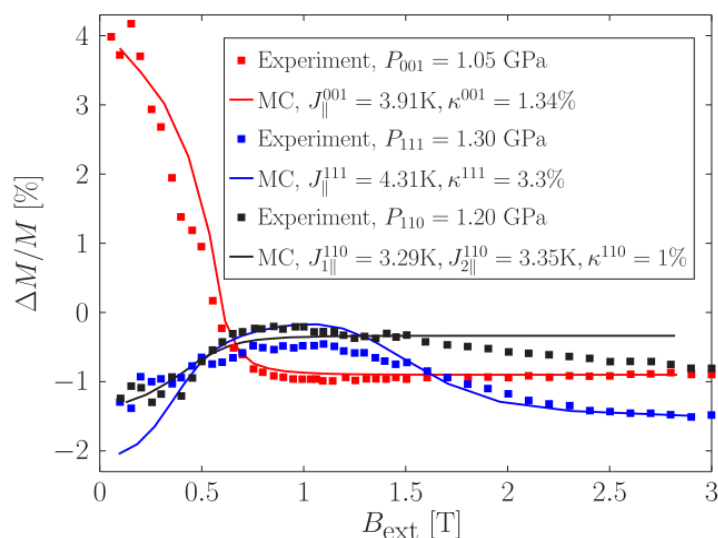


**Figure 2.9:** Modulation amplitude plotted as a function of temperature for ambient pressure as well as 5 GPa and 6 GPa. The inset depicts the ambient pressure and 6 GPa data at 1.4 K. The modulation amplitude is defined as  $I_{max} - I_{min}$  (length of the arrow). Figure from [24].



**Figure 2.10:** The three different directions that pressure is applied in the model. The number of parameters needed to model the system differs depending on the direction of the pressure. Note that the value of  $J_{\parallel}$  is not necessarily the same for the different cases. Figure from [25]

In 2007 Mito et al. showed that the spin ice material  $\text{Dy}_2\text{Ti}_2\text{O}_7$  display a significant magnetisation response under uniaxial pressure [26]. This data is shown in figure 2.11. Subsequent theoretical models using only nearest neighbour interactions suggest a uniaxial pressure induced phase transition to a ferromagnetic state [27]. Richard Edberg at KTH, Stockholm has expanded the model to include dipolar interactions and it is this theoretical work that forms the basis for this project [25].



**Figure 2.11:** Magnetisation data measure by Mito et al. [26] plotted along with MC fits generated using the DSM model.  $\kappa$  denotes the compression of the lattice in the direction of the pressure. Figure from [25]

The pressure is modelled along three orthogonal directions. When the crystal is compressed, the exchange interactions will change with pressure. It is assumed that the interactions perpendicular to the pressure will not change. The notation is introduced in figure 2.10. Due to the symmetries of the system, the all the interactions can be described with two different values,  $J_{\parallel}$  and  $J_{\perp}$  for pressure in the (001) and (111) directions where

as three  $J_{1\parallel}$ ,  $J_{2\parallel}$  and  $J_{\perp}$  are needed for the (110 plane).

As the previous work has been done on  $\text{Dy}_2\text{Ti}_2\text{O}_7$  (DTO) [26], this is chosen as the model system. DTO is however not very suitable for neutron experiments as Dysprosium has a very large neutron absorption cross section [28]. For this reason, simulations are also performed for the very similar  $\text{Ho}_2\text{Ti}_2\text{O}_7$  (HTO), as the goal is to do neutron measurements on this material.

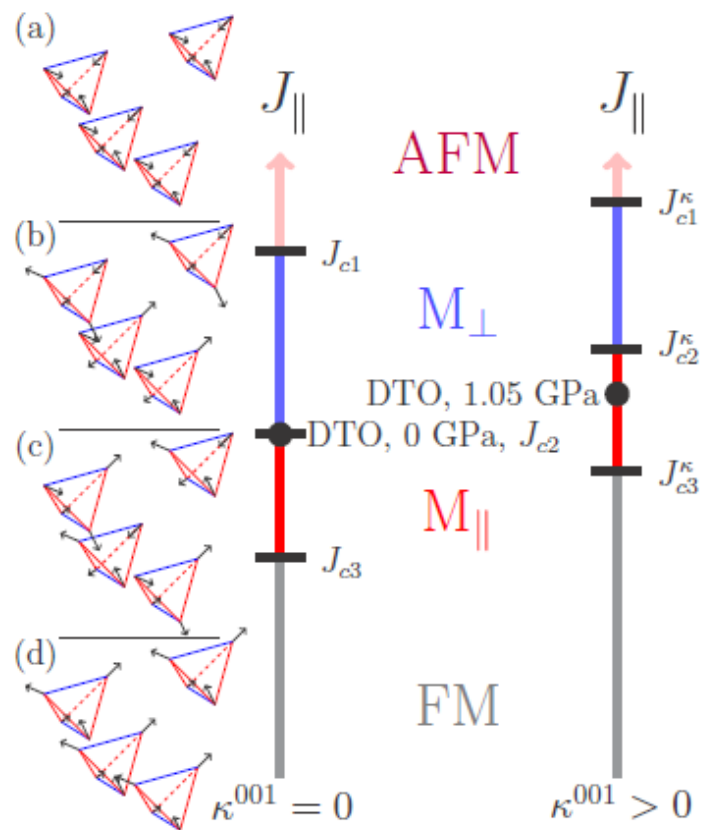
The parameters of the model (2.11) are then optimized, so that they offer the best fit to the magnetization data measured by Mito et al. The resulting fits are shown in figure 2.11 along with data.

As the response is clearly most significant for pressure in the (001) direction, this case is examined more thoroughly. The associated ground state turns out not to be a ferromagnetic state as has been previously proposed. The added dipolar term seems to maintain some of the degeneracy in the system. Figure 2.12 shows the four different possible states in the phase diagram of DTO. At ambient pressure, DTO is on the phase boundary between the  $M_{\perp}$ , which has spin chains perpendicular to the (001) and  $M_{\parallel}$  which has spin chains parallel to (001). This means that all of the states that obey the ice rule are degenerate. When pressure is applied, the exchange interactions are distorted, causing all the phase boundaries to move. At the same time, DTO also shifts in the phase diagram, pushing it into the  $M_{\parallel}$  state. This is what leads to increased magnetization in the direction of the pressure in figure 2.11. The ground state manifold has been reduced to only include the ones with spin chains in the direction of the pressure. The previously proposed ferromagnetic state is not accessible unless the pressure is much higher. By linear extrapolation of  $J_{\parallel}$ , the pressure has to be as high as 3.4 GPa.

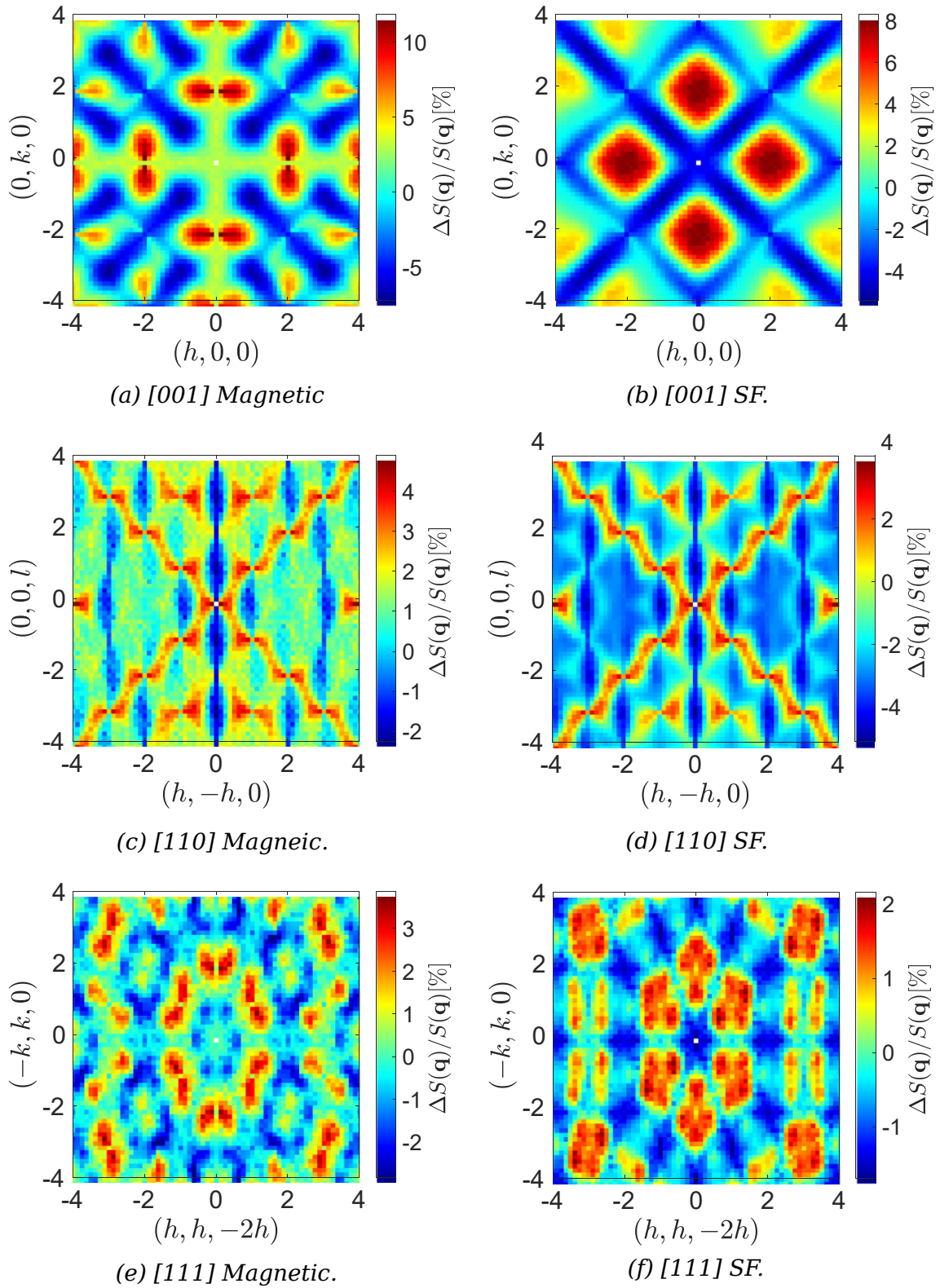
It is then possible to compute the relative change in the scattering cross section

$$\frac{\Delta S(\mathbf{Q})}{S(\mathbf{Q})} = \frac{S(\mathbf{Q})_{P>0} - S(\mathbf{Q})_{P=0}}{S(\mathbf{Q})_{P=0}} \quad (2.13)$$

for the parameters found by fitting to the magnetization data. These can be seen in figure 2.13. It is this theoretical work that founds the basis of the experimental studies in this thesis. The same model described here were used to calculate the neutron cross section  $\text{Ho}_2\text{Ti}_2\text{O}_7$  under uniaxial pressure, that will be discussed in subsequent chapters.



**Figure 2.12:** The four possible ground states plotted with the corresponding phase boundaries  $J_{ci}$  for ambient pressure and  $J_{ci}^{\kappa}$  for  $P > 0$ . Applied pressure distorts the phase boundaries and also shifts DTO in the phase diagram. Figure from [25]



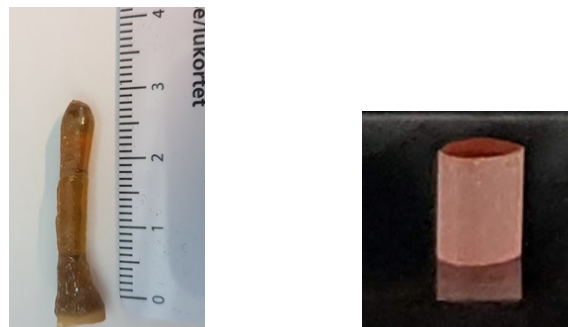
**Figure 2.13:** Relative change in both magnetic and spin flip elastic cross sections for DTO under uniaxial pressure in the direction perpendicular to the scattering plane.

### 2.3.3 $\text{Ho}_2\text{Ti}_2\text{O}_7$ Sample

In this project, neutron experiments were performed on Holmium Titanate.  $\text{Ho}_2\text{Ti}_2\text{O}_7$  (HTO) is a spin ice material as discussed above, with nearest neighbour exchange  $J_{nn} = 1.56$  K [29]. As  $\text{Ho}^{3+}$  has total angular momentum,  $J = 8$ , it consequently has a very large magnetic moment,  $\mu \sim 10\mu_B$ . For this reason it has a significant dipolar interaction, given by the parameter  $D = 1.41$  K [29]. HTO has a cubic unit cell with lattice parameter  $10.1\text{\AA}$  [30].

HTO has a ferromagnetic Curie-Weiss temperature of  $\Theta_{CW} \sim 2$  K, but due to frustration it does not order down to mK temperatures. Around  $\Theta_{CW}$  it instead transitions into the spin ice state, dominated by short range correlations.

In this project, the goal is to measure HTO under uniaxial pressure and thus the sample has to be aligned very accurately and cut very precisely to ensure a completely flat contact surface between the pressure cell and the sample. For this reason, the alignment and cutting is outsourced to a company that specialise in this. In figure 2.14, an image of the entire sample, as it is grown, is shown next to an image after it is cut.



**Figure 2.14:** HTO sample after it is grown (left). The sample is then cut into cylinders with dimensions  $h = 3$  mm and  $d = 3$  mm or  $d = 2$  mm (right). The samples are synthesised and grown by Ingrid Marie Bakke Fjellvåg.

# Chapter 3

## Neutron Scattering

Neutron scattering has proved a versatile method for determining structure and dynamics in solid state systems. This section provides an overview of the techniques relevant to this project. The field of neutron scattering is much larger and more varied than what is presented here, sources for additional information include [31, 32].

### 3.1 The Neutron

As neutrons are uncharged, they only interact with the sample via the short ranged nuclear interactions. This means that as opposed to primarily scattering from the surface of the sample, neutrons provide bulk measurements. This property also means that it is possible to have a significant sample environment around the sample, as neutrons interact quite weakly with matter.

Furthermore, the energy scale of neutrons match that of fundamental excitations very well making them a perfect probe for studying the vibrational modes of materials.

Lastly as neutrons have spin, they are ideally suited to probe both the magnetic structure and magnetic excitations. It is even possible, in the case of weakly correlated magnetic materials, to separate the magnetic and structural scattering signals completely.

The neutron is an integral part of almost all matter, as it can be found in the nucleus of all known elements except for the most common hydrogen isotope  $^1\text{H}$ . When in the nucleus, the neutron is stable but in its free state it has a lifetime of around 15 minutes. The neutron has a mass of  $m_n = 1.675 \cdot 10^{-27}$  kg, very close to that of the proton. It carries no charge but due to its spin, it has a magnetic moment,

$$\hat{\boldsymbol{\mu}} = \gamma \mu_N \hat{\boldsymbol{\sigma}}. \quad (3.1)$$

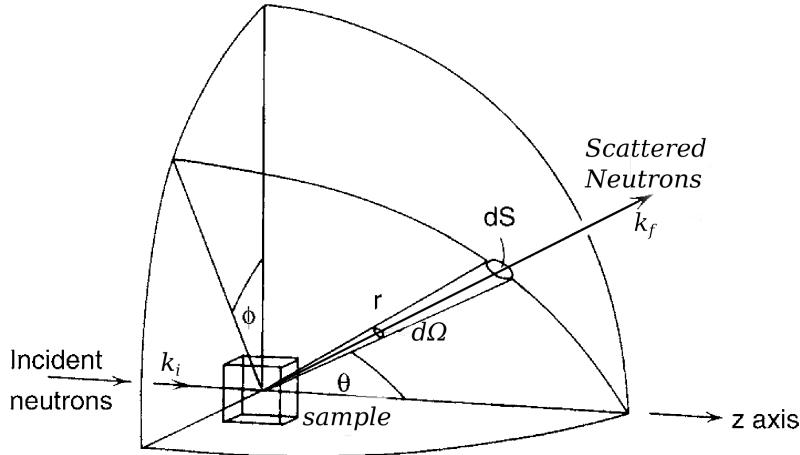


Where  $\mu_N$  is the nuclear magneton,  $\gamma$  is the gyromagnetic ratio and  $\hat{\sigma}$  is the *Pauli spin operator*. According to quantum mechanics, neutrons have both particle and wave properties. As a consequence of this, a neutron moving with velocity  $v$  can be described by its associated *De Broglie* wavelength [32]

$$\lambda = \frac{2\pi\hbar}{m_n v}. \quad (3.2)$$

As neutrons are bound in the nuclei of atoms, it is not entirely straight forward to obtain free neutrons, to perform scattering experiments. Therefore neutron experiments are limited to large scale facilities. They fall in to two categories, the older reactor sources (FRM-2, NIST, HFIR, ILL) that produce neutrons in fission reactors and the newer spallation sources (SNS, ISIS, PSI, ESS), that produce neutrons by accelerating protons into a neutron-rich target [32].

## 3.2 Scattering Theory



**Figure 3.1:** Schematic of a scattering event. The incoming neutron beam hits the sample and is scattered with scattering angle  $2\theta$  and azimuthal angle  $\phi$  into solid angle  $d\Omega$ . Figure adapted from [33].

A scattering event as the one depicted in figure 3.1 consists of a sample and an incoming beam of neutrons, that scatters off the sample. The incoming beam can be described as a plane wave by a wave vector  $\mathbf{k}_i$  [31]

$$\psi_i(\mathbf{r}) = \frac{1}{\sqrt{Y}} \exp(i\mathbf{k}_i \cdot \mathbf{r}). \quad (3.3)$$

Where  $Y$  is a normalisation constant. The neutron beam is scattered by the sample with scattering angle  $2\theta$ , the scattered neutrons are likewise described by a plane wave, with wave vector  $\mathbf{k}_f$ . To quantify the number of neutrons scattered into a given solid angle  $d\Omega$  the differential scattering cross section is defined

$$\frac{d\sigma}{d\Omega} = \frac{\# \text{ of neutrons scattered in to } d\Omega}{d\Omega I_0}, \quad (3.4)$$

where  $I_0$  is the total flux of the incoming neutron beam. By considering the possibility that the scattering event changes the energy of the neutron from  $E_i$  to  $E_f$ , (3.4) can in turn be generalised into the partial differential scattering cross section

$$\frac{d\sigma^2}{d\Omega dE_f} = \frac{\# \text{ of neutrons scattered in to } d\Omega, \text{ with energies } [E_f, E_f + dE_f]}{d\Omega dE_f I_0}. \quad (3.5)$$

To calculate (3.5), it is necessary to determine the transition probability between a plane-wave state with wave vector  $\mathbf{k}_i$  and one with wave vector  $\mathbf{k}_f$ . This probability is given by Fermi's Golden rule

$$W_{i \rightarrow f} = \frac{2\pi}{\hbar} \left| \langle \psi_f | \hat{V} | \psi_i \rangle \right|^2 \rho(E_f). \quad (3.6)$$

$\hat{V}$  is the interaction potential given by the sample, and  $\rho(E_f)$  is the density of states per unit energy of the scattered neutrons. Calculating this and normalising by incident flux yields the partial differential scattering cross section

$$\frac{d\sigma^2}{d\Omega dE_f} = \left( \frac{Y m_n}{2\pi \hbar^2} \right)^2 \frac{k_f}{k_i} \left| \langle \psi_f, \lambda_f | \hat{V} | \psi_i, \lambda_i \rangle \right|^2 \delta(E_{\lambda_i} - E_{\lambda_f} + \hbar\omega). \quad (3.7)$$

The initial and final state of the sample is denoted as  $\lambda_{i,f}$  and  $\hbar\omega = E_i - E_f$  is the energy transferred to the sample by the neutron. Thus the delta function ensures energy conservation. In the following we will examine the elastic contribution to the scattering cross section, denoted  $\left( \frac{d\sigma}{d\Omega} \right)_{\text{el}}$ , thus we will assume  $\hbar\omega = 0$  and  $k_i = k_f$ .

### 3.3 Nuclear Scattering

I will begin by considering scattering from the nuclei of a static lattice. This interaction can be approximated with the *Fermi pseudo-potential*

$$\hat{V}(\mathbf{r}) = \sum_j \frac{2\pi\hbar}{m_n} b_j \delta(\mathbf{r} - \mathbf{r}_j). \quad (3.8)$$

### 3.3. Nuclear Scattering

---

Here, the  $j$ 'th nucleus in the lattice is approximated as a delta function in space at position  $\mathbf{r}_j$ . The scattering length,  $b_j$  is an inherent property of the isotope. It has units of length and sets the magnitude of the interaction between the neutron and the nucleus. Inserting 3.8 into 3.7, yields

$$\left(\frac{d\sigma}{d\Omega}\right)_{\text{nuc, el.}} = \frac{Y^2 m_n^2}{4\pi^2 \hbar^4} \left| \langle \psi_f, \lambda_f | \frac{2\pi\hbar}{m_n} \sum_j^N b_j \delta(\mathbf{r} - \mathbf{r}_j) | \psi_i, \lambda_i \rangle \right|^2 = \left| \sum_j^N b_j \exp(i\mathbf{Q} \cdot \mathbf{r}_j) \right|^2 \quad (3.9)$$

Here, the scattering vector  $\mathbf{Q}$  has been defined as  $\mathbf{Q} \equiv \mathbf{k}_i - \mathbf{k}_f$ . This quantity turns out to be extremely useful and has a physical interpretation,  $\hbar\mathbf{Q}$  is the momentum exchanged with the sample in the scattering event. For an elastic scattering event, there is no energy transfer and thus  $k_i = k_f = k$ . Using this, we arrive at

$$Q = \frac{4\pi \sin(\theta)}{\lambda}, \quad (3.10)$$

where  $\lambda$  is the wavelength of the neutron. (3.9) holds true only in the case were the nuclei are fixed in space. Real atoms however, vibrate and this vibration adds a certain dampening to the elastic scattering signal, known as the Debye-Waller factor

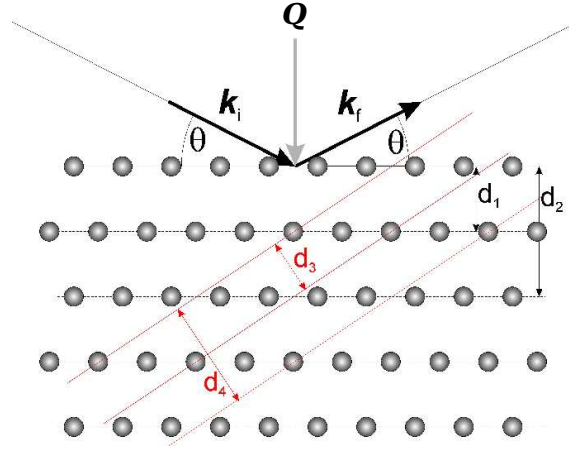
$$\exp(-2W_j) = \exp(-2 \langle \mathbf{Q} \cdot \mathbf{u}_j(t) \rangle^2). \quad (3.11)$$

Here  $\mathbf{u}_j(t)$  is the displacement from equilibrium of the  $j$ 'th atom as a function of time. The angled bracket denotes the time average. It is usually assumed that this term is identical for all atoms. Multiplying (3.11) with (3.9), we have in principle arrived at the nuclear scattering cross section.

So far we have considered the general case of an ensemble of nuclei. Let us consider the specific case of scattering with a crystalline material. This means that the material has translational symmetry, one such lattice is shown in figure 3.2.

By employing this periodicity of the lattice it is possible to change the sum over the atoms to two sums, one over the individual atoms in the unit cell ( $i$ ) and one over the unit cells  $j$ . By defining the relative position of the  $i$ 'th nucleus inside the unit cell as  $\Delta_i$ , we arrive at,

$$\left(\frac{d\sigma}{d\Omega}\right)_{\text{nuc, el.}} = \exp(-2W) \left| \sum_i b_i \exp(i\mathbf{Q} \cdot \Delta_i) \sum_j \exp(i\mathbf{Q} \cdot \mathbf{r}_j) \right|^2. \quad (3.12)$$



**Figure 3.2:** Scattering from a crystalline material. Scattering will result in *Bragg peaks* corresponding to different lattice spacings in the material ( $d_1$  and  $d_3$ ). Some spacings produce destructive interference ( $d_2$  and  $d_4$ ), resulting in  $|F_N(\mathbf{Q})|^2 = 0$ . Figure from [34].

By performing the sum over the unit cells ( $j$ ) we obtain

$$\left(\frac{d\sigma}{d\Omega}\right)_{\text{nuc, el}} = N \frac{(2\pi)^3}{V_0} \exp(-2W) |F_N(\mathbf{Q})|^2 \sum_{\mathbf{G}} \delta(\mathbf{Q} - \mathbf{G}). \quad (3.13)$$

Here  $V_0$  is the volume of the unit cell and  $F_N(\mathbf{Q})$  is the *nuclear structure factor*,

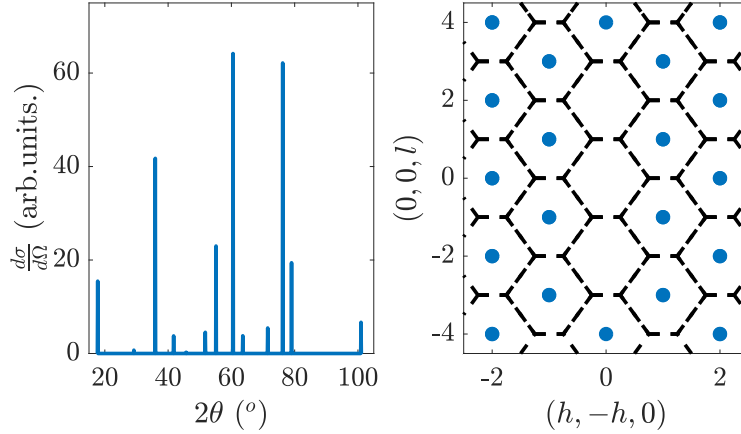
$$F_N(\mathbf{Q}) = \sum_i b_i \exp(i\mathbf{Q} \cdot \Delta_i). \quad (3.14)$$

The delta function in (3.13) is what is known as the *Laue Condition*, it means that scattering only occurs when  $\mathbf{Q}$  is equal to a reciprocal lattice vector  $\mathbf{G}$ . This is more famously expressed in terms of the *Bragg law* [34]

$$n\lambda = 2d \sin(\theta), \quad (3.15)$$

where  $n$  is an integer and  $d$  is the spacing between lattice planes. This does not mean that there is scattering from every reciprocal lattice point. Depending on the geometry of the lattice, scattering from some lattice planes will result in destructive interference, manifesting as  $F_N(\mathbf{G}) = 0$ . Different lattice plane choices can be seen in figure 3.2.

In figure 3.3 the structural Bragg scattering from spin ice material  $\text{Ho}_2\text{Ti}_2\text{O}_7$  has been plotted as a function of  $2\theta$  (left) along with their position in  $\mathbf{Q}$ -space (right). It has been calculated by inserting the scattering lengths of Ho, Ti and O along with their respective positions in the unit cell in (3.13) and calculating the corresponding scattering angle from (3.10).



**Figure 3.3:** Bragg peaks of  $\text{Ho}_2\text{Ti}_2\text{O}_7$ , calculated using (3.13). The relative intensity of each peak plotted as a function of scattering angle  $2\theta$  (left). Position of Bragg peaks plotted in reciprocal space along with the reciprocal unit cell (right). The center of each unit cell corresponds to a Bragg point ( $\mathbf{Q} = \mathbf{G}$ ).

### 3.4 Magnetic Scattering

As preciously stated, the neutron has a magnetic moment. This means that the neutron interacts with the spin state of the sample, leading to a magnetic contribution to the scattering cross section. The magnetic field generated by an electron at position  $\mathbf{r}_j$  is given as [31]

$$\mathbf{H}(\mathbf{r}, \mathbf{r}_j) = \nabla \times \left( \frac{\boldsymbol{\mu}_e \times (\mathbf{r} - \mathbf{r}_j)}{|\mathbf{r} - \mathbf{r}_j|^3} \right). \quad (3.16)$$

This is the magnetic field from a localised magnetic dipole with dipole moment equal to that of the electron  $\boldsymbol{\mu}_e$  (2.1). Given the magnetic moment of the neutron (3.1), the magnetic interaction potential becomes,

$$\hat{V}_m = -\gamma\mu_N\hat{\boldsymbol{\sigma}} \cdot \sum_j \mathbf{H}(\mathbf{r}, \mathbf{r}_j). \quad (3.17)$$

To calculate the corresponding scattering cross section, (3.17) is inserted in (3.7), yielding

$$\left( \frac{d\sigma}{d\Omega} \right)_{\text{mag}} = \left( \frac{Ym_n}{2\pi\hbar^2} \right)^2 \left| \langle \psi_f, \chi_f, \lambda_f | \hat{V}_m | \psi_i, \chi_i, \lambda_i \rangle \right|^2. \quad (3.18)$$

As we are here dealing with the interaction of the neutron spin with the magnetic correlations in the system, the spin state of the neutron  $\chi$  has been included. Evaluating the spatial part of this is rather complicated, by doing it we arrive at [35],

$$\left(\frac{d\sigma}{d\Omega}\right)_{\text{mag}} = (\gamma r_0)^2 |\langle \chi_f, \lambda_f | \hat{\boldsymbol{\sigma}} \cdot \mathbf{M}_\perp | \chi_i, \lambda_i \rangle|^2. \quad (3.19)$$

$r_0 = 2.818 \cdot 10^{-15}$  m is the classical radius of the electron and  $\mathbf{M}_\perp = \hat{\mathbf{Q}} \times (\mathbf{M} \times \hat{\mathbf{Q}})$  is the part of the Fourier transformed spins,

$$\mathbf{M} = \sum_j \exp(i\mathbf{Q} \cdot \mathbf{r}_j) \mathbf{s}_j, \quad (3.20)$$

that is perpendicular to the scattering vector  $\mathbf{Q}$ . This shows that the neutrons will only scatter with the spin component perpendicular to  $\mathbf{Q}$ . Assuming an unpolarised beam of incident neutrons, it is possible to show that (3.19) becomes [35]

$$\begin{aligned} \left(\frac{d\sigma}{d\Omega}\right)_{\text{mag}} &= \left|\frac{g}{2}F(Q)\right|^2 \exp(-2W) (\gamma r_0)^2 \sum_{\alpha\beta} (\delta_{\alpha\beta} - \hat{Q}_\alpha \hat{Q}_\beta) \\ &\times \sum_{\lambda_i} p_{\lambda_i} \sum_{j,j'} \exp(i\mathbf{Q} \cdot (\mathbf{r}_{j'} - \mathbf{r}_j)) \langle \lambda_i | s_j^\alpha s_{j'}^\beta | \lambda_i \rangle. \end{aligned} \quad (3.21)$$

$\sum_{\alpha\beta}$  is a sum over the x, y, z components of the spins.  $\hat{Q}_\alpha$  refers to the  $\alpha$  component of the scattering vector of unit length.  $p_{\lambda_i}$  is the probability that the sample is in the initial state  $\lambda_i$ . The term in the last sum is the Fourier transform of the spin correlation function. This is sometimes referred to as  $S(\mathbf{Q})$  and this term contains all information about the magnetic structure.

$$F(Q) = \int \mathfrak{s}(\mathbf{r}) \exp(i\mathbf{Q} \cdot \mathbf{r}) d\mathbf{r}, \quad (3.22)$$

is the *magnetic form factor* of the individual magnetic ion, where  $\mathfrak{s}(\mathbf{r})$  is the normalised density of unpaired electrons [35]. The magnetic form factor is a continuous function for which it is true that  $F(0) = 1$  and  $F(Q \rightarrow \infty) = 0$ .

By assuming a static and periodic structure, it is possible to show that scattering from an ordered magnetic system results in delta peaks in reciprocal space. The positions of these, the *magnetic Bragg reflections*, in reciprocal space are calculated in a completely analogous manner to (3.13),

$$\begin{aligned} \left(\frac{d\sigma}{d\Omega}\right)_{\text{magn, el}} &= (\gamma r_0)^2 \frac{N(2\pi)^3}{V_0} \exp(-2W) \left[\frac{g}{2}F(Q)\right]^2 \\ &\times |F_M(\mathbf{Q})|^2 \sum_{\mathbf{G}} \delta(\mathbf{Q} - \mathbf{G} - \boldsymbol{\tau}). \end{aligned} \quad (3.23)$$

### 3.4. Magnetic Scattering

---

Here  $\boldsymbol{\tau}$  is the magnetic ordering vector and  $F_M(\mathbf{Q})$  is the magnetic structure factor. As this project is not concerned with ordered systems, I will not go further into discussing (3.23).

While a static, long range ordered, magnetic system is one extreme on the spectrum of magnetic structures, the other extreme is a paramagnet. Here the spins are completely uncorrelated,

$$\langle \mathbf{s}_j \cdot \mathbf{s}_{j'} \rangle = 0. \quad (3.24)$$

In this case only  $j = j'$  terms contribute in (3.21), yielding

$$\left( \frac{d\sigma}{d\Omega} \right)_{\text{mag}} = \frac{2}{3} N s(s+1) \left| \frac{g}{2} F(Q) \right|^2 \exp(-2W) (\gamma r_0)^2 \quad (3.25)$$

Thus, scattering from a paramagnet does not depend on anything but the magnetic form factor and has no distinct features.

For the case of frustrated materials at  $T > T_N$  the system is somewhere in between the fully ordered case and the completely uncorrelated paramagnet. Nearby spins are correlated, but the correlation dies off with some characteristic correlation length  $\xi$ ,

$$\langle \mathbf{s}_j \cdot \mathbf{s}_{j'} \rangle \propto \exp(-|\mathbf{r}_{j'} - \mathbf{r}_j|/\xi). \quad (3.26)$$

By Fourier transforming this term, it is possible to show that [36]

$$S(\mathbf{Q}) \propto \frac{1}{\frac{1}{\xi^2} + |\mathbf{Q} - \mathbf{G}|^2}. \quad (3.27)$$

This Lorentzian is what appears in the specific case, when the correlation length decreases exponentially with the distance between the spins. Any system with finite correlation length will produce scattering peaks with finite widths. Shorter correlation lengths will lead to broader, more diffuse features.

### Experimental Considerations

In the previous we have arrived at an expression for both the magnetic and nuclear elastic scattering cross sections. There are however several other contributions to the total cross section. First of all, there are inelastic components to both the magnetic and nuclear cross sections. Experimentally, there are ways to look at these exclusively or eliminate them to study just the elastic cross section. In this project, the total cross section is measured.

There are also incoherent contributions to the scattering cross section, giving rise to signals that are isotropic in  $\mathbf{Q}$ . A magnetic contribution, due to uncorrelated spins, an isotope

incoherent contribution due to the local variation in the scattering length and a nuclear spin incoherent contribution.

With all these different contributions, broad and diffuse magnetic features can be very hard to resolve. This problem is further exacerbated by the fact that when doing an experiment, the scattering cross section is not measured directly, but is instead convolved with the resolution function of the instrument. This can be approximated as a convolution with a Gaussian function and this effect also serves to broaden all the features in the scattering signal. Luckily, there is a way to separate magnetic and nuclear scattering. This is done by polarizing the neutron beam.

### 3.4.1 Polarization Analysis

This section is built on [35, 37], both of which provide a more in depth analysis. I will begin by analysing the case where a magnetic field is applied to polarize the neutrons in the  $z$ -direction. As the neutron has  $s = \frac{1}{2}$ , the spin state can be described by the eigenstates to the  $z$ -component of the Pauli spin operator  $\sigma_z$ , given as the spinors

$$|\chi_+\rangle = \begin{pmatrix} 1 \\ 0 \end{pmatrix}, \quad |\chi_-\rangle = \begin{pmatrix} 0 \\ 1 \end{pmatrix}. \quad (3.28)$$

The polarization state of the incident beam is then characterized by the polarization vector

$$\mathbf{P} = \hat{\mathbf{e}}_z \frac{n_+ - n_-}{n_+ + n_-} \quad (3.29)$$

$\hat{\mathbf{e}}_z$  is the unit vector in the  $z$ -direction and  $n$  denotes the number of neutrons in the up or down spin state (3.28).

The magnetic scattering potential can be taken as (3.19) and the nuclear scattering can be taken as (3.13). The latter does not affect the spin state and is thus denoted by a constant,  $b$ , yielding

$$\hat{V} = -\gamma r_0 \hat{\boldsymbol{\sigma}} \cdot \mathbf{M}_\perp + b. \quad (3.30)$$

Using this interaction potential, the transition probability between spin states is then proportional to

$$U = \langle \chi_f | \hat{V} | \chi_i \rangle. \quad (3.31)$$



The matrix elements of which are,

$$U^{++} = \langle \chi_+ | \hat{V} | \chi_+ \rangle = b - \frac{\gamma r_0}{2} M_{\perp z} + \frac{1}{3} b_{si}, \quad (3.32a)$$

$$U^{--} = \langle \chi_- | \hat{V} | \chi_- \rangle = b + \frac{\gamma r_0}{2} M_{\perp z} + \frac{1}{3} b_{si}, \quad (3.32b)$$

$$U^{+-} = \langle \chi_+ | \hat{V} | \chi_- \rangle = -\frac{\gamma r_0}{2} (M_{\perp x} + iM_{\perp y}) + \frac{2}{3} b_{si}, \quad (3.32c)$$

$$U^{-+} = \langle \chi_- | \hat{V} | \chi_+ \rangle = -\frac{\gamma r_0}{2} (M_{\perp x} - iM_{\perp y}) + \frac{2}{3} b_{si}. \quad (3.32d)$$

Here I have also introduced the incoherent scattering contribution  $b_{si}$  for the nuclear spin incoherent scattering. The isotope incoherent part is absorbed into  $b$ . A derivation of these terms can be found in [37].  $U^{++}$  and  $U^{--}$  describes scattering that does not change the spin state of the neutron, so called *non spin flip* (NSF) scattering.  $U^{+-}$  and  $U^{-+}$  describes the other case, when the spin state of the neutron changes, so called *spin flip scattering* (SF).

It is possible to show [37] that these scattering cross sections for a paramagnet or a short range antiferromagnet become

$$\left( \frac{d\sigma}{d\Omega} \right)_{\text{nsf}} = \frac{1}{2} \left( \frac{d\sigma}{d\Omega} \right)_{\text{mag}} \left( 1 - (\hat{\mathbf{P}} \cdot \hat{\mathbf{Q}})^2 \right) + \left( \frac{d\sigma}{d\Omega} \right)_{\text{nuc}} + \frac{1}{3} \left( \frac{d\sigma}{d\Omega} \right)_{\text{si}}, \quad (3.33a)$$

$$\left( \frac{d\sigma}{d\Omega} \right)_{\text{sf}} = \frac{1}{2} \left( \frac{d\sigma}{d\Omega} \right)_{\text{mag}} \left( 1 + (\hat{\mathbf{P}} \cdot \hat{\mathbf{Q}})^2 \right) + \frac{2}{3} \left( \frac{d\sigma}{d\Omega} \right)_{\text{si}}. \quad (3.33b)$$

Here the magnetic and nuclear cross sections are the ones we arrived at earlier (3.21), (3.13).

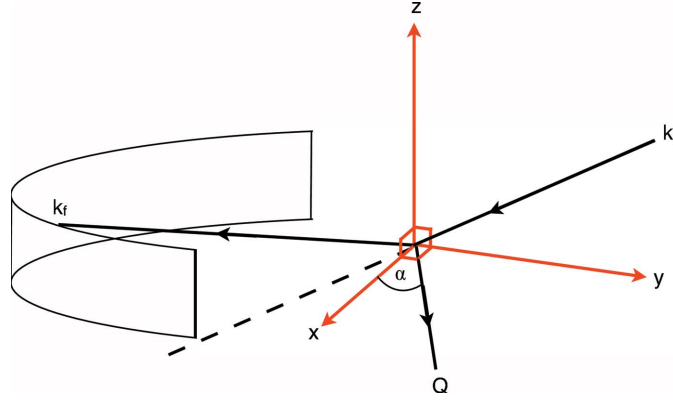
These equations enables a complete separation of the magnetic and nuclear scattering signals, this is done by measuring with neutron polarization along three perpendicular directions,

$$\hat{\mathbf{P}}_x = \begin{pmatrix} 1 \\ 0 \\ 0 \end{pmatrix}, \hat{\mathbf{P}}_y = \begin{pmatrix} 0 \\ 1 \\ 0 \end{pmatrix}, \hat{\mathbf{P}}_z = \begin{pmatrix} 0 \\ 0 \\ 1 \end{pmatrix}. \quad (3.34)$$

If scattering is only measured in the x,y plane (see figure 3.4) the normalised scattering vector is

$$\hat{\mathbf{Q}} = \begin{pmatrix} \cos(\alpha) \\ \sin(\alpha) \\ 0 \end{pmatrix}. \quad (3.35)$$

Where  $\alpha$  is the angle between the scattering vector and the arbitrarily chosen x axis. The setup is shown schematically in figure 3.4.



**Figure 3.4:** Setup for polarisation analysis, the incident neutrons scatter with the sample at the origin into a detector measuring scattering only in the plane. The polarisation is oriented along the x,y and z direction in turn. Figure from [37]

Inserting (3.35) and (3.34) in (3.33) yields the SF and NSF neutron cross section for all three different polarization directions [37]

$$\left(\frac{d\sigma}{d\Omega}\right)_x^{\text{nsf}} = \frac{1}{2} \sin^2 \alpha \left(\frac{d\sigma}{d\Omega}\right)_{\text{mag}} + \frac{1}{3} \left(\frac{d\sigma}{d\Omega}\right)_{\text{si}} + \left(\frac{d\sigma}{d\Omega}\right)_{\text{nuc}}, \quad (3.36a)$$

$$\left(\frac{d\sigma}{d\Omega}\right)_x^{\text{sf}} = \frac{1}{2} (1 + \cos^2 \alpha) \left(\frac{d\sigma}{d\Omega}\right)_{\text{mag}} + \frac{2}{3} \left(\frac{d\sigma}{d\Omega}\right)_{\text{si}}, \quad (3.36b)$$

$$\left(\frac{d\sigma}{d\Omega}\right)_y^{\text{nsf}} = \frac{1}{2} \cos^2 \alpha \left(\frac{d\sigma}{d\Omega}\right)_{\text{mag}} + \frac{1}{3} \left(\frac{d\sigma}{d\Omega}\right)_{\text{si}} + \left(\frac{d\sigma}{d\Omega}\right)_{\text{nuc}}, \quad (3.36c)$$

$$\left(\frac{d\sigma}{d\Omega}\right)_y^{\text{sf}} = \frac{1}{2} (1 + \sin^2 \alpha) \left(\frac{d\sigma}{d\Omega}\right)_{\text{mag}} + \frac{2}{3} \left(\frac{d\sigma}{d\Omega}\right)_{\text{si}}, \quad (3.36d)$$

$$\left(\frac{d\sigma}{d\Omega}\right)_z^{\text{nsf}} = \frac{1}{2} \left(\frac{d\sigma}{d\Omega}\right)_{\text{mag}} + \frac{1}{3} \left(\frac{d\sigma}{d\Omega}\right)_{\text{si}} + \left(\frac{d\sigma}{d\Omega}\right)_{\text{nuc}}, \quad (3.36e)$$

$$\left(\frac{d\sigma}{d\Omega}\right)_z^{\text{sf}} = \frac{1}{2} \left(\frac{d\sigma}{d\Omega}\right)_{\text{mag}} + \frac{2}{3} \left(\frac{d\sigma}{d\Omega}\right)_{\text{si}}. \quad (3.36f)$$

By linear combination of these equations, it is possible to separate the magnetic and nuclear scattering completely from each other.

$$\left(\frac{d\sigma}{d\Omega}\right)_{\text{mag}} = 2 \left(\frac{d\sigma}{d\Omega}\right)_x^{\text{sf}} + 2 \left(\frac{d\sigma}{d\Omega}\right)_y^{\text{sf}} - 4 \left(\frac{d\sigma}{d\Omega}\right)_z^{\text{sf}}. \quad (3.37)$$

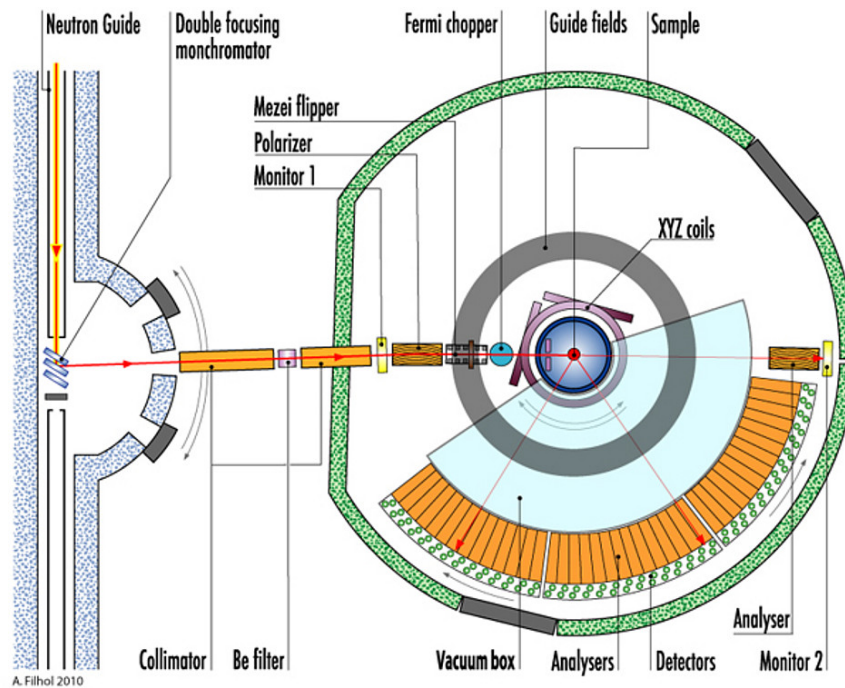
$$\left(\frac{d\sigma}{d\Omega}\right)_{\text{nuc}} = \frac{1}{6} \left[ 2 \left(\frac{d\sigma}{d\Omega}\right)_{\text{Tnsf}} - \left(\frac{d\sigma}{d\Omega}\right)_{\text{Tsf}} \right]. \quad (3.38)$$

Tnsf and Tsf denoting the sum of the non spin flip and spin flip cross section respectively.

It is important to note that these equations are only valid for systems that are not correlated over long distances and that have no ferromagnetic domains. The magnetic field from a ferromagnetically correlated system will depolarise the scattered beam. Similar equations can be obtained for ordered antiferromagnets, but it requires prior knowledge about the magnetic structure factor or that the orientation of  $M$  is known.

### 3.5 D7 - Diffuse Scattering Spectrometer

In this project, measurements have been performed at the diffuse scattering spectrometer D7 at ILL in Grenoble, France [37]. A schematic overview of D7 is presented in figure 3.5. The instrument is designed for measuring diffuse magnetic and nuclear scattering signals and is equipped with full xyz polarization analysis as described above.



**Figure 3.5:** Schematic overview of the diffuse scattering spectrometer D7 at ILL. It has xyz polarization analysis and a detector bank covering  $5^\circ < 2\theta < 150^\circ$ . Figure from [38].

The neutrons travel through the neutron guide from the source, in the case of ILL it is a reactor source. The beam scatters from a monochromator. The monochromator is a piece of pyrolytic graphite, which scatters according to Bragg's law (3.15), such that it is possible to pick a distinct incoming wavelength. On D7 there are three different choices of incoming wavelength (3.1 Å, 4.8 Å, 5.8 Å), accessible via a suitable rotation.

The neutrons then pass through a collimator and, optionally, a beryllium filter. The Beryllium filter serves to eliminate higher order Bragg scattering, i.e. scattering from neutrons with wavelength  $\frac{\lambda}{2}$ ,  $\frac{\lambda}{3}$ ,  $\frac{\lambda}{4}$ , etc.

The polarization analysis begins in the polarizer, which is a polarizing super mirror. They work by exploiting the fact that for a very small range of incident angles, a neutron beam will be polarized when reflecting off a ferromagnetic material [32]. In this case, the polarizer is positioned so it polarizes the beam in the  $z$ -direction.

The Mezei-flipper non-adiabatically flips the spins, whether this is on or not, determines whether spin flip or non spin flip scattering is measured. The sample is surrounded by a guide field in the  $z$ -direction. This is to ensure that the beam stays polarized. The XYZ coils produce a magnetic field that adiabatically rotates the spins into the direction of choice. When the neutron beam scatters off the sample, the spin then either flips or does not, before the guide field rotates it back into the  $z$ -direction.

Scattering is then measured by a detector bank covering  $5^\circ < 2\theta < 150^\circ$ , with mounted supermirror analyzer to measure only one spin polarization. The detector bank is in vacuum to reduce air scattering.

The fermi chopper is only used in spectroscopy mode and as only diffraction data was measured in this project, this is not relevant.

It is not possible to produce detectors, flippers or supermirrors that are 100 % efficient and as the data need to be comparable between detectors, a correction is needed. As vanadium only scatters incoherently for the incident energies in question, a measurement of vanadium will provide a good estimate of the differing intensity between detectors.

For producing a correction of the polarization analysis, a rod of quartz is measured. As quartz is amorphous it scatter homogeneously across the detector bank. More importantly, it has no magnetic or spin incoherent cross section, so there should be no spin flip scattering. The amount of wrongly attributed spin flip scattering in each detector can then be used to correct the data.

These measurements have to be performed before each experiment with both vanadium and quartz the same dimensions as the sample.

It is possible to use a variety of sample environments on D7. In this project we used a standard cryostat capable of reaching a base temperature of around 1.5 K. As well as the uniaxial pressure cell, the details of which I will describe in the next chapter.

# Chapter 4

## Uniaxial Pressure Cell

In this chapter I will describe the uniaxial pressure design and the improvements we made during the project. Furthermore I will detail the calibration process of a load gauge for in-situ pressure measurement. The pressure cell presented in this section has been designed by Lise Sandberg, Malcolm Guthrie, Pascale Deen, Kim Lefmann, Dennis Westphal, Keld Theodor, Jan Oechsle, Alexander Holmes and myself.

The challenges of uniaxial pressure experiments are numerous and difficult to overcome. Many of these difficulties are exacerbated when designing a pressure cell for diffuse magnetic neutron experiments, as this puts further constraints on the choice of materials. Before we get into the specifics of the design process, I will give a brief introduction to mechanical properties of materials under pressure.

### 4.1 Material Properties

All of the concepts discussed here are described in [39]. Consider the stress-strain curve in figure 4.1. The stress, usually denoted  $\sigma$ , is the uniaxial pressure exerted on the sample, in units of Pa.

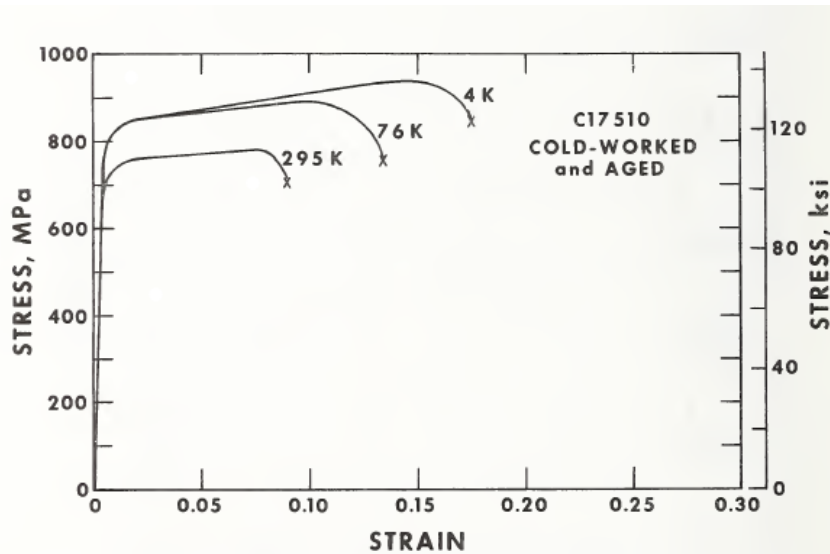
The strain is the deformation that happens to the sample under a given strain and is usually denoted  $\epsilon$ . It is defined as the contraction or expansion of the material, normalised to unloaded length and thus, it is dimensionless.

At low strain, in the elastic regime, the material will contract or expand according to its *Young's modulus* or modulus of elasticity ( $E_Y$ ). This is the willingness of the material to stretch or compress under strain and is given as the slope of the stress-strain curve, in the linear regime

$$E_Y = \frac{\sigma_{el}}{\epsilon_{el}}. \quad (4.1)$$

A material with a large Young's modulus is rigid, whereas a material with a low value

is flexible. At some higher pressure, eventually the elastic regime stops, this pressure is known as the *yield strength*.



**Figure 4.1:** Stress-strain curve for Copper-Beryllium C17510, at three different temperatures. Looking at the 295 K curve, the material deforms elastically up to the yield strength of around 700 MPa. It then deforms plastically up to the ultimate strength just below 800 MPa before failing at  $\epsilon \approx 0.1$  and  $\sigma = 700$  MPa. Figure from [40].

Yield strength, also known as the elastic limit, is the total pressure that can be exerted on a material before it starts deforming permanently. This is the point where the stress-strain curve (figure 4.1) stops being linear. This is one of the main quantities of interest when choosing materials for the pressure cell, as this is what determines the maximum load.

When the stress is increased above the yield strength, the material will start deforming plastically. In this regime, the deformation is irreversible. It should be noted that this curve may look different for compression and elongation. The yield strength is noted for relevant materials in table 4.1. It should be noted that these values are just approximate as impurities may cause them to vary quite dramatically.

The *Poisson effect* refers to an effect that causes a material to expand in the direction perpendicular to the compressive stress. It is described by the Poisson ratio, the ratio between the transverse and longitudinal strain,

$$R_P = -\frac{\epsilon_t}{\epsilon_l}. \quad (4.2)$$

This ratio is different for different materials, for non-isotropic materials it may even be different in each of the directions perpendicular to the strain. There are theoretical models to calculate this for different materials, but they are not very accurate and  $R_P$  has to be

determined experimentally.

This effect means that uniaxial pressure will distort the pressure cell in all three dimensions, possibly introducing a pressure dependent component to the neutron background.

Material	Maximum yield strength (MPa)
Copper Beryllium 25 AT	1350
Stainless Steel AISI 316 [41]	290
Titanium grade 2 [42]	448
Tungsten Carbide (WC) [43]	6833

**Table 4.1:** Maximum yield strength of relevant materials. For Tungsten Carbide, the compressive strength is noted. A data sheet for CuBe 25 can be found in appendix B.

## 4.2 Cell Version 1

The initial version of the cell design, shown in figure 4.2 is largely based on existing diamond anvil cell designs.

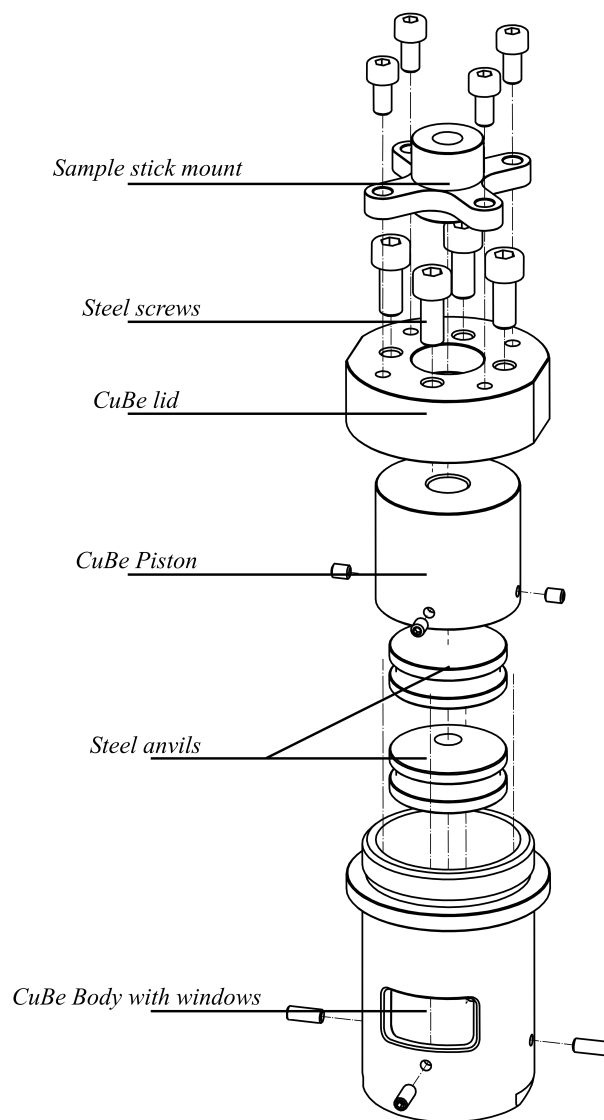
The sample is placed between the anvils and pressure is applied with a hydraulic press, pushing down on the piston through the hole in the lid. The screws in the lid are then tightened to hold the piston down and thus keep pressure constant, after which the hydraulic press is released. The cell can then be placed on a neutron beamline and the pressure will remain constant throughout the experiment. The dimensions of the pressure cell are carefully chosen to fit inside an Orange cryostat.

Before choosing materials for the pressure cell, it is necessary to estimate how much pressure is needed. To induce the  $M_{||}$  phase transition in DTO, described in section 2.3.2, a minimum pressure of  $\sim 1.5$  GPa is needed. To induce the ferromagnetic phase transition, we need to go to 3.4 GPa. We therefore aim for a minimum pressure of around 3 GPa. While this is not enough to induce the ferromagnetic state, it is hopefully a realistic goal. As a good safety margin is required to operate the cell at neutron facilities, the cell will have to be able to withstand 1.5 times that pressure without breaking. We imagine the cell will be used with a cylindrical sample with dimensions  $h = 3$  mm and  $d = 3$  mm. This means that the body of the cell has to withstand a force of

$$F_{max} = 4.5 \text{ GPa} \cdot \pi(1.5 \text{ mm})^2 = 32 \text{ kN}. \quad (4.3)$$

Furthermore, the material chosen for the body has to be non-magnetic. The polarization analysis described in the earlier chapter is completely dependent on there being no

ferromagnetic couplings in the neutron beam.



**Figure 4.2:** The first design for the pressure cell, the cell is made from CuBe and steel. This design has windows at the sample position to ensure a good signal strength.

For this reason, the body is machined from Copper-Beryllium 25 AT (CuBe) (Appendix B). CuBe is a copper alloy widely used in industry for making high durability tools. It was chosen because of the high yield strength (after heat treatment) of 1350 MPa, as well as for being non-magnetic. It does have one significant drawback, namely that the



incoherent scattering cross section of copper is not particularly low [28] and thus will produce quite a large background, as well as possible attenuate the neutron beam significantly. For these reasons, the cell has two 70° windows to ensure a broad Q-region of transmission.

The anvils are the parts of the cell that need the largest yield strength, as they are in direct contact with the sample and thus. Their yield strength should be at least 4.5 GPa. Furthermore the anvils have to be extremely flat, to reduce the risk of the sample breaking. These requirement turns out to be very difficult to satisfy at the same time. Materials with yield strengths of that magnitude are extremely hard to come by and very difficult to machine.

In the first iteration of the cell design, this decision was postponed and seats of steel 316 were machined. This was chosen due to steel being readily available, easy to machine and cheap. With a yield strength of up to 290 MPa, this is not nearly enough to achieve the pressure needed to induce the phase transition. They are however sufficient to start testing the theory, as the scattering signal of HTO is predicted to change continuously with pressure. Table 4.2 contains the maximum applied force the critical components of the cell can withstand, as well as the sample pressure that this corresponds to.

Neutron measurements performed with this cell design is presented in chapter 5. These measurements led to several changes in the design.

Component	Material	Maximum Force (kN)	Sample Pressure (GPa)
Screws	Steel 316	22.6	3.2
Cell walls	CuBe Alloy	272.1	38.5
Anvils	Steel 316	2.05	0.3

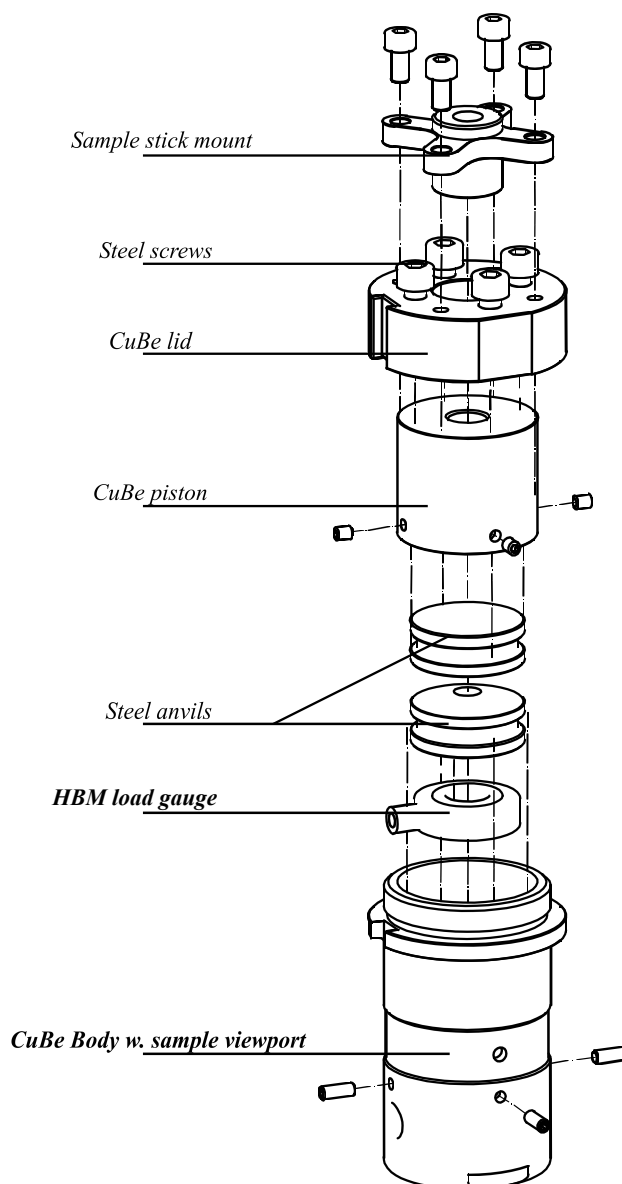
**Table 4.2:** The force at which the critical components of cell v1 will yield and the corresponding pressure that is achievable on a cylindrical sample with diameter  $d = 3$  mm.

## 4.3 Cell Version 2

The second cell design, presented in figure 4.3, was constructed to combat the most critical issues from the initial neutron experiment with the first pressure cell. These measurements proved rather inconclusive, this was mainly due to two things:

- First, the windows in the cell walls proved to do more harm than good, as they introduced artefacts in the data. The extensive data correction that was needed made it difficult to deduce much about HTO under pressure. However, the CuBe body proved to be transparent enough that the windows could just be eliminated. Instead, the thickness of the cell wall was reduced around the sample position from

3 mm to 1.5 mm to reduce attenuation and background. With this change, the cell walls will yield at an applied force of 213.1 kN, corresponding to a sample pressure of 30.1 GPa, well above the requirement. Thus it is still the steel anvils that are the limiting factor.



**Figure 4.3:** The second version of the cell design. A space for a commercial HBM load gauge has been added. Furthermore the windows have been removed, and in their place, the wall thickness is reduced around the sample position. New components and components that have been changed are in bold.

- Second, the thermal contraction of the cell and the sample after cooling, meant that the applied pressure was actual unknown during the measurement. A method for measuring in-situ pressure at low temperature is therefore needed. In industry,

a variety of load gauges are used, but none are designed for use at cryogenic temperatures. Even so, we first settled on using a commercially available 40 KMR load gauge from HBM [44]. It has a strain gauge based setup, the details of which are unknown as that is proprietary information. The calibration process of this load gauge is described in [45]. Unfortunately the gauge turned out not to be able to withstand the continued thermal cycling and thus this iteration of the design had no functioning load gauge. The body of the pressure cell was also extended to accommodate the load gauge. It is placed in the bottom of the cell because the length of the piston is carefully determined to ensure that the sample will be at the beam-height.

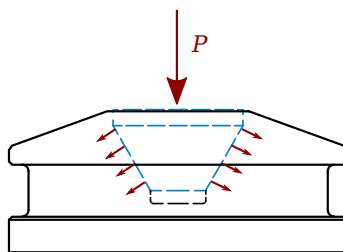
As the steel anvils did not break during the first experiments, these were kept for the next version of the cell. A neutron experiment was performed with this cell design, it is presented in chapter 6

### 4.4 Cell Version 3

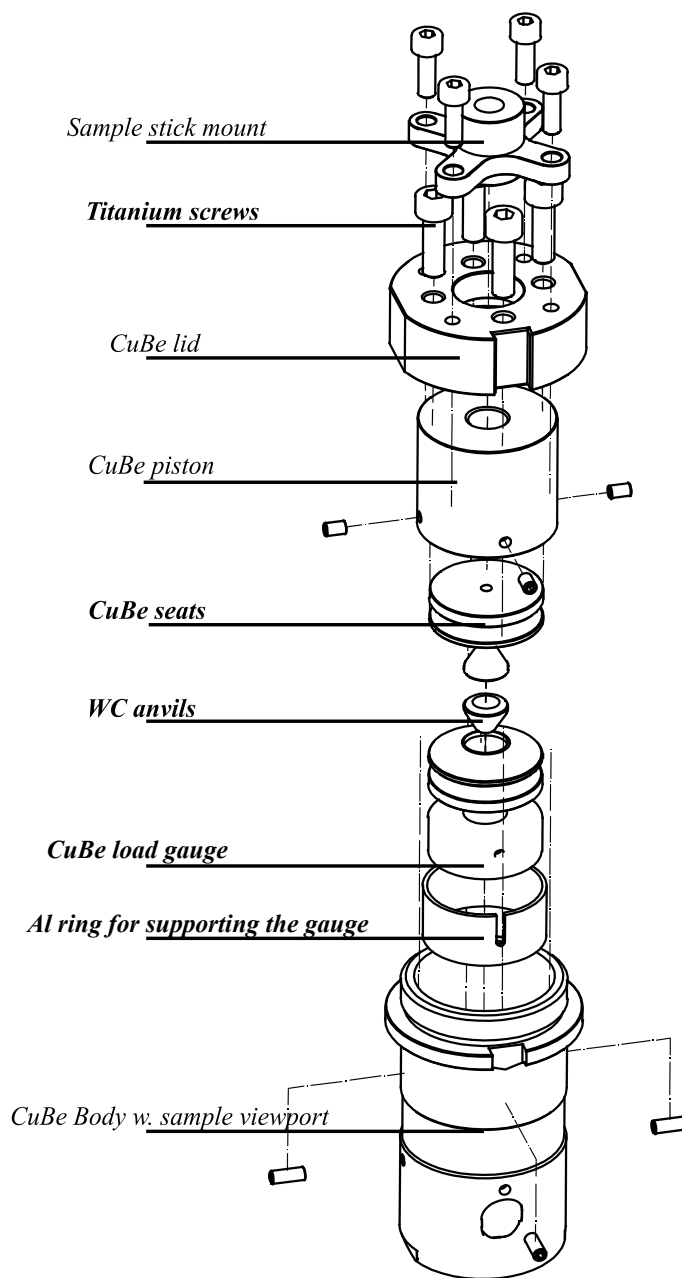
The second set of neutron measurements were much more promising than the first, as the cell background proved largely homogeneous. There were, however, issues with the steel anvils indenting and the pressure was still highly uncertain.

The third and so far final iteration of the cell design is largely identical to the second version and is presented in figure 4.5. There are however, two significant difference. New seats have been designed and the softer steel seats are changed for a new seat design with a CuBe cage and an anvil made from cemented Tungsten Carbide (WC).

WC has a compressive yield strength of upwards of 7 GPa [43], making it hard enough to achieve the pressures required to induce the phase transitions in HTO. The idea behind the design is that the pressure is distributed evenly into the CuBe cage, as depicted in figure 4.4, preventing it from deforming permanently.



**Figure 4.4:** CuBe cage with WC seats (dashed blue). When pressure is applied to the WC seat, it is distributed evenly into the CuBe cage.



**Figure 4.5:** The pressure cell design v3. A load gauge is constructed and added to the cell, to allow in-situ pressure measurements. The steel anvils are here changed for the much harder WC anvils. New components and components that have been changed are in bold.

Additionally, a new load gauge is designed. It is built on a strain gauge based set-up, just as the HBM gauge. The difference is that this is designed using strain gauges that are designed for cryogenic temperatures [46]. The details of the design and calibration is presented in the next sections. The screws, holding the pressure constant is changed for identical titanium screws. Titanium is non-magnetic and has a higher yield strength. The forces at which the critical components of this design fails can be found in table 4.3.

## 4.5. Load Gauge

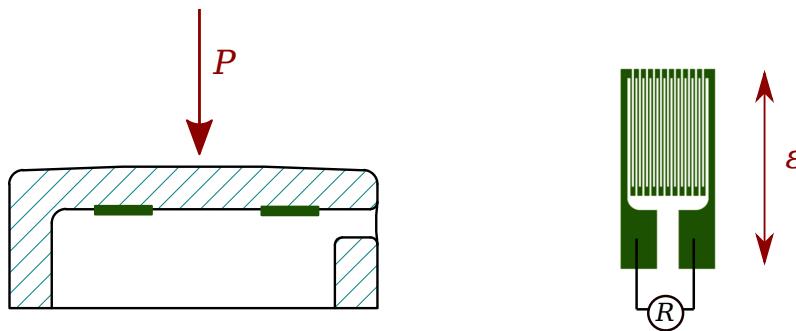
This means that we should have achieved our goal of being able to go to approximately 4.5 GPa. Keep in mind that these numbers are the best case value of the yield strength so the actual components may very well have small impurities that reduces the maximum force achievable quite a lot. The limits could however quite easily be pushed further by using a higher grade titanium for the screws. The complete set of drawings of each of the components are presented in Appendix C.

Component	Material	Maximum Force (kN)	Sample pressure (GPa)
Screws	Titanium grade 2	35.2	4.9
Cell Walls	CuBe 25 AT	213.1	30.1
Load Gauge	CuBe 25 AT	106.0	15.0
Anvils	Tungsten Carbide	48.3	6.8

**Table 4.3:** The force at which the critical components of cell v3 will yield and the corresponding pressure that is achievable on a cylindrical sample with diameter  $d = 3$  mm.

## 4.5 Load Gauge

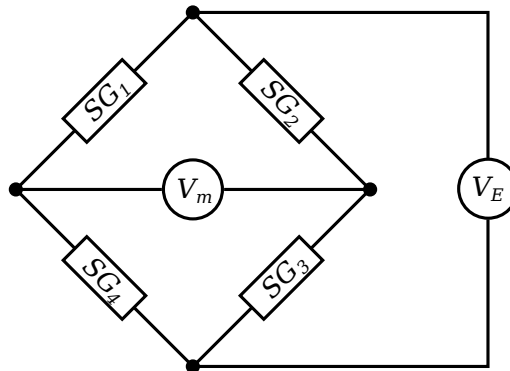
The load gauge consists of a CuBe cage with four mounted strain gauges. Strain gauges are resistors, designed to change resistance when under strain in one direction, while being much less sensitive to strain in the perpendicular direction. Both the CuBe cage and a strain gauge are depicted schematically in figure 4.6.



**Figure 4.6:** The CuBe cage (left), with mounted strain gauges (marked in green), the hole in the side is for the wiring. Pressure is applied from above, the resulting strain on the strain gauge (right) changes the measured resistance. Only strain applied along the length of the wires will change the resistance significantly.

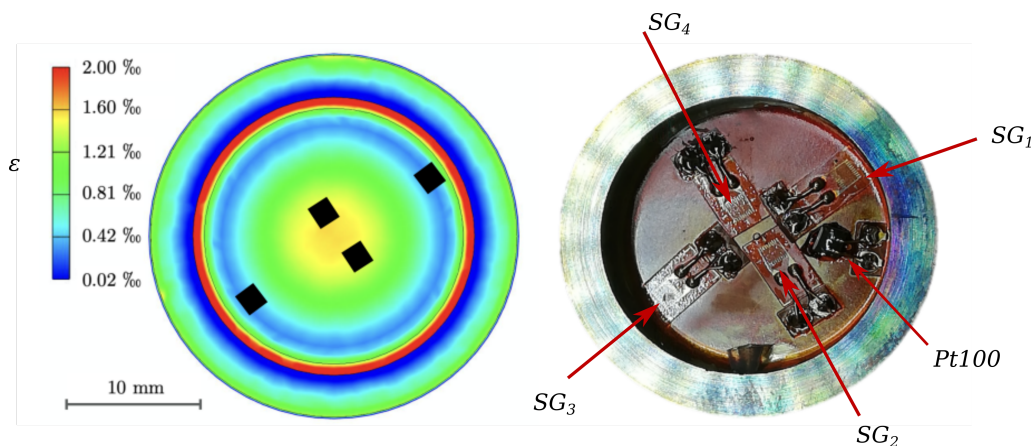
The strain gauges used are manufactured by Tokyo Measuring Instruments Lab. and are of the type CFLA-1-350 they are designed to work at cryogenic temperatures and are tested down to 4 K, they are glued onto the CuBe cage using a cryogenic glue (type C-1) [46,47].

The strain gauges (SG) are arranged in a Wheatstone bridge, one is depicted in figure 4.7. It consists of four resistances, in this case strain gauges, connected in the manner depicted.



**Figure 4.7:** A Wheatstone bridge, consisting of four strain gauges (SG). They are placed on the CuBe cage so that when a pressure is applied, they experience a strain. An excitation voltage ( $V_E$ ) is applied across the bridge and the response is measured as the relative voltage  $\frac{V_m}{V_E}$ .

A constant excitation voltage ( $V_E$ ) is applied and the voltage drop across the bridge is measured ( $V_m$ ). The load gauge response is then the relative voltage  $\frac{V_m}{V_E}$ . If the bridge is balanced, meaning that the unloaded resistance of all the strain gauges are the same the unloaded signal will be zero. When stress is then applied, the induced strain will change the resistance in the gauges, offsetting the bridge. The Wheatstone bridge set-up was originally designed to determine the value of an unknown resistance accurately, but is useful when measuring strain as even small deviations from strain will cause the signal to deviate from zero [48].

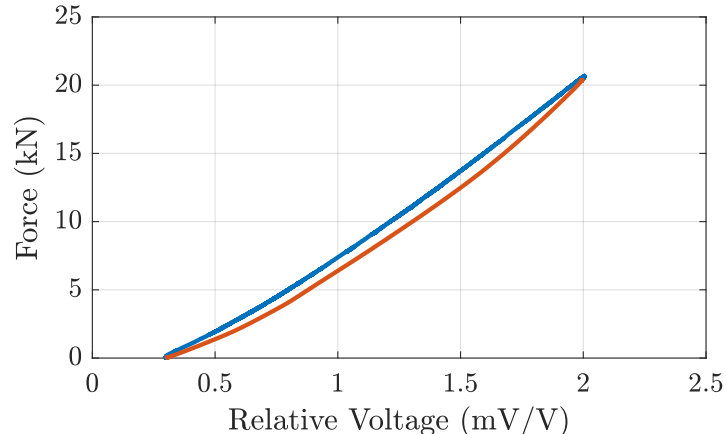


**Figure 4.8:** Finite element analysis showing the strain on the CuBe cage under 2 tonnes of force (left), the positioning of the strain gauges are shown in black. Picture of the load gauge taken before the wiring is done (right). The strain gauges are mounted next to a pt100 thermometer.

The gauges are carefully placed so that pressure applied to the centre of the CuBe cage will only result in strain along the gauges. A picture taken from the bottom of the load gauge, before it was wired, is shown to the right in figure 4.8. A finite element analysis has since been performed by Karl-Emil Nielsen at the workshop at NBI to test whether the gauges are placed ideally. The resulting figure, including the chosen strain gauge positions can be seen in figure 4.8. The strain gauges operate optimally around  $\epsilon = 1 \text{ ‰}$ , evidently they are not placed optimally. However, as we shall see in this section, the signal is strong enough with the current placement and we decided to keep it this way. A Pt100 thermometer was also placed on the bottom of the gauge for monitoring the temperature during testing. The signal from this, as well as the relative voltage is measured using the HBM Quantum MX440B universal measuring amplifier [49].

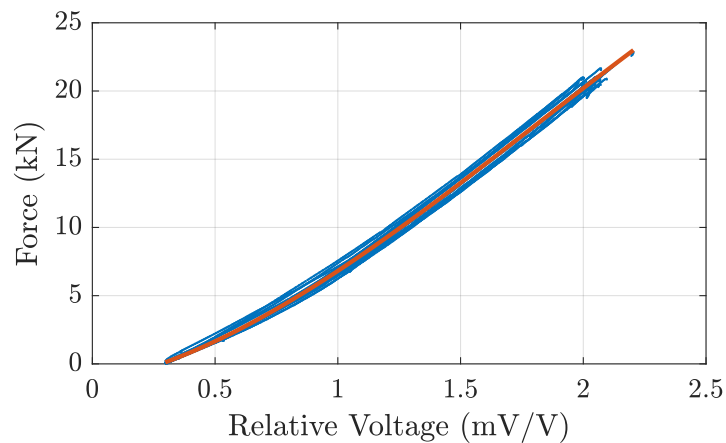
### 4.5.1 Room Temperature Calibration

This load gauge design has to be calibrated to translate the measured relative voltage to an applied force. To do this, force is applied with a hydraulic press, while the corresponding relative voltage is measured. The accuracy of the press is not known, so a commercially available load gauge is utilised as a reference measurement.

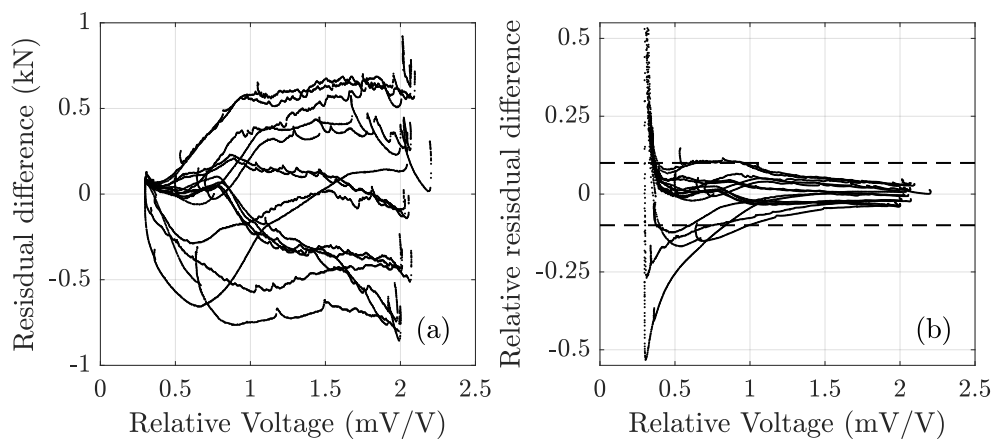


**Figure 4.9:** Applied force plotted as a function of relative voltage for one pressure cycle, increasing pressure (blue) and decreasing (orange). The gauge exhibits a small amount of hysteresis, on the order of 1 kN.

All the measurements are performed with the load gauge inside the cell. This is done to ensure that pressure is applied as precisely as possible to the centre of the gauge, as we discovered that misalignment changed the response quite dramatically. To combat this, we developed a method for centralising the gauge in the cell. When the gauge is centralised there is approximately 2.5 mm to each cell wall and thus four 2.5 mm drills proved ideal as spacers, to control the centralisation.



**Figure 4.10:** Room temperature pressure calibration measurements of the load gauge. The data has been fitted with a 3rd order polynomial, the parameters of which can be found in table 4.4.



**Figure 4.11:** The absolute residual difference between the data and the fit (a). The relative residual difference between the data and the fit (b). The  $\pm 10\%$  zone has been marked with dashed lines.

In figure 4.9, the applied force is plotted as a function of relative voltage for one such measurement, for both increasing and decreasing force. It is evident that there is a small amount hysteresis in the gauge, on the order of 1-2 kN. This is a little unfortunate, but virtually unavoidable as it is an inherent property of most materials. This measurement was repeated three times. The gauge was then removed from the cell and re-centralised. This process is repeated five times, resulting in 15 pressure cycles. The curves are split into increasing and decreasing pressure, the increasing part is plotted in figure 4.10. The data has been fitted with a third order polynomial, of the form

$$F = aV_R^3 + bV_R^2 + cV_R + d. \quad (4.4)$$



## 4.6. Temperature Calibration

Temperature (K)	$a$	$b$	$c$	$d$
296	$-1.07 \pm 0.02$	$5.77 \pm 0.08$	$3.52 \pm 0.08$	$-1.42 \pm 0.03$
195	$-0.399 \pm 0.003$	$3.887 \pm 0.011$	$5.739 \pm 0.011$	$-1.788 \pm 0.003$
125	$-1.795 \pm 0.010$	$7.98 \pm 0.03$	$4.22 \pm 0.03$	$-1.308 \pm 0.009$
77	$-1.005 \pm 0.011$	$5.21 \pm 0.04$	$6.77 \pm 0.03$	$-1.740 \pm 0.010$

**Table 4.4:** Fit Parameters of 3rd degree polynomial fit to the calibration data presented in figures 4.10 and 4.14.

Here  $F$  is the applied force in kN and  $V_R$  is the relative voltage in units of  $\frac{mV}{V}$ . The parameters to this fit can be found in table 4.4. In figure 4.11a, the residual difference between the fit and the data is plotted. It is evident that the systematic error related to the alignment of the applied force is much larger than the statistical error associated with the measurements. The error is no larger than 1 kN. By plotting the calculating the relative residual difference (figure 4.11b) it is clear that the residuals more or less all fall within the 10 % boundary. In the high pressure limit, they all fall within 5 %. This is an encouraging result as this indicates that we will be able to estimate the pressure with a fairly high precision.

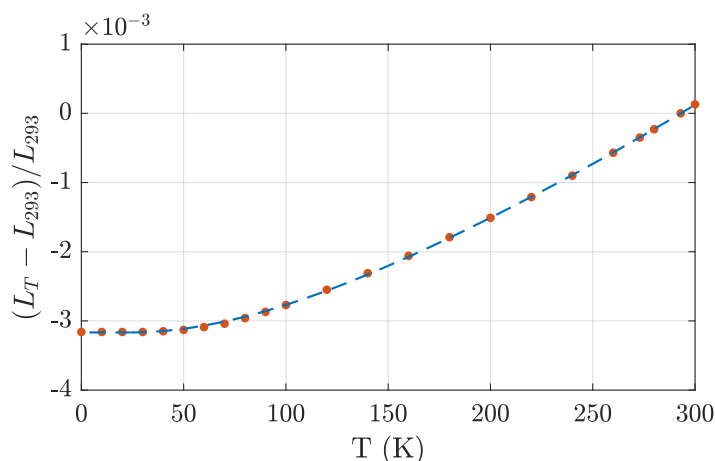
## 4.6 Temperature Calibration

The cell is to be used down to 1 K and when cooling, the sample and the cell will both contract, most likely at different rates, this will change the pressure. Thus a temperature calibration of the load gauge is required to be able to accurately determine this change.

When cooling there are several effects that will change the response of the load gauge gauge:

- The resistance of the strain gauges will change. This will most likely lead to a change in both the unloaded offset and the pressure response. This effect is expected to be rather small, as the gauges are designed for cryogenic temperatures, they are likely made from an alloy that has a weak temperature dependence of its resistivity. This is confirmed by measuring the resistance as a function of temperature (Appendix D).
- The CuBe cage will contract according to the curve in figure 4.12, resulting in a change in the unloaded offset. This change is not too much of an issue as this offset can easily be determined by measuring the unloaded response as a function of temperature which just requires a cryostat.

- Lastly the modulus of elasticity of CuBe changes with temperature as well. This change means that the response of the load gauge will change as a function of temperature. For this reason a measurement of the response from the unloaded gauge as a function of temperature is not sufficient. A pressure curve is needed at low temperature, i.e 1.5 K to be able to accurately determine the pressure. This was however not possible in this project.



**Figure 4.12:** Thermal contraction of CuBe plotted as the relative length change of a block of CuBe between temperature  $T$  and 293 K. The points are data [50], the line is a fit from [51].

#### 4.6.1 LN<sub>2</sub> Calibration

To probe the low- $T$  properties of the pressure cell, we make the assumption that the elasticity of CuBe will not change much below liquid Nitrogen (LN<sub>2</sub>) temperature of 77 K. This is a reasonable postulate as this is the case for a wide range of materials, including Copper [40], the primary constituent of CuBe. Furthermore the thermal contraction of CuBe (figure 4.12) clearly stops around this temperature. If this is the case it should be sufficient to take a pressure curve at 77 K and use that to determine the pressure at very low temperatures.

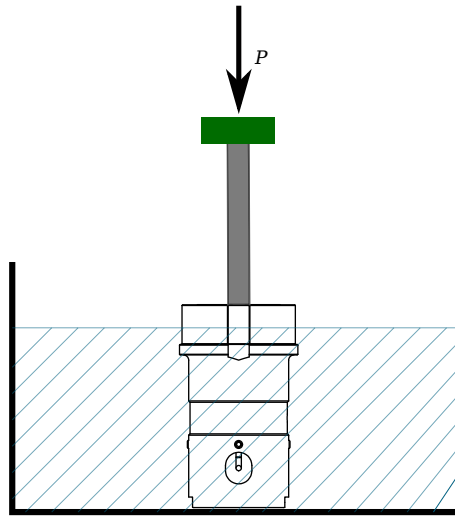
These calibration measurements was performed by Lise Ørdu Sandberg using the set-up in figure 4.13. The pressure cell containing the load gauge was submerged in liquid Nitrogen. The temperature is measured using the Pt100 thermometer,

Pressure is applied with a stainless steel rod with the commercial gauge mounted at the top. This ensures that there is a weak thermal link between the cell at 77 K and the commercial gauge at room temperature, providing the reference measurement.

Pressure curves are taken at 77 K as well as at 125 K, while heating.

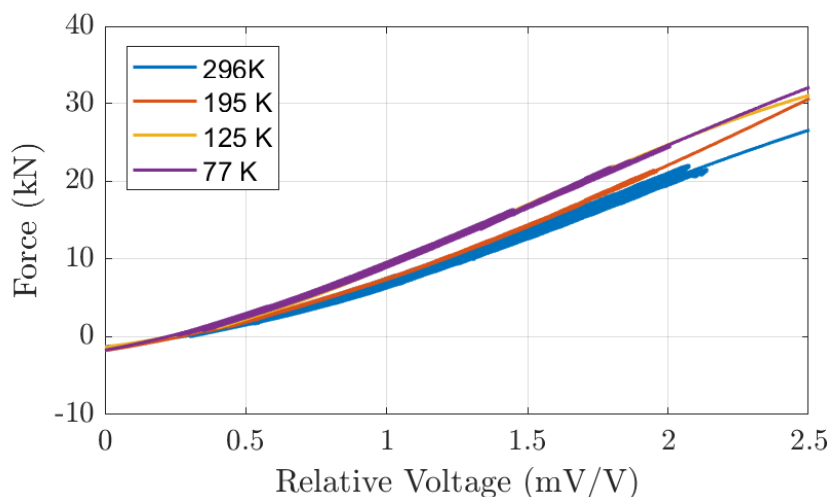
#### 4.6. Temperature Calibration

The temperature changed slowly enough that it was possible to obtain an additional curve without the temperature drifting more than a couple of K.



**Figure 4.13:** The set-up used when measuring pressure calibration curves. The cell is submerged in liquid Nitrogen or dry ice and once equilibrium temperature is reached, pressure is applied using a stainless steel rod mounted on a hydraulic press. The steel rod serves to reduce the thermal link between the sample and the commercial gauge mounted at the top of the rod.

Additionally, a pressure curve was taken with the same set-up, except that LN<sub>2</sub> was changed for dry ice, giving T = 195 K. All of these curves with associated fits are shown in figure 4.14.

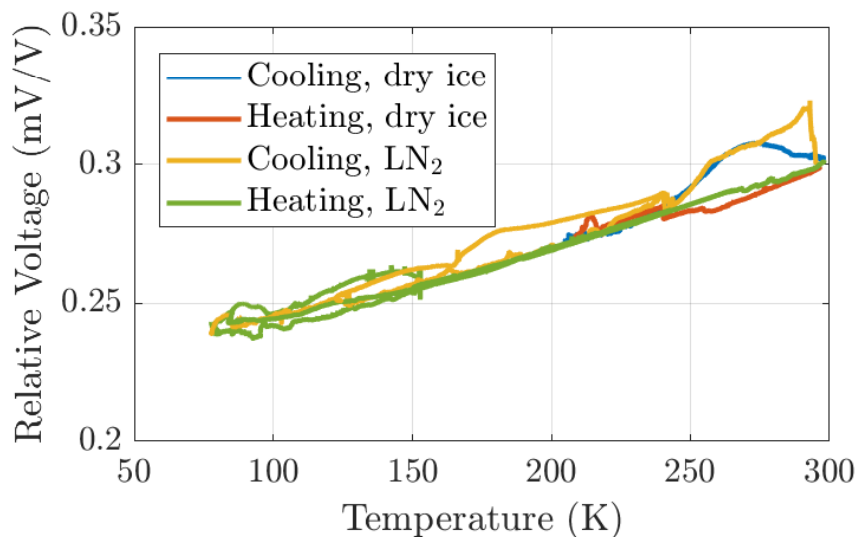


**Figure 4.14:** Pressure curves taken at 296 K, at 195 K (Dry ice), 77 K (LN<sub>2</sub>) and 125 K. The latter temperature curve is almost hidden behind the 77 K data. It was achieved as an intermediate step while the LN<sub>2</sub> was evaporating, it is thus not an entirely stable temperature estimate.

These measurements show that the curve changes quite dramatically down to 77 K. The majority of the change happens above 125 K as the curve changes very little between 125 K and 77 K. In fact the 125 K and 77 K curves are right on top of each other. This further corroborates the fact that the Young's modulus of CuBe is more or less constant at low temperatures.

The same set-up was used to measure the unloaded offset as a function of temperature, as plotted in figure 4.15. The data is very noisy, which is likely a result of the very fast and inhomogeneous cooling, caused by submerging the gauge in the coolant. This is supported by the fact that the cooling curves are much more noisy than the heating curves. The offset change is quite small compared to the effect of pressure, at least in the temperature range measured here.

To further investigate the behaviour of the gauge at lower temperatures, measurements are performed in a cryostat.



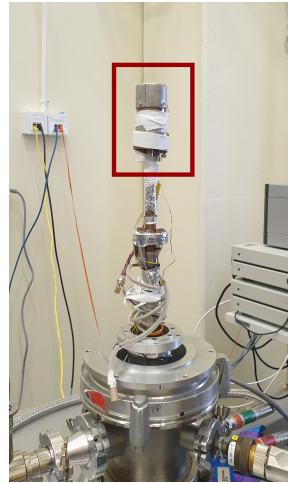
**Figure 4.15:** Gauge response at ambient pressure as a function temperature. The response is also measured upon submerging the load gauge in LN<sub>2</sub> and dry ice. The temperature is measured with a pt100 sensor attached to the load gauge.

#### 4.6.2 CCR Calibration

To go to lower temperatures, a closed-cycle-cryostat is utilised. It has a base temperature of around 20 K, depending on the thermal mass of the sample and the thermal link between the cold head and the sample. As previously stated, it is not possible to get pressure curves at these lower temperatures, as there is no way of changing the pressure in-situ. Instead, we will gain insight by applying pressure at room temperature and measuring the relative

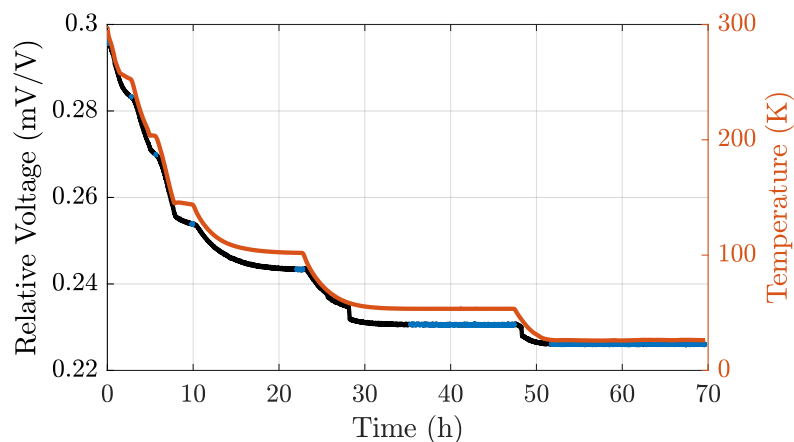
#### 4.6. Temperature Calibration

voltage at low temperatures. The gauge is placed in the cell, which is attached to the cold head as shown in figure 4.16.



**Figure 4.16:** The pressure cell (red square) mounted on the CCR. The temperature is measured with a thermometer on the bottom of the cell.

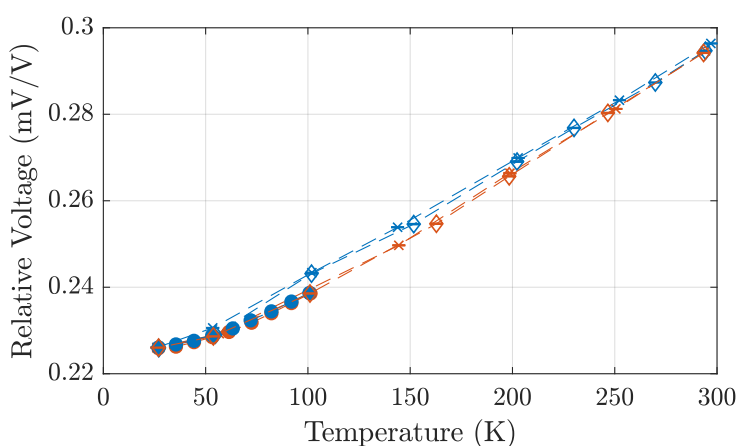
Initially the response from the load gauge is measured unloaded. One ramp between 300 K and 26 is presented in figure 4.17.



**Figure 4.17:** load gauge response and sample temperature as a function of time. The data marked in blue is where the response from the load gauge has stabilised.

On the left axis, the load gauge response is plotted and on the right the temperature of the sample. Looking at the temperature curve, it is evident that the cell was very slow to thermalise. At first we believed that this was because of the large thermal mass. After finishing the unloaded measurements, it became apparent that the thermal contact between the cell and the cold head had been, due to some screws not being tight enough.

Two full temperature cycles were measured, in addition to one at a 10 K increment between 100 K and 26 K.



**Figure 4.18:** Unloaded temperature calibration curve of the load gauge between 300 K and 26 K, decreasing temperature (blue) and increasing (orange). There appears to be a slight hysteresis in the response, though this may be an effect of the very poor thermal contact.

For each temperature setting, the part of the data where the temperature had stabilized was chosen (shown in blue in figure 4.18) and the average was taken. The resulting data is plotted in figure 4.18.

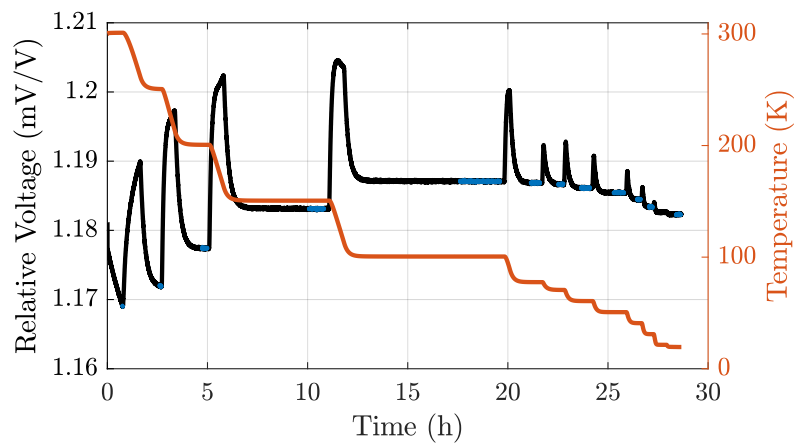
These measurements are completely consistent with the LN<sub>2</sub> measurement in figure 4.15 and also support the assertion that the rapid fluctuations in the LN<sub>2</sub> measurements, were only due to the very rapid and irregular cooling. The curve in figure 4.18 appears to be linear down to around 70 K and then flattens slightly.

This is also consistent with the thermal contraction of CuBe (figure 4.12). As expected, this indicates that the change in the unloaded offset is mainly caused by the thermal contraction.

While we are not able to obtain a pressure curve at base temperature, we are able to test whether it is likely that the Young's modulus of CuBe changes a lot between 77 K and 20 K. To do this, a loaded measurement has to be performed. A pressure of 8.9 kN is applied and a temperature cycle is measured, the time series is plotted in figure 4.19.

Interestingly, this curve looks very different from the unloaded curve in figure 4.17. It is clear that the thermal contact was much better this time, since the temperature curve stabilizes much faster than in the unloaded case. Additionally, when the temperature is changed the pressure increases quite a lot before falling back down and stabilizing. This is believed to be because of the thermal gradient across the cell. As the cold-head cools down very rapidly, this causes the adjacent part of the cell to also cool and thus contract, much more rapidly than the part of the cell furthest from the cold head. This causes the pressure to increase.

As this gradient disappears when the entire cell reaches a common temperature, the pres-



**Figure 4.19:** Load gauge response and sample temperature as a function of time. A force of 8.9 kN was applied at room temperature. As the thermal link between the cold head and pressure cell was better this time, resulting in a lower base temperature of 20 K.

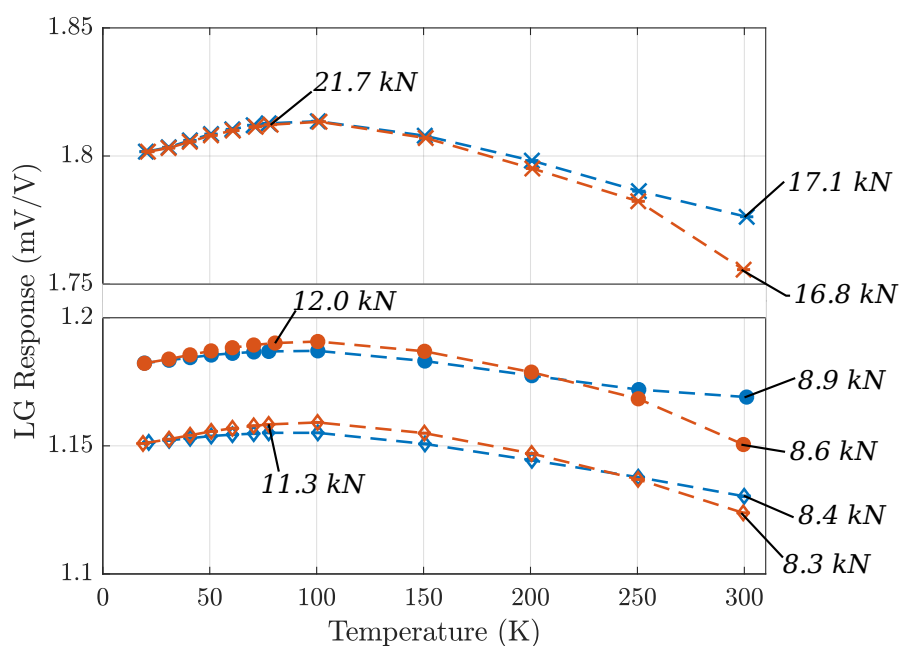
sure drops again, stabilizing at a new value.

From figure 4.19 it is also apparent that the pressure drifts quite a lot at 300 K. This drift disappears at lower temperature, an explanation is given in section 4.6.3.

Three measurements are performed and as before, data is chosen based on when the load gauge has stabilised. The resulting curves are plotted in figure 4.20. Initially a force of 8.9 kN is applied to the cell. Contrary to the unloaded case, the relative voltage increases down to around 100 K. This corresponds to the pressure inside the cell increasing due to the thermal contraction of the cell components. At 77 K the applied force has increased to 12.0 kN.

Below 77 K the relative voltage changes only changes  $0.08 \frac{\text{mV}}{\text{V}}$ , exactly the same amount as the change in the same temperature range in the unloaded case (figure 4.18). This leads me to conclude that the change in the relative voltage in this regime does not correspond to a change in the pressure or in the elasticity of the load gauge. Instead, the change is a result of the thermal contraction of the load gauge and the temperature dependence of the resistivity in the strain gauges.

Upon heating to 300 K the pressure has drifted to 8.6 kN. Another curve is therefore taken without extracting the cell to test the reproducibility of the result. Once the pressure has decreased to 8.4 kN another curve is measured showing exactly the same behaviour. Lastly, the cell is extracted from the CCR and a force of 17.1 kN is applied, increasing to 21.7 kN at 77 K. This curve shows exactly same behaviour, confirming that the gauge is not deforming permanently and the thermal cycling has not broken the gauge either.



**Figure 4.20:** Temperature curves for three different applied pressures between 300 K and 20 K. Decreasing temperature (blue) and increasing (orange). The applied force noted is calculated at 300 K and 77 K using the curves in figure 4.10.

With these measurements, it is reasonable to postulate that the 1 K pressure can be estimated accurately using the 77 K pressure curve, the parameters of which can be found in table 4.4. I estimate, based on the relative residual difference that the pressure can be determined with a 10 % error. This is just a rough estimate and I believe additional pressure curves should be taken at 77 K to investigate this.

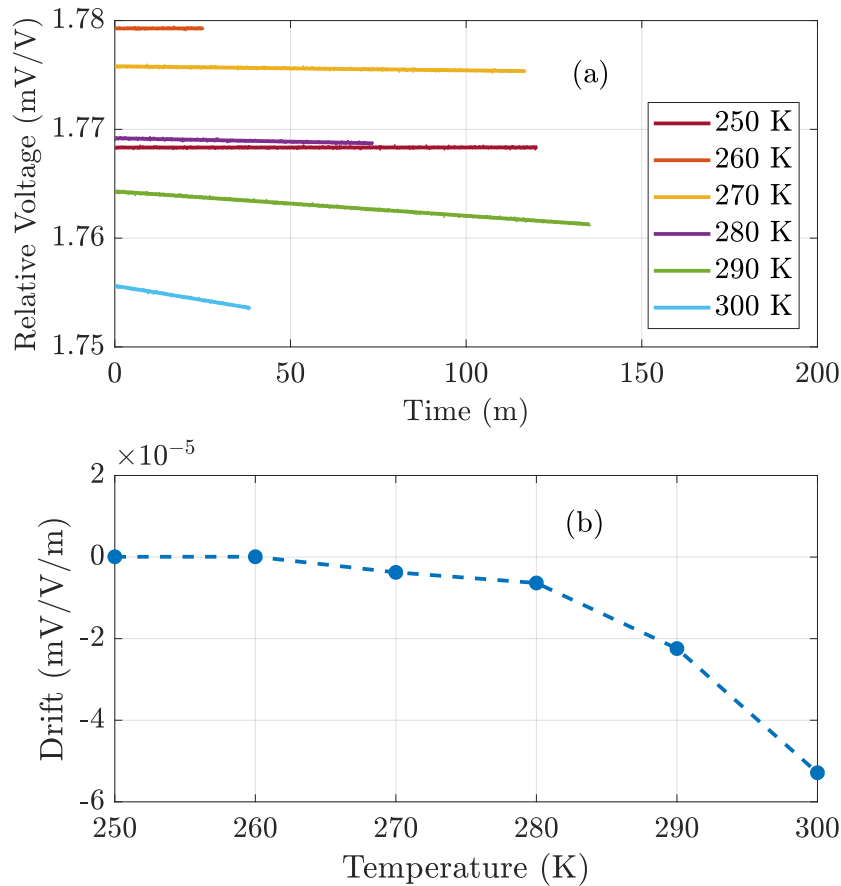
These measurements were performed with the steel anvils in the cell, meaning that the large increase in pressure inside the cell upon cooling may not be a feature of the new cell design with the CuBe - WC anvils.

### 4.6.3 High Temperature Drift

The high temperature drift, observed in figure 4.19 seems rather mysterious, however, the fact that the drift disappears at lower temperature is a significant clue as to what could be causing it. Initially, I believed that the load gauge or some other part of the pressure cell was deforming permanently. As yield strength usually increases at lower temperature, this would explain why the drift disappears when cooling. There are, however, two reasons that this seems rather unlikely. First, the forces were not nearly high enough to be close to the yield strength of any of the cell components. Second, upon careful examination of all the cell components, I found no evidence of deformation. If the load gauge had deformed,



this would also have appeared as a change in the unloaded offset.

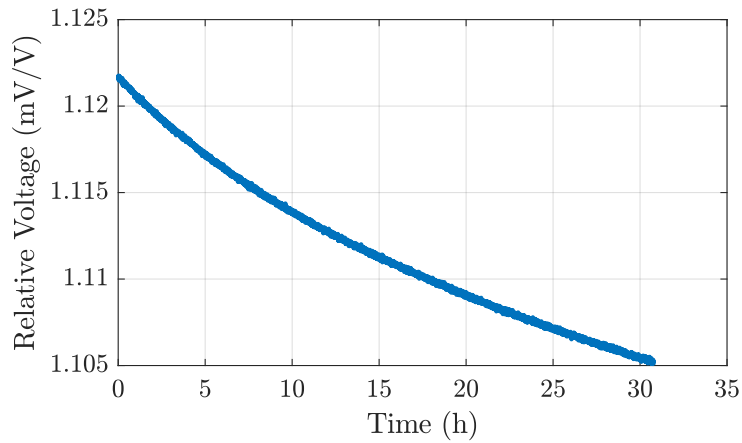


**Figure 4.21:** The load gauge response as a function of time (a) for 10 K intervals between 300 K and 250 K, fitted with linear curves. The drift speed clearly decreases as a function of temperature. The slope of the fits as a function of temperature (b).

Alternatively, the drift may be caused by the internal friction in the cell being too low. When pressure is applied, the only thing that keeps it constant is the internal pressure in the cell, mainly the friction between the screw and the thread. When the cell is cooled, it contracts. Some parts will contract more than others and this could increase the internal friction, which may in turn cause the drift to stop. I believe this is the most likely explanation. This could be tested by increasing the friction, for example by changing the screws. To quantify the drift, it was measured at 10 K intervals between 300 K and 250 K at an applied force of 16.8 kN. The resulting curves are plotted in figure 4.21a. They are all fitted with linear fits and the temperature dependence of the drift speed is plotted in figure 4.21b.

Over a longer period of time, the drift is not linear. This is consistent with the explanation that the internal friction in the cell is responsible for the drift. When the pressure drops,

less friction will be required to keep the pressure from dropping further and thus the drift is expected to slowly drop off. In figure 4.22, the drift is shown for a period of 30 hours at 300 K.

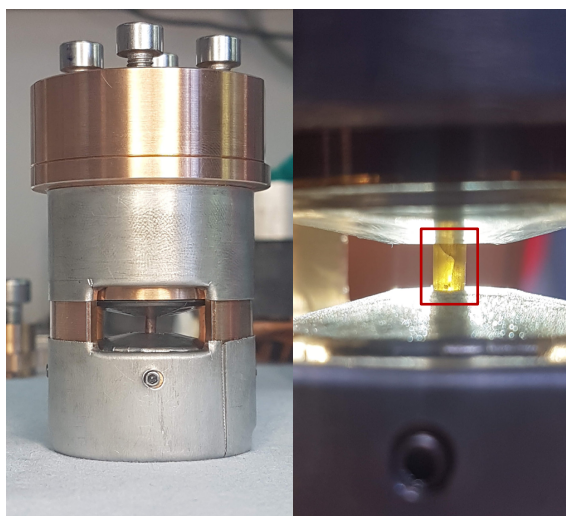


**Figure 4.22:** Load gauge response as a function of time, measured with an initial applied force of 8.9 kN at 300 K.

## Chapter 5

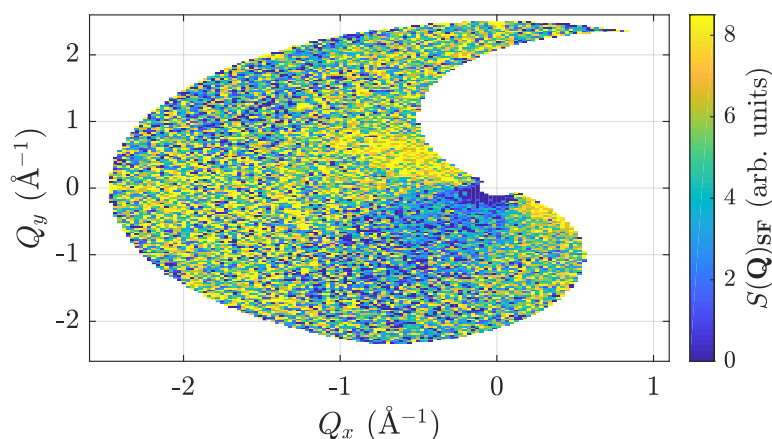
# Neutron Measurements on HTO with Cell v1

The experiment presented in this section was performed at D7, ILL in October 2018. It was performed by Pascale Deen, Ingrid Marie Bakke Fjellvåg and Richard Edberg. The data analysis was performed by me, in collaboration with Lise Sandberg.



**Figure 5.1:** Frontal view of the cell (left), covered in a sheet of cadmium to increase neutron absorption [28]. HTO sample (red square) in cell (right). After pressure has been applied, cracks start to appear.

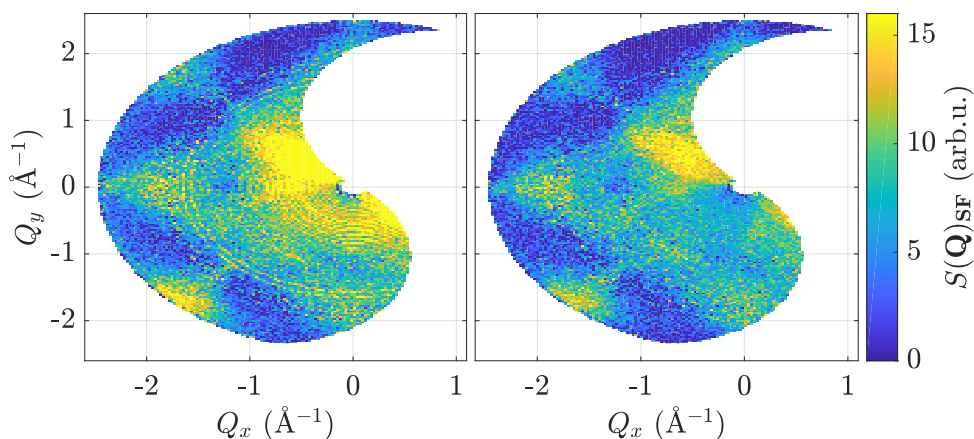
The incoming neutron wavelength was  $\lambda = 4.8 \text{ \AA}$ , and the sample was aligned so that scattering was measured in the  $(h, k, 0)$  plane. All measurements were performed in the first version of the cell, v1, the design of which is detailed in section 4.2. A cylindrical HTO sample ( $h = 3 \text{ mm}$ ,  $d = 2 \text{ mm}$ ) was measured in a  $180^\circ$  sample rotation range at ambient pressure and with 2 kN and 4 kN of applied force, corresponding to 0.6 GPa and 1.2 GPa uniaxial pressure, respectively.



**Figure 5.2:** Spin flip measurement of HTO taken at  $T = 50$  K, in the Paramagnetic phase and under 4 kN of applied force.

These pressures are the room temperature pressures, disregarding thermal contraction of the cell and sample during cooling. A picture of the sample in the pressure cell is shown in figure 5.1. The cell is covered in a sheet of Cadmium to increase neutron absorption.

One way to estimate the background from the pressure cell, is to look at the paramagnetic signal. As scattering from the HTO sample in this phase is expected to be completely rotationally symmetric (3.25), any rotation dependent feature, must be an artefact of the pressure cell.



**Figure 5.3:** Spin flip measurement of HTO at  $T = 1.5$  K, in the spin ice phase under an applied pressure of 2 kN (left) and 4 kN (right).

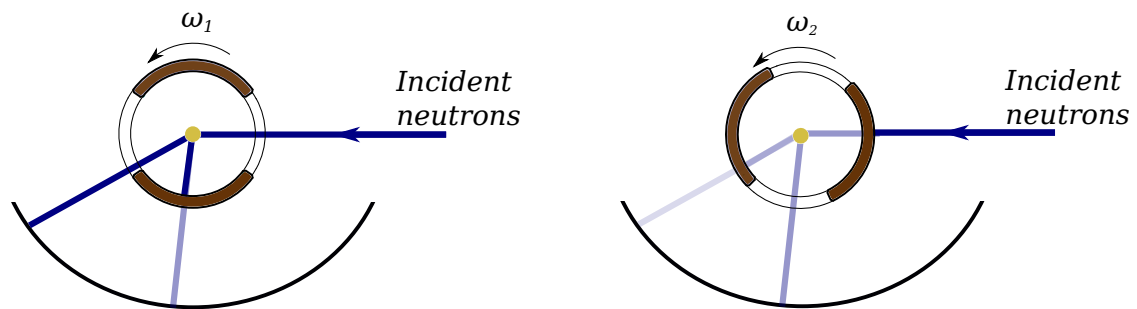
The data in figure 5.2 was taken at  $T = 50$  K, in the paramagnetic phase of HTO. The data is clearly not rotationally symmetric. The pressure cell produces substantial artefacts in the data. This is not at all surprising, since the idea behind this cell design was that

scattering would only be possible through the windows. It therefore makes sense that there are some areas of high intensity, when scattering is measured through the windows and some with lower intensity, when it is measured through the walls of the pressure cell.

These effects are also clearly present in the low temperature measurements, taken at  $T = 1.5$  K, presented in figure 5.3. This is problematic, since this makes it difficult to distinguish the changes caused by the pressure and ones caused by the cell background. The logical thing would be to normalize the low temperature data with the paramagnetic data, as this would then eliminate the attenuation caused by the cell as well as correct for the magnetic form factor. This, however, turns out not to be possible, the paramagnetic signal is too noisy and thus this corrections introduces a lot of unwanted noise in the data. Another avenue of correction has to be pursued.

## 5.1 The Simulation

We are confident that the regions of high and low intensity in the data are due to the windows in the cell. There appears to be three distinct levels of intensity in the paramagnetic signal. Presumably these correspond to the neutron beam being attenuated either once, twice or not at all depending on whether the incoming, outgoing, both or neither of the beams passes through a cell wall and is attenuated. If this is the case, it is possible to simulate the attenuation of the signal at every Q-point, given a scattering angle  $2\theta$  and cell and sample rotation  $\omega$ .



**Figure 5.4:** The geometry of the simple simulation of the attenuation by the cell. This is shown for two different cell and sample rotations  $\omega_1$  and  $\omega_2$ . The neutron beam scatters at the sample position, in the centre of the pressure cell and is measured at the detector covering  $2\theta = (5^\circ - 150^\circ)$ . For the left case, the incoming beam passes through a window, causing the signal to be attenuated either one time or not at all. For the right case, the incoming beam passes through a wall and thus the signal is attenuated once or twice.

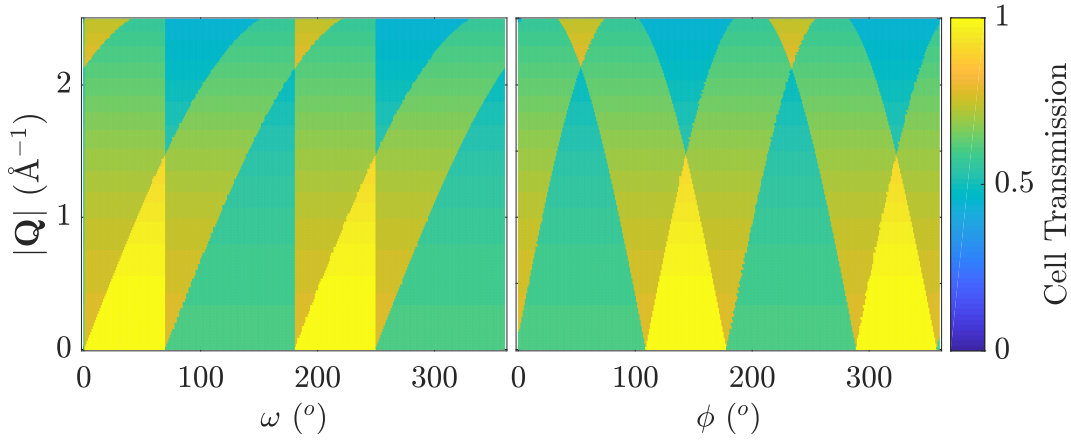
Such a simulation is created in Matlab. Iterating over the sample rotation  $\omega = (0^\circ - 360^\circ)$  and the scattering angle  $2\theta = (5^\circ - 150^\circ)$  the beam is attenuated zero, one or two times depending on how many times the beam passes through a cell wall. This process is shown

schematically in figure 5.4. The attenuated intensity ( $I_A$ ) is calculated as

$$I_A = I_0 \exp(-\mu d), \quad (5.1)$$

Where  $I_0$  is the non attenuated intensity, set to 1,  $d = 3$  mm is the thickness of the cell wall and  $\mu$  is the attenuation coefficient. This is calculated for copper beryllium using the online resource provided by NIST [52], yielding  $\mu = 0.086$  mm<sup>-1</sup>. As we also wish to correct the data for the magnetic form factor, this is calculated for Ho<sup>3+</sup> and multiplied with the simulation.

This yields the transmission of the cell as a function of  $|\mathbf{Q}|$  and sample rotation  $\omega$  as plotted to the left in figure 5.5. However, to transform to the experimental parameters  $Q_x$ ,  $Q_y$ , a transformation between  $\omega$  and the polar angle,  $\phi = \tan^{-1} \left( \frac{Q_y}{Q_x} \right)$  is needed.

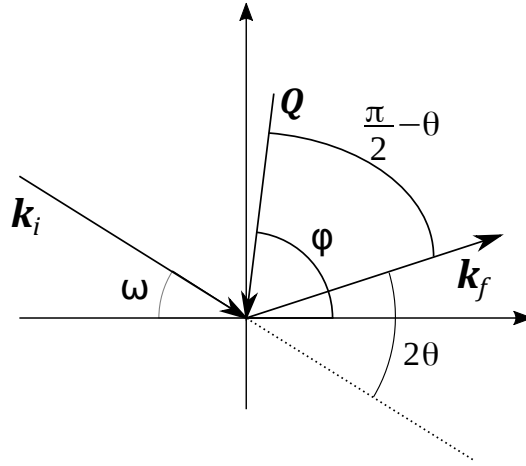


**Figure 5.5:** The simulation of the attenuation caused by the pressure cell as a function of  $|\mathbf{Q}|$  and sample rotation,  $\omega$  (left) and Polar Angle,  $\phi$  (right).

By geometric analysis it is possible to show that, assuming elastic scattering  $k_i = k_f$ , the polar angle can be calculated as

$$\phi = \frac{\pi}{2} - \theta + 2\theta - \omega = \frac{\pi}{2} + \theta - \omega. \quad (5.2)$$

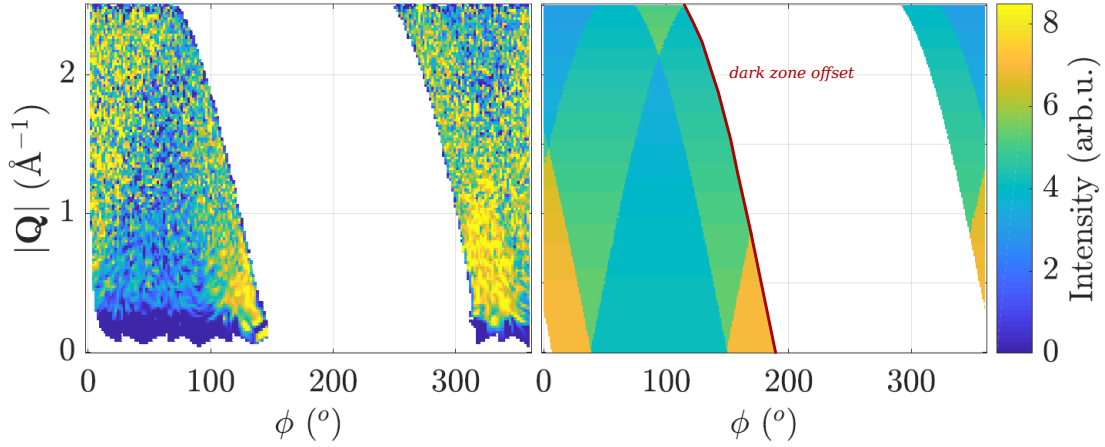
The geometry of the problem is shown in figure 5.6. Using this coordinate transformation we arrive at the right plot in figure 5.5.



**Figure 5.6:** The geometry of a scattering event. The polar angle  $\phi$  can be described in terms of the scattering angle  $2\theta$  and the sample rotation  $\omega$ .

### 5.1.1 Fitting

To ensure that the rotation offset of the simulation matches that of the experiment, a  $\phi$ -offset is added to the simulation. Furthermore, since the data only covers a  $180^\circ$  angle, a  $180^\circ$  *dark zone* is added to the simulation.

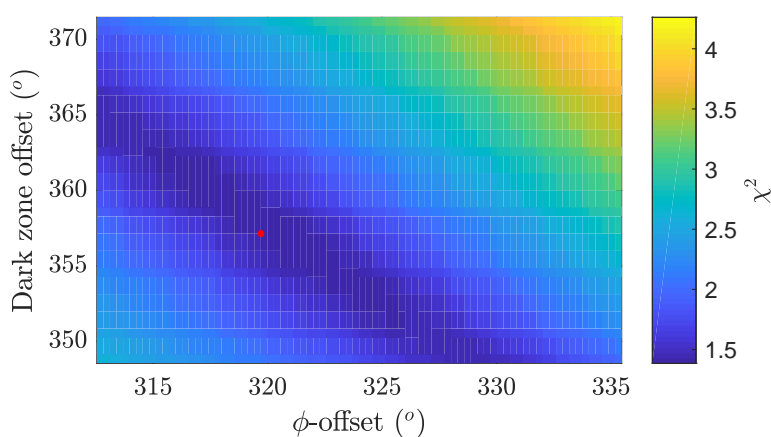


**Figure 5.7:** The paramagnetic signal (left) and the simulation (right) as a function of polar angle  $\phi$  and  $|\mathbf{Q}|$ . The edge of the *dark zone* (in red) and the offset in  $\phi$  are then varied to fit the simulation to the paramagnetic signal.

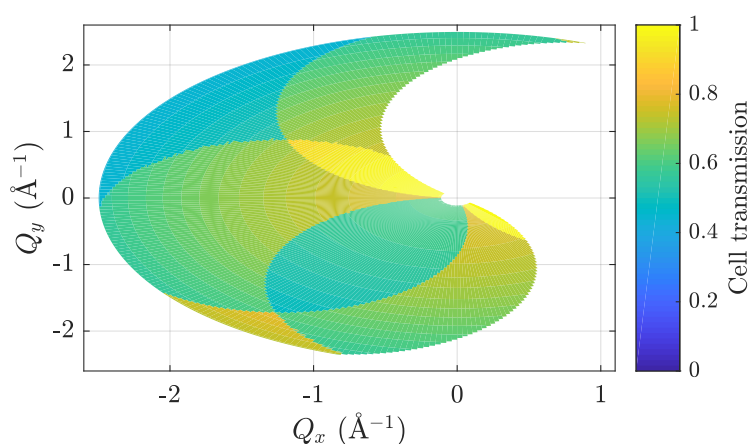
To make it possible to fit the simulation to the paramagnetic data, the data is interpolated onto the same grid as the simulation and the intensity of the simulation is normalized to the average intensity of the paramagnetic scan. The paramagnetic data and the simulation is plotted for comparison in figure 5.7. To estimate the goodness of fit, the  $\chi^2$  value is calculated

$$\chi^2 = \frac{(I_{sim} - S(\mathbf{Q})_{SF,param})^2}{\sigma_{SF,param}^2}. \quad (5.3)$$

It would of course be naive to believe that this simple simulation can accurately capture every feature of the paramagnetic signal. This fitting routine should however be able to find the parameters that ensure the best agreement with data. In figure 5.8, the  $\chi^2$ -value is plotted for a range of different values of the parameters. Choosing the parameters with the lowest  $\chi^2$ , normalising the maximum intensity of the simulation back to 1 and converting it to  $Q_x$ ,  $Q_y$ , yields the result shown in figure 5.9. When comparing this result with the paramagnetic data in figure 5.2, it is clear that the simulation has reproduced all main features in the signal. Whether the relative intensities are correct can only be tested by attempting to correct the paramagnetic signal.



**Figure 5.8:** The  $\chi^2$  plotted as a function of  $\phi$  offset and *dark zone* offset. The minimum  $\chi^2$  is marked with a red dot.



**Figure 5.9:** The finished simulation with  $\phi$  offset and *dark zone* fitted to the paramagnetic signal. Comparing this with figure 5.2, the same basic features have clearly been recreated.



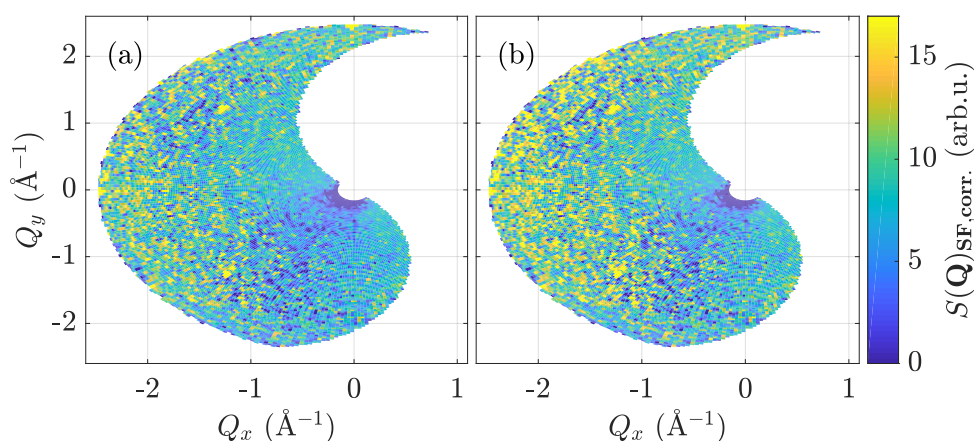
## 5.2 Correcting the Data

The paramagnetic and the low temperature data is interpolated onto the same grid as the simulation to enable the correction.

### 5.2.1 Paramagnetic data

To test the quality of the simulation, the paramagnetic signal is normalised to the simulation results and plotted in figure 5.10a. It is clear that the simulation has greatly reduced the artefact from the cell attenuation, it is however not perfect. For example there is a region of lower intensity around  $(-0.5, -1) \text{ \AA}^{-1}$ . It appears as though the attenuation by the cell might be more significant than what was calculated.

As the paramagnetic data was taken with an applied force of 4 kN, some level of discrepancy could be expected.

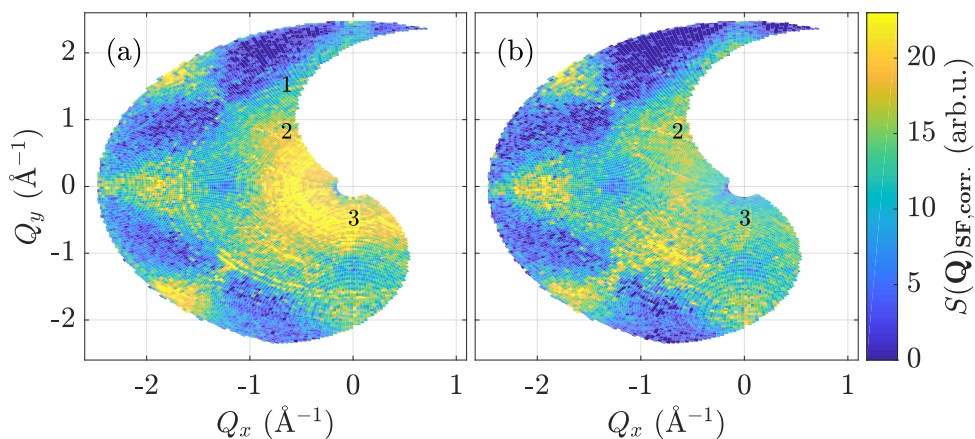


**Figure 5.10:** The paramagnetic signal normalised to the final simulation results, with ambient wall thickness (a) and fitted wall thickness of 3.2 mm (b). Clear features of the cell attenuation in the data still remain.

When the cell is pressurised the cell walls will expand perpendicular to the pressure, according to the Poisson effect (4.2), resulting in an increased attenuation. The thickness of the cell walls is implemented as a fitting parameter in the fitting routine described above, yielding a value of  $d_{fit} = 3.2 \text{ mm}$  compared to the value at ambient pressure of  $d = 3 \text{ mm}$ . The paramagnetic data is corrected using  $d_{fit}$ , the resulting data is plotted in figure 5.10b. This result is very hard to distinguish from the correction using the ambient value of the wall thickness.

## 5.2.2 Low Temperature Spin Flip Data

Correcting the pressurised, low temperature data is then trivial, as both of these data sets were taken at the same  $\omega$  value as the paramagnetic scan. The resulting data can be seen in figure 5.11.

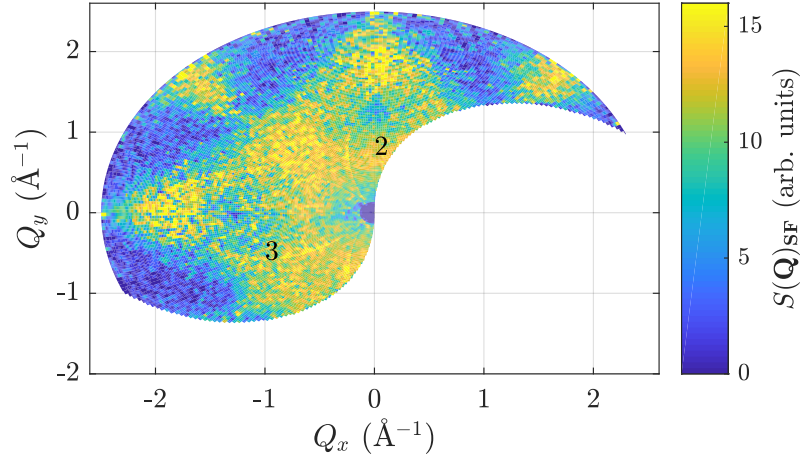


**Figure 5.11:** Spin flip measurement of HTO at 1.5 K under 2 kN (a) and 4 kN (b). The data has been corrected by the simulation of the cell attenuation.

Here, the 2 kN data (figure 5.11a) has been corrected with the attenuation resulting from the ambient value for the wall thickness  $d$ . This is of course not entirely physical as we would expect the actual value to be somewhere between 3 mm and 3.2 mm. While the correction has definitely managed to reduce the artefacts from the cell, there are still some quite significant cell features in the data. Most significantly, around the edges of the cell features (2, 3 in figure 5.11a), sharp edges are still present, indicating that the correction is not completely accurate. There is also a ring (1) of slightly increased scattering at constant  $Q$ .

The 4 kN data (figure 5.11b) is corrected using the fitted wall thickness  $d_{fit}$ , as the paramagnetic was also taken at 4 kN. The same remnants of the cell artefacts are still present (2, 3).

The Ambient pressure measurement was taken at a different rotation offset and thus it is necessary to fit the  $\phi$  offset once again. The ambient pressure data is then corrected using  $d = 3$  mm, the result of this correction can be seen in figure 5.12. Where the same cell artefacts are also present (2, 3).



**Figure 5.12:** Spin flip data measurement of HTO at ambient pressure and 1.5 K. It has been corrected by the simulation discussed above, using the attenuation coefficient obtained by fitting to the paramagnetic data

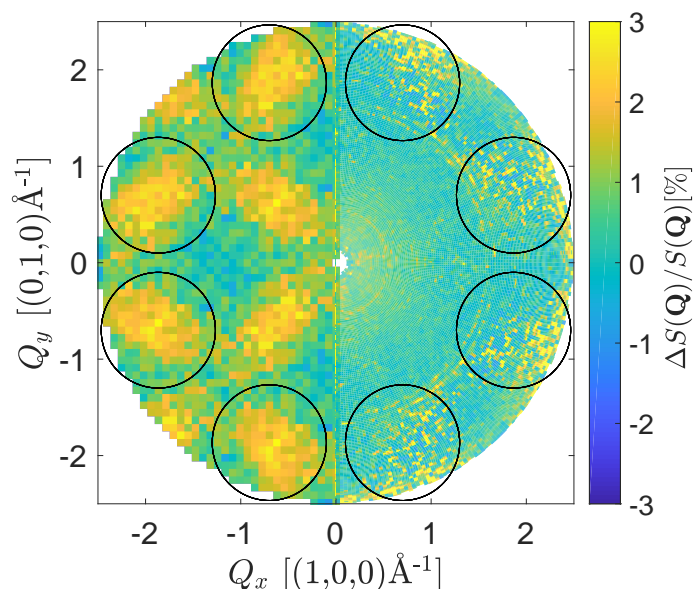
As the increase in wall thickness is directly related to the pressure applied, the pressure can be estimated. This estimate relies on the room temperature values of the elasticity and Poisson ratio of CuBe, as the low temperature values are unknown. The Poisson ratio of CuBe is  $R_P = 0.3$  and the Young's modulus is  $E_Y = 122$  GPa [40]. The corresponding applied pressure can then be calculated as

$$P = E_Y \epsilon_l = \frac{E_Y (d_{fit} - d)}{d R_P} = 27 \text{ GPa}. \quad (5.4)$$

This is obviously not physical as multiple cell components, as well as the sample will fail long before this pressure is reached. In later experiments, we saw indentation of the steel anvils with as little pressure applied as 0.7 GPa. This does however tell us that there are aspects of the cell background that we do not yet understand. The applied forces of 2 kN and 4 kN should be taken with a grain of salt. It is certain that some amount of pressure was applied, but exactly how much is quite uncertain.

### 5.3 Comparing with Theory

Given the uncertainty related to how much pressure was applied during each of the measurements, as well as our lacking understanding of the cell background, it is not possible to ascribe much certainty to a quantitative comparison between the data and theory. It is however interesting to make a qualitative comparison between the corrected data and theory.



**Figure 5.13:** Relative change in the spin flip scattering between ambient pressure and 4 kN, comparison between theory (left) and data (right). The high  $Q$  region shows slight agreement between theory and data (circled). Figure from [25]

In figure 5.13 the relative change between ambient and 4 kN data is plotted along with the change in the theoretical cross section at ambient pressure and 1.5 GPa. This figure was made by Richard Edberg and published in [25]. The data has been symmetrized to increase the overlap between the two data sets. The low- $Q$  region is completely featureless. It seems that any information there may have been in the low- $Q$  region have been destroyed by the pressure cell. In the high- $Q$  region, there are areas of increased intensity in the regions that theory predict. This is promising and indicate that with a cleaner cell background we may have seen a more substantial agreement with theory.

The problems with the background corrections and the need for more accurate pressure determination led to the new cell design, discussed in section 4.3. Neutron measurements were also performed with this cell, they are discussed in the next chapter.

## Chapter 6

# Neutron Measurements on HTO with Cell v2

A second set of neutron measurements were performed at D7, ILL in October 2019, this time using the second version of the cell design (section 4.3). The experiment was performed by Pascale Deen, Denis Vasiukov and myself. The aim was to characterize the background of the new pressure cell design, as well as to try to quantify the change in the spin flip scattering.

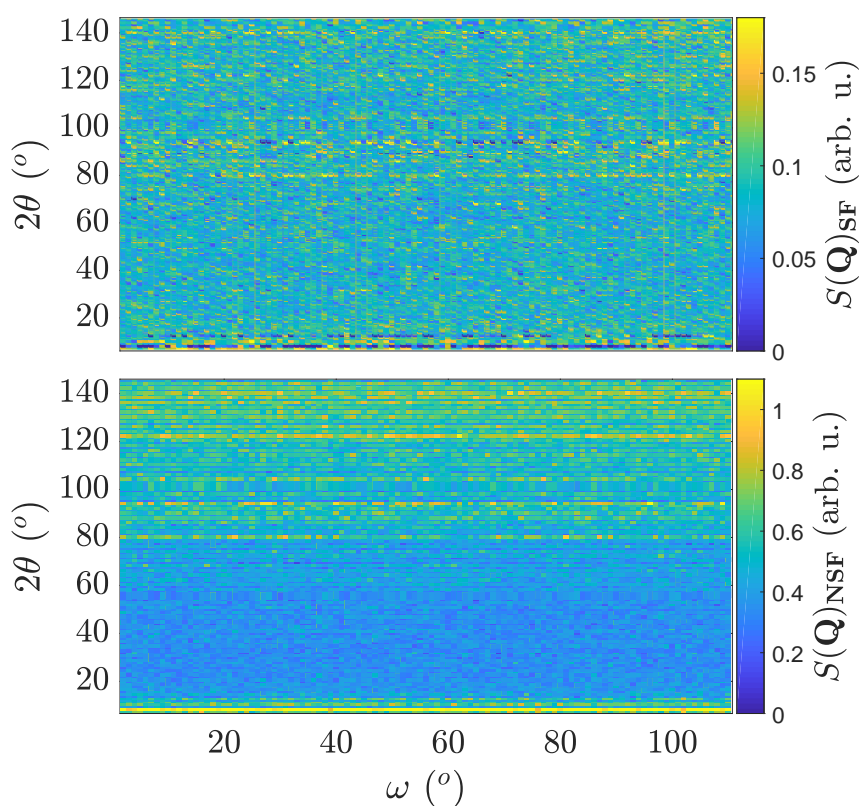
As in the previous experiment, the outside of the cell was covered in cadmium (figure 6.1), everywhere except for at the sample position.



**Figure 6.1:** Image of the pressure cell v2. The cell has been covered in a sheet of cadmium, everywhere but at the sample position.

## 6.1 Measuring the Cell Background

Initially a background measurement was performed at 300 K with an aluminium nut at the sample position. Aluminium has a very low incoherent scattering cross section and thus the resulting signal will be almost exclusively scattering from the cell and aluminium powder lines. With a wavelength of  $\lambda = 4.8 \text{ \AA}$ , these should be at  $2\theta = 84^\circ$ ,  $110^\circ$ , and  $144^\circ$ . Both the spin flip and non-spin flip part of the background is plotted as a function of scattering angle ( $2\theta$ ) and sample rotation ( $\omega$ ) in figure 6.2.



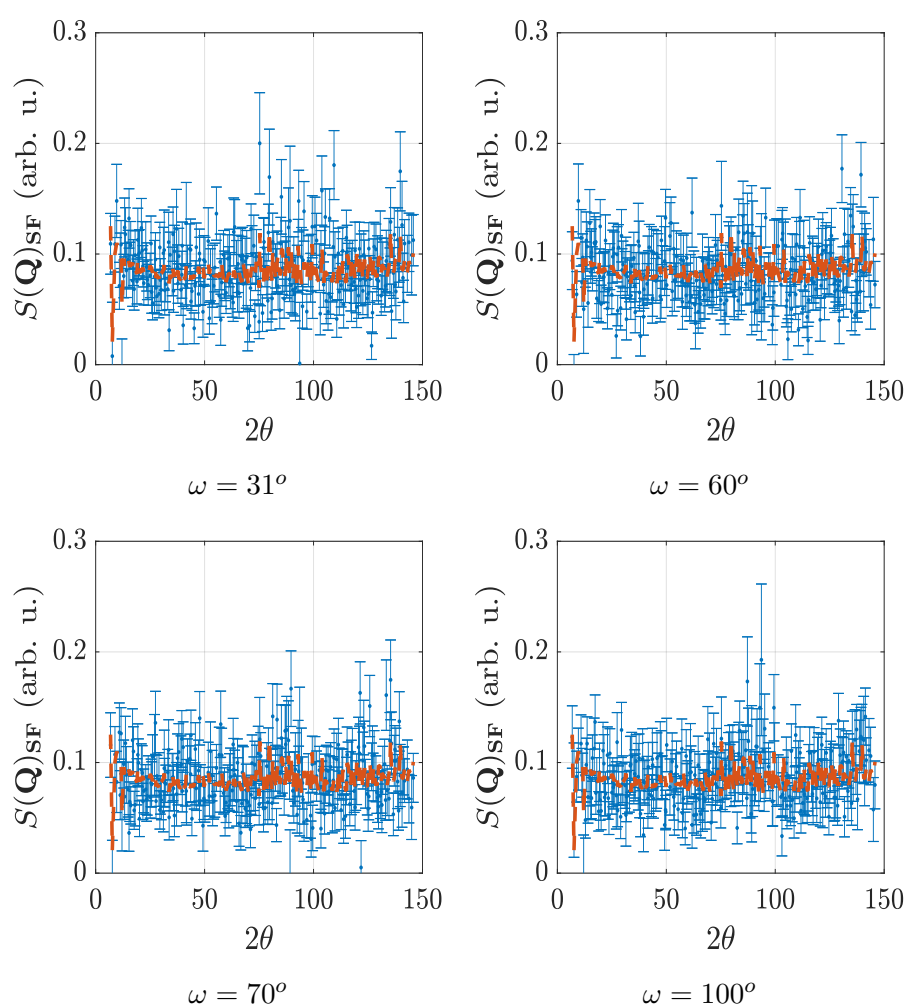
**Figure 6.2:** Background measurement of the cell at 300 K, taken at D7 with  $\lambda = 4.8 \text{ \AA}$ . An aluminium nut was placed at the sample position to separate the anvils. Both the spin flip (top) and non spin flip (bottom) signal are presented.

Examining the background signal, it looks to be largely independent of sample rotation. Especially the non spin flip signal appears to be almost entirely  $\omega$ - independent. The case is less clear when looking at the spin flip scattering. Although there is no indication of any large  $\omega$ -dependent features, the relatively low statistics makes it impossible to rule out completely. However, the cell is entirely rotation symmetric, except for the two small "view ports", so it seems likely that the SF background should also be rotation symmetric.

## 6.1. Measuring the Cell Background

To substantiate this claim the  $\omega$ -average is performed, this is then compared to several  $2\theta$  cuts, six of which are shown in figure 6.3. There is no evidence that any of the cuts disagree with the average in any significant way, therefore we choose to use the average as the background.

It would of course be more ideal to also have done these measurements at low temperature, as the measurements we are trying to correct are done at  $T = 1.5$  K. However due to time constraints this was not possible. This may seem problematic, but as the cell is constructed to be almost entirely non-magnetic, the SF scattering from the cell should not be too temperature dependent.



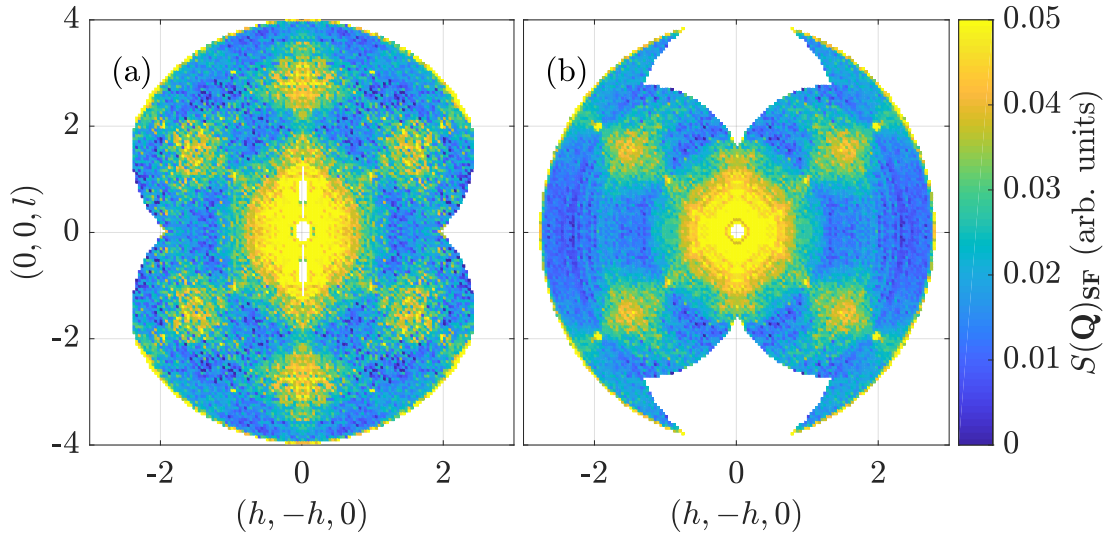
**Figure 6.3:** Four  $\omega$  cuts (blue) in the SF background plotted along with the intensity averaged across  $\omega$  (orange) as a function of  $2\theta$ . Some of the cuts have slight deviations from the average, but these deviations are not statistically significant.

## 6.2 Low Temperature Spin Flip Data

A measurement of a HTO cylinder ( $h = 3 \text{ mm}$ ,  $r = 3 \text{ mm}$ ) in the cell was performed at  $T = 1.5 \text{ K}$  and ambient pressure. The sample was aligned so that scattering was measured in the  $(h, -h, l)$ -plane. Only z-polarization was measured, as the z spin flip cross section can be calculated directly from the theoretical simulations (section 2.3.2), there is no immediate need to separate the total magnetic cross section. In the future a full measurement of all polarization directions could be performed to extract the total magnetic scattering cross section of the background. The spin flip scan is presented in figure 6.4a.

The sample was then extracted in order to apply pressure with a hydraulic press. The first attempt failed because the pressure was applied too fast causing the first sample to break and the steel anvils to indent at  $F < 5 \text{ kN}$ . A second identical sample was used and pressure was increased to  $F \sim 2.5 \text{ kN}$ , which corresponds to approximately  $P = 0.35 \text{ GPa}$ , at which point clear cracks were observed in the crystal. This should however not be a problem as the pressure will keep the sample fixed. To verify that there was no misalignment and that the sample didn't break, a structural Bragg peak was scanned as a function of temperature and showed no change.

The cell and sample were then cooled back down to  $T = 1.5 \text{ K}$  and a measurement was performed, the data can be seen in figure 6.4b.



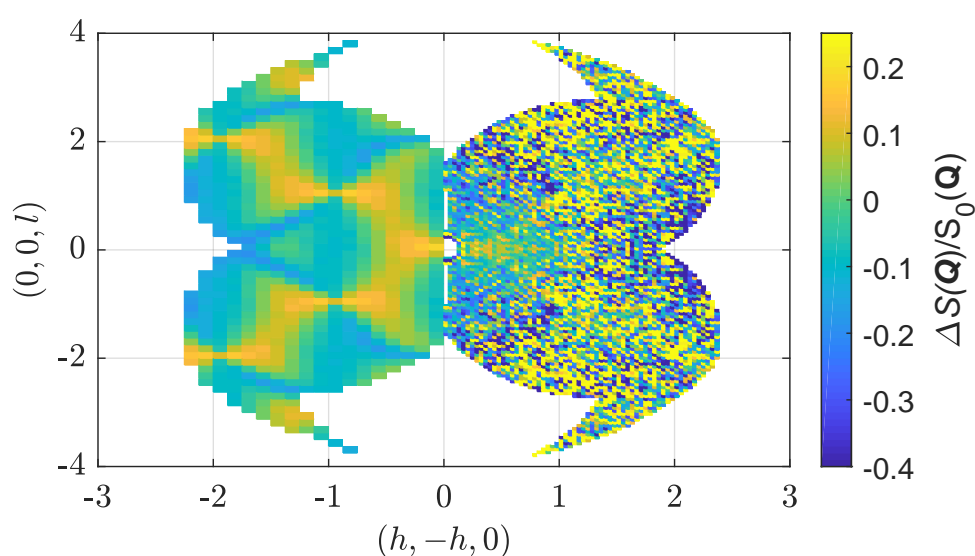
**Figure 6.4:** Spin flip measurement of HTO at ambient pressure (a) and  $P = 0.35 \text{ GPa}$  (b) applied in the  $(110)$  direction, perpendicular to the scattering plane. The data has been symmetrised to maximize overlap between the two data sets. Published in [29].

Due to a misidentification of a structural Bragg peak during the experiment, the two



measurement were not performed over the same  $\omega$ -range and they do not have the amount of overlap that we would have liked. Therefore the datasets were symmetrized. The  $(h, -h, l)$  plane has two mirror planes, the x- and y-axis, the data has been mirrored in both.

Comparing the two data sets, it seems as though the background in the data taken under pressure is slightly lower, furthermore it looks as though the broad features in figure 6.4b. e.g. at  $(h, k, l) = (1.7, -1.7, 1.7)$  are slightly more well defined. At first glance it may also appear that the pinch points have become slightly more intense. To investigate this further, the relative change in scattering intensity is plotted in figure 6.5 along with theory.

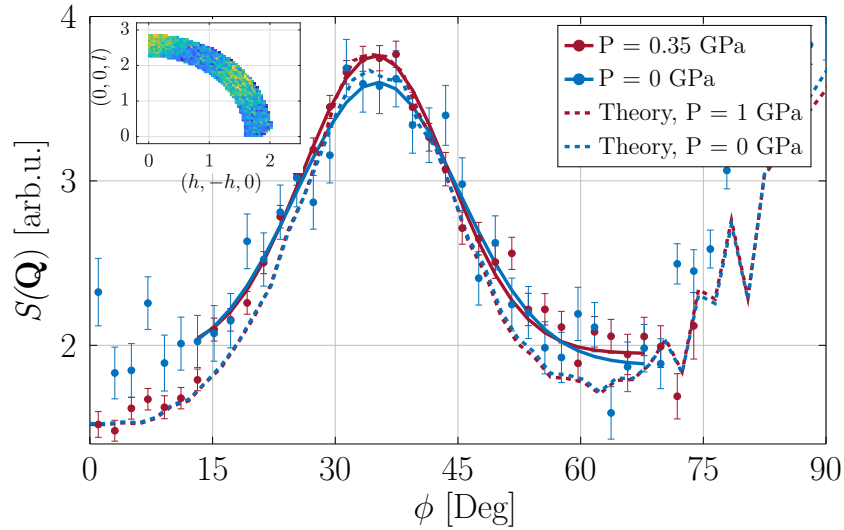


**Figure 6.5:** Relative change in the spin slip scattering of HTO under uniaxial pressure, MC simulation at  $P = 1$  GPa (left) and data (right). The theoretical map has been cropped to ease comparison with data. Simulations have been performed by Richard Edberg.

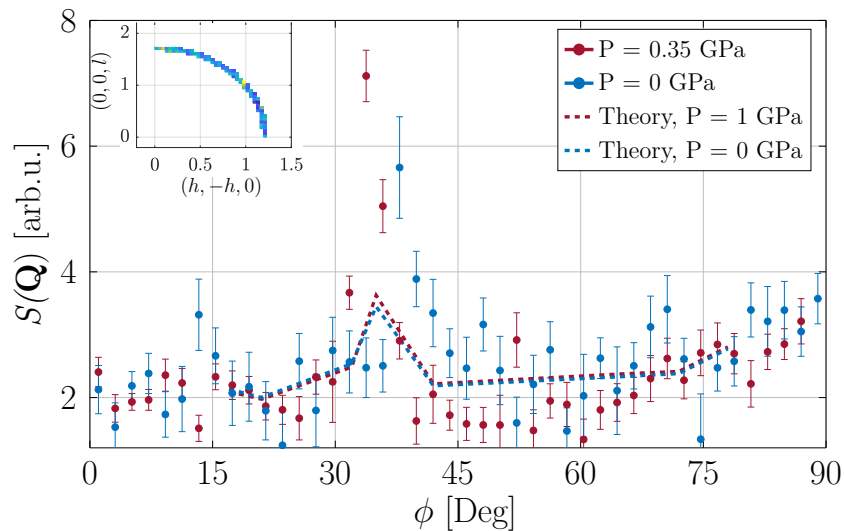
There seems to be some agreement between theory and data. Especially the lines of decreased scattering seems to be at least qualitatively consistent between theory and data. Furthermore, close to  $(0, 0, 0)$ , the two data sets have a similar horizontal features along  $(h, -h, 0)$ . The experiment does not however, convincingly recreate the lines of increased intensity going from the origin to  $(-2, 2, 2)$  in a zig-zag pattern.

Quantifying the changes that are observed requires some additional examination. Several cuts are made to try and estimate the precise change, first an angular cut is made across the broad feature at  $(1.7, -1.7, 1.7)$  as shown in figure 6.6. The change seems very small and indeed, it turns out to be insignificant. Fitting the peaks with a Gaussian and comparing the peak amplitude of the fits yields a change of  $4\% \pm 4\%$ . This is obviously not significant.

As the pinch point is indicative of the long range interactions of the magnetic monopoles, it is interesting to see whether this interaction increases as a function of pressure. A cut is made across a pinch point and plotted, along with theory, in figure 6.7. It does look as though the intensity of the pinch point increases as a function of pressure. This increase is not captured by theory. As a limited number of spins can be simulated, it is reasonable that theory has trouble capturing these long range features in detail.



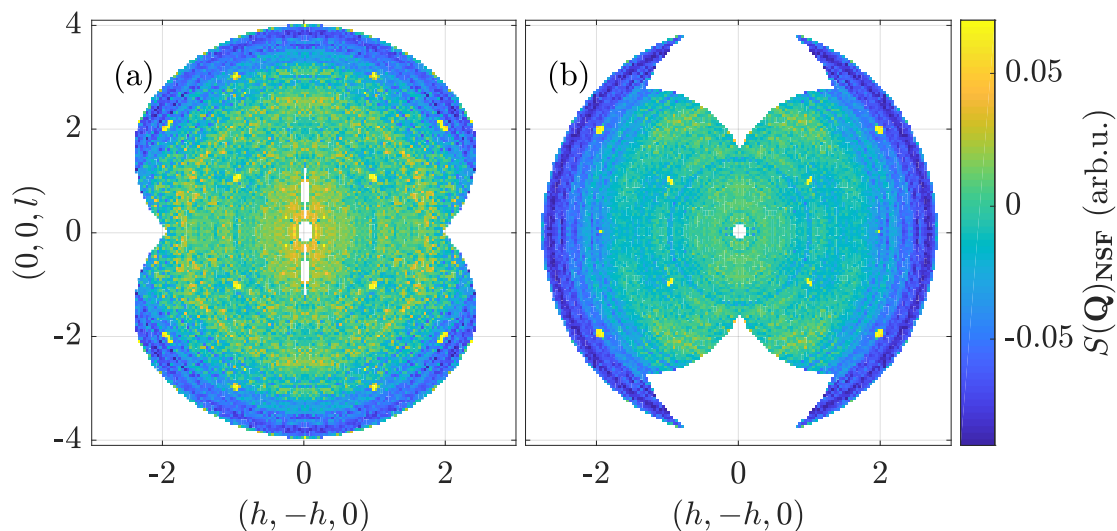
**Figure 6.6:** Angular cut of data (points), between  $|\mathbf{Q}| = 1.38 \text{ \AA}$  and  $|\mathbf{Q}| = 1.78 \text{ \AA}$ , from D7 experiment with fitted Gaussians (solid) compared to theory (dashed). The data is cut across a pinch point. The theoretical lines have been rescaled and a background parameter has been added for it to be comparable to data. The cut through reciprocal space is shown in the inset. Published in [29].



**Figure 6.7:** Angular cut of data (points) across pinch point, compared to theory (dashed). The theoretical lines have been rescaled to be comparable to the experimental data. The cut through reciprocal space is shown in the inset.

## 6.3 Low Temperature Non Spin Flip Data

As stated earlier (3.36e), a significant fraction of the non spin flip signal is magnetic. As the spin flip signal gave some rather inconclusive results, it could be interesting to try and examine the magnetic part of the non spin flip signal. The measurements are shown in figure 6.8.



**Figure 6.8:** Non-spin flip measurement of HTO at ambient pressure (a) and  $P = 0.35$  GPa (b) applied in the (110) direction, perpendicular to the scattering plane. The data has been symmetrised to maximize overlap between the two data sets.

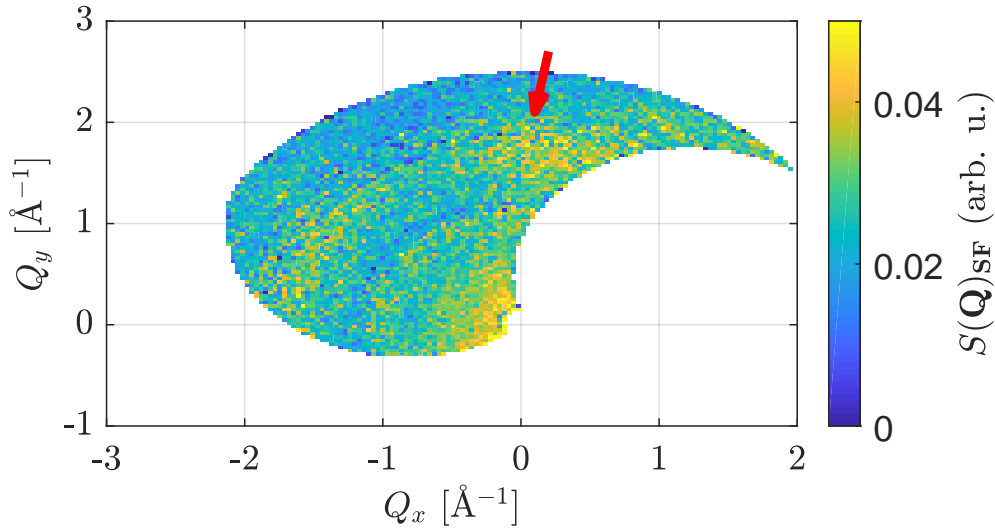
It is immediately clear that there are some issues with the background subtraction as both data sets have large regions of negative intensity. This is not surprising as the background measurement was done at 300 K and it is expected that scattering from lattice vibrations in the cell will decrease at lower temperature.

The background in the data taken under pressure is significantly more negative. This is an indication that the background, at least the NSF part, is pressure dependent. As the cell is compressed by the pressure, the cell walls will thicken slightly due to the Poisson effect and the beam will be attenuated more, just as discussed in the previous chapter.

Attempts were made to correct the background, by fitting the  $|\mathbf{Q}|$  - dependence of the background with a high order polynomial and then dividing the data by the fit. This did not however result in anything useful as any diffuse magnetic feature were distorted or destroyed by the process.

## 6.4 Paramagnetic Data

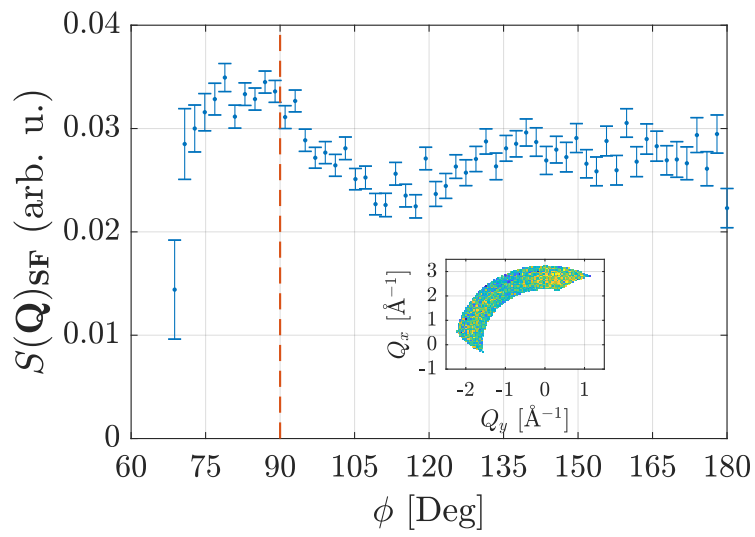
A paramagnetic scan was done at 50 K and ambient pressure, it is presented in figure 6.9. The SF background has been subtracted, in the same way as the data in figure 6.4. As The paramagnetic phase have uncorrelated spins, the corresponding spin flip scattering should be entirely flat, except for the magnetic form factor which is only  $|\mathbf{Q}|$  dependent (3.22).



**Figure 6.9:** HTO at 50 K, in the paramagnetic phase. The spin flip background (figure 6.2) has been subtracted. Given a perfect background subtraction, this signal should have been complete rotation symmetric. This is however not the case as there is a strong  $\omega$ -dependent feature (red arrow).

At first glance it looks like the scan has very weak spin ice features (marked by a red arrow). When doing a line cut (figure 6.10) it is clear that this is not the case, as the peak does not obey the crystal symmetries. The origin of this feature, is unclear. There is no apparent reason that the background has rotation dependent features. The cell wall is completely rotation symmetric, except for the two viewports (figure 4.3).

A future experiment to map the pressure and temperature dependence of the background is essential to understand the limitations of the current cell design as well as to determine the best possible background subtraction for future experiments.



**Figure 6.10:** Line cut of spin-flip measurement of HTO at 50 K, in the paramagnetic phase. The dashed red line indicates the mirror plane of the  $(h, -h, l)$  - plane

# Chapter 7

## Discussion and Outlook

### 7.1 Uniaxial Pressure Cell

The pressure cell design presented in this report is at a place where I am convinced that it is possible to consistently perform neutron experiments under a constant and accurately determined (to within 10 %) pressure, up to 3 GPa. There are however still several more challenges that needs to be resolved before I would deem the design finished.

First, even with the load gauge ensuring in situ monitoring of the pressure on the sample during an experiment, there is no way to ensure that the sample actually stays pressurised. If the sample has a much larger thermal contraction than the pressure cell around it, the pressure may drop a lot. While this would of course be measured by the load gauge, it would still mean that it would not be possible to measure at the desired pressure. Of course the opposite may also prove an issue as the thermal contraction of the sample may cause it to crush itself if it is too small compared to the pressure cell. These effects could potentially limit the choice of sample quite dramatically.

One way to alleviate this is to create a cell design that makes it possible to change the pressure in situ. Such pressure cells already exist for other techniques, such as susceptibility measurements and X-ray scattering. One designed by C. Hicks et al [53] is based on piezoelectric components. The pressure is changed by utilizing the fact that the piezoelectric elements contract or expand when a voltage is applied. This means that they are only able to apply relatively small forces, which in turn means that they require very small samples to achieve significant pressures. For this reason, these designs do not work for application in neutron scattering experiments. Especially in the case of magnetic, diffuse scattering.

Another solution would be a design that employs a pressurised membrane to apply the pressure. Such a design already exists and could fairly easily be modified to fit this cell.

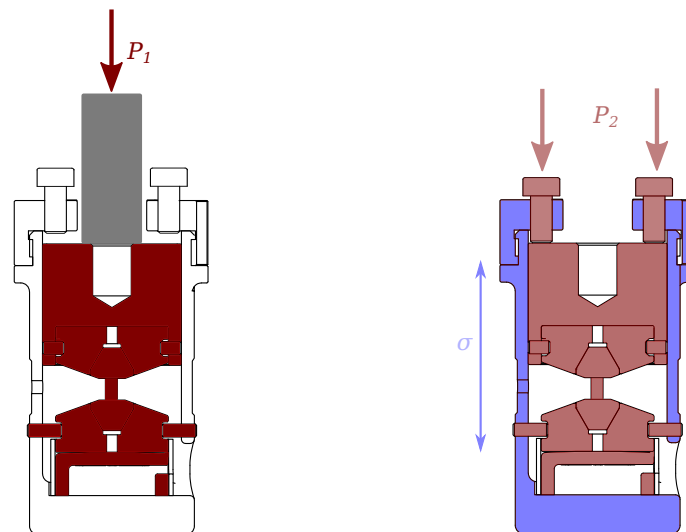
## 7.1. Uniaxial Pressure Cell

The membrane would then be connected to a supply of pressurised Helium at room temperature. Which would be used to change the pressure without having to extract the cell. This design would, however, require extensive modifications to the set-up at the neutron beamline.

The most significant problem that I have not discussed in the previous chapters is the fact that it is extremely difficult to apply a precise pressure. The issue is depicted in figure 7.1. When pressure is applied with a hydraulic press, the piston, anvils, sample and load gauge are compressed.

The idea then is that when the screws are tightened and the press is released, the screws will keep the pressure constant. However, when the screws are tightened and the press is released, the body of the cell experience a strain in the opposite direction, causing the body to stretch. This relaxation will in turn reduce the pressure inside the cell.

This effect turns out to be quite significant, reducing an applied force of 20 kN to around 15 kN. The precise amount varies with exactly how much the screws are tightened and how much force is applied. This means that it is difficult to achieve pressures that are close to the yield point of either the cell or the sample.



**Figure 7.1:** Pressure applied to the pressure cell, with a hydraulic press (left) and after the screws are tightened and the press released (right). Parts that are under compressive stress are marked in red, parts that are being stretched are blue. When the press is released, the cell body is stretched, leading to a drop in the internal pressure ( $P_1 > P_2$ ).

It is possible to get around this issue by not using a press to apply the pressure. Instead, pressure can be applied by simply tightening the screws. This approach makes it very difficult to ensure an even distribution of pressure from each of the four screws, increasing

the risk of breaking the sample and so this is not a viable solution.

It may be possible to mitigate the problem by using a more rigid material for the cell body, but I would not recommend this course of action. To resolve this issue I would rather recommend a manner of applying pressure where the entire cell is strained from the beginning. This could for example be a design that utilize one central screw in the lid to apply the pressure.

### 7.1.1 The Load Gauge

The load gauge is in a functional state. The room temperature pressure curves are reproducible and it holds up well under repeated loading and thermal cycling. Ideally, I would have measured additional pressure curves in the LN<sub>2</sub> set-up at 77 K to test the reproducibility of these curves. At the moment the gauge has to be centred very precisely to ensure an accurate pressure measurement. This is difficult and results in a systematic error. To combat this, I would suggest making two improvements.

First, changing the strain gauges for bigger ones would likely alleviate the problem. The strain gauges that are used in the current design are quite small, this makes them very sensitive to local strain fluctuations. Larger strain gauges would measure the average strain over a larger area and thus a small misalignment of the gauge would play a smaller role.

Second, constructing a ring to surround the load gauge would align it more accurately, and would make it easier to reproduce the gauge placement between measurements.

Given a lot more time and resources, it would also be ideal to obtain pressure curves at lower temperatures. As previously stated, this is currently not possible in the Copenhagen region. There is a set-up available at the SNS, in Tennessee. This set-up utilizes a pressurised membrane to change the pressure in situ. At the moment, however, I do not believe that this is necessary. The low temperature behaviour of the gauge is understood well enough to accurately estimate the pressure.

## 7.2 Ho<sub>2</sub>Ti<sub>2</sub>O<sub>7</sub> Under Pressure

The neutron data presented in this thesis is rather inconclusive. While we did observe changes to the scattering signal that are consistent with theory, the change in peak intensity of  $4 \pm 4$  % is not significant. The fact that the pinch point scattering seems to increase with pressure is however, more promising. It could be, at least intuitively, interpreted as an increased interaction between the magnetic monopoles. Further modelling and experiments with a more well determined pressure is however needed before any concrete

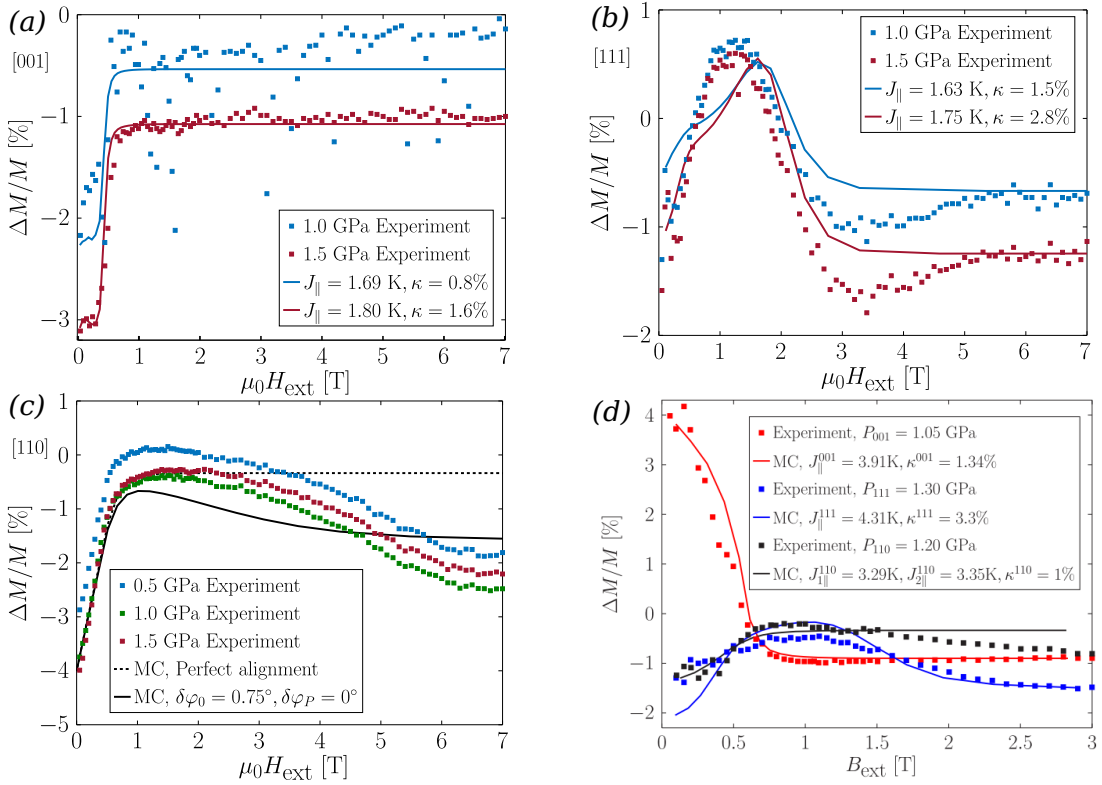


conclusions can be drawn. These things taken together does nonetheless indicate that uniaxial pressure has measurable effects on the magnetic interactions in HTO. This is further corroborated by magnetisation measurements.

### 7.2.1 Magnetisation Measurements

Magnetisation measurements on HTO under uniaxial pressure were performed in Japan by Ingid Marie Bakke Fjellvåg, Patrik Henelius and Pascale Deen. This was done with the assistance of M. Mito and his group, using their experimental set-up [29].

The relative difference in magnetization is plotted in figure 7.2(a-c) along with theory. The three different plots correspond to pressure applied along the three different directions (001), (111), (110). The original magnetisation measurements on DTO, discussed in section 2.3.2 are plotted in figure 7.2d for comparison.



**Figure 7.2:** Magnetization measurements of HTO (a-c) from [25] and DTO (d) from [29]. The relative change in magnetization between ambient pressure and the pressure noted in the legend is plotted as a function of temperature, along with theory.

Theory provides excellent fits for pressure along (001) and (111). There is however quite a large discrepancy between data and theory in the case of pressure along the (110) direction (figure 7.2c (lower line)). The magnetization is expected to saturate at some sufficiently high field. This does not appear to happen in the (110) case. This discrepancy is believed

to be due to a misalignment when pressure was applied [29]. This misalignment is taken into account in the fitting, producing a better result (figure 7.2c (upper line)). In the case of DTO, it was concluded that uniaxial pressure broke the degeneracy between the two different dipolar chain states ( $M_{\perp}$ ,  $M_{\parallel}$ ) and at high pressure (3.4 GPa) would induce a ferromagnetic ground state [25]. The same thing appears to be the case for HTO, with pressure along (001) and (111). Here HTO is expected to transition into the ferromagnetic ground state at 3.3 GPa and 4 GPa respectively. With pressure along (110), it turns out that the degeneracy is upheld. The change in the nearest neighbour interaction is cancelled by the change in the dipolar interaction.

This may explain the very insubstantial change observed in the second neutron experiment, where pressure was applied along the (110) axis.

This allows us to conclude that measurements should ideally be performed with pressure applied along (001) as this is where the change will be most significant and the transition to the ferromagnetic state will occur at the lowest pressure (3.3 GPa).

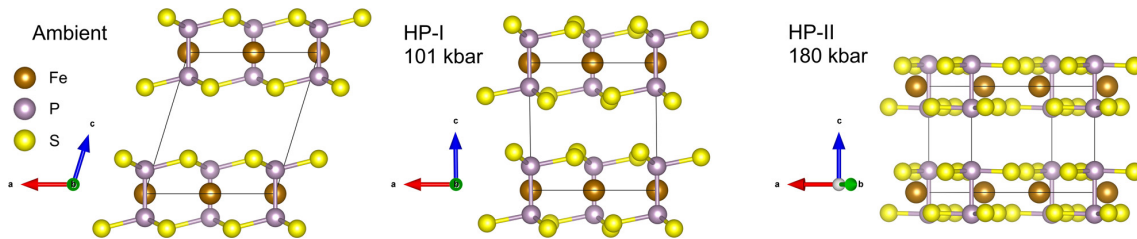
The issue now becomes whether or not the sample will actually be able to withstand these high pressures. During the second neutron experiment the sample broke and the steel anvils indented below 0.7 GPa. This leads me to conclude that the pressures reached during the first experiment can not have been as high as previously noted (0.6 GPa and 1.2 GPa). With the new WC - anvils it may be possible to go to higher pressures as they won't indent, but the sample has not become any stronger and will likely break at pressures much lower than 3.3 GPa.

During the magnetization measurements, the sample was supported by epoxy, making it possible to go to 1.5 GPa, this is much higher than what was reached during the neutron measurements, but still well below the goal of 3.3 GPa. Furthermore, epoxy is unproblematic in a magnetization experiment, but with its high hydrogen content it would create a massive neutron background. One possible solution could be to use deuterated epoxy.

## 7.3 Future Projects

The spin ice study is by no means finished. It is however, still a useful exercise to consider possible future projects with the pressure cell. I will attempt to outline one suggestion as to where the application of uniaxial pressure may prove interesting.

Recently Coak et al. published a hydrostatic pressure study on  $\text{FePS}_3$  [54]. They showed that by applying hydrostatic pressure on a powder sample they were able to induce two structural phase transitions, depicted in figure 7.3.  $\text{FePS}_3$  is a largely 2D material, with a very weak out of plane coupling along the c-axis, only bound by weak van-der-Walls forces.



**Figure 7.3:** Structural phase transitions of  $\text{FePS}_3$  under uniaxial pressure. Under ambient pressure (left), the ions are strongly bound in the a-b plane and only bound with van-der-Walls forces out of plane. Under 101 kbar (middle), corresponding to 10.1 GPa, the sample undergoes a *shear*-transition, displacing the layers with respect to each other. Under 180 kbar (right), corresponding to 18 GPa, the c-axis collapses. Figure from [54].

The Fe ions couple antiferromagnetically within the plane and have a weak out of plane antiferromagnetic coupling. Hydrostatic pressure is applied to the powder sample and the strong intra-planar binding ensures that it mainly affects the c-axis, making it pseudo-uniaxial.

At 101 kbar, corresponding to 10.1 GPa a transition occurs that is a *shear* of the plane, changing the orientation of the c-axis. At 180 kbar, corresponding to 18 GPa, a second transition occurs. This transition is a collapse of the c-axis.

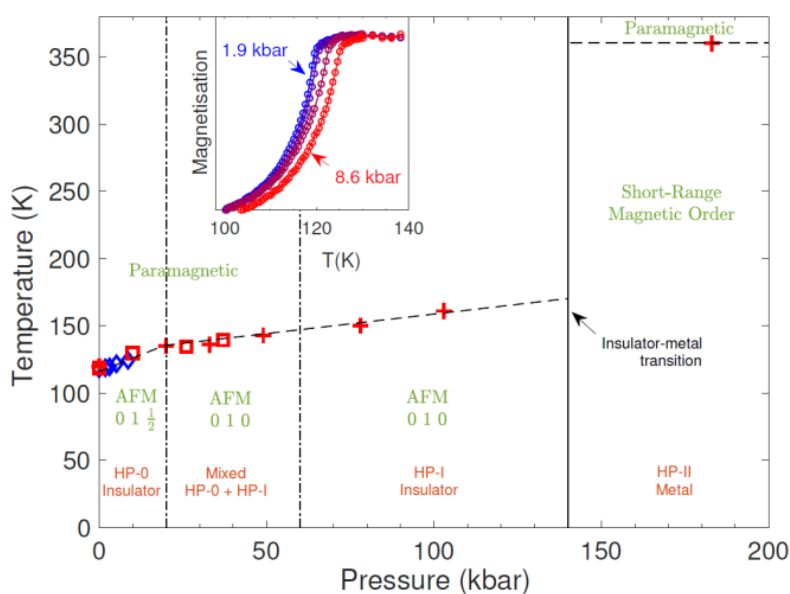
In an expansion on this piece of work Coak et al. [55] present magnetic powder diffraction measurements of the same compound, as well as the magnetic phase diagram uncovered (figure 7.4). They demonstrate several magnetic phase transitions between different antiferromagnetic states. At  $\sim 14$  GPa a transition to a metallic state is accompanied by a transition to a novel magnetic phase, exhibiting short range order.

The application of uniaxial pressure on this compound seems to be an even stronger tool. It would then be possible to ensure that it is indeed only the c-axis that is being

compressed. The pressures discussed here are obviously much higher than the  $\sim 3$  GPa that our pressure cell can achieve. There is however, a likely possibility that the phase diagram will look quite different under uniaxial pressure and with a single crystal sample, so that interesting behaviour is within reach.

In general these van-der-Waals materials seem like obvious candidates for uniaxial pressure studies. This class of compounds exhibit a host of interesting magnetic and electronic properties and their weak out of plane coupling makes them an ideal testing ground for testing the effects of uniaxial pressure.

There is, however, one major issue, I have not been able to find synthesis results of single crystals large enough for neutron scattering and they may not even be possible to synthesise.



**Figure 7.4:** Phase diagram of FePS<sub>3</sub> with hydrostatic pressure as a tuning parameter. The compound undergoes several antiferromagnetic transitions as a function of temperature. Upon metallisation, the long range magnetic order disappears and a short range magnetic order emerges. Figure from [55]

# Chapter 8

## Conclusion

In this thesis, I have presented a design of a uniaxial pressure cell optimized for diffuse, magnetic neutron scattering studies. The cell is capable of achieving pressures of up to 3 GPa with a cylindrical sample with dimensions  $h = 3$  mm and  $d = 3$  mm. I have detailed the calibration process of a load gauge for in situ measurement of the pressure, with an accuracy of around 10 %.

While there are still substantial challenges related to the application of pressure, after some further adjustments of the cell design, it will be ready to be used on neutron beamlines at both the ILL and in the future, the ESS. The work presented here clearly demonstrates that while the pressure dependence of the neutron background is not yet fully understood, the background is largely non-magnetic and homogeneous. This means that the background contribution to the scattering signal can be subtracted, making the cell ideal for studies of diffuse magnetic signals.

Neutron measurements on spin ice material  $\text{Ho}_2\text{Ti}_2\text{O}_7$  show a non-significant change in the peak intensity of  $4 \pm 4$  % as a function of uniaxial pressure. There does, however, seem to be increased scattering from the pinch points, indicating some possible increase in the interaction between the monopole excitation, an effect not described effectively by theory. I believe the reasons that the neutron results have proved rather inconclusive is mainly three things.

First, the experiments were performed while the pressure cell was still under development. This meant that the background from the pressure cell was not well understood, leading to extensive issues with the background subtraction. Additionally, the uncertainty on the applied pressure, made the theoretical modelling quite a lot more difficult.

Second, there is no indication that the samples are able to withstand pressures as high as would be needed to reach the ferromagnetic state proposed by theory. This may be alleviated by finding some way of supporting the sample.

Third, in the second neutron experiment, where the cell background was fairly well understood and a decent background subtraction could be made, the pressure was applied along the (110) direction. Subsequent susceptibility measurements showed that this is the direction where the weakest pressure response would be expected.

Combining these things, it is not very surprising that the neutron experiments have been unable to produce significant agreement with theory. I do, however, believe that the cell is now in a state, where it would be possible to perform the experiments needed to test the theoretical predictions. That is, provided that the samples are able to survive the applied pressure or that a hydrogen-free method for supporting the sample can be found.

# Bibliography

- [1] D. V. Delft and P. Kes. The discovery of superconductivity. *Europhysics News*, 42(1):21–25, 2011.
- [2] W. Heisenberg. Zur Theorie des Ferromagnetismus. *Zeitschrift für Physik*, 49(9-10):619–636, 1928.
- [3] Vinod Kumar Joshi. Spintronics: A contemporary review of emerging electronics devices. *Engineering Science and Technology, an International Journal*, 19(3):1503 – 1513, 2016.
- [4] P. W. Anderson. Resonating valence bonds: A new kind of insulator? *Materials Research Bulletin*, 8:153–160, 1973.
- [5] P. W. Anderson. The resonating valence bond state in  $\text{La}_2\text{CuO}_4$  and superconductivity. *Science*, 235:1196–1198, 1987.
- [6] L. Savary and L. Balents. Quantum spin liquids: A review. *Reports on Progress in Physics*, 80(1), 2017.
- [7] C. Castelnovo, R. Moessner, and S. L. Sondhi. Magnetic monopoles in spin ice. *Nature*, 451:3–6, 2008.
- [8] T. Fennell, P. P. Deen, D. F. McMorrow, S. T. Bramwell, D. Prabhakaran, A. T. Boothroyd, R. J. Aldus, A. R. Wildes, and K. Schmalzl. Magnetic Coulomb Phase in the Spin Ice  $\text{Ho}_2\text{Ti}_2\text{O}_7$ . *Science*, 326(5951):415–417, 2009.
- [9] T. Fennell. Neutron scattering studies of spin ices and spin liquids. *Collection SFN, EDP Sciences*, 04001(13):1–21, 2014.
- [10] L. Balents. Spin liquids in frustrated magnets. *Nature*, 464(7286):199–208, 2010.
- [11] R. Sibille, N. Gauthier, E. Lhotel, V. Porée, V. Pomjakushin, R. A. Ewings, T. G. Perring, J. Ollivier, A. Wildes, C. Ritter, T. C. Hansen, D. A. Keen, G. J. Nilsen, L. Keller, S. Petit, and T. Fennell. A quantum liquid of magnetic octupoles on the pyrochlore lattice. *Nature Physics*, 16(5):546–552, 2020.

- 
- [12] E. Snider, N. Dasenbrock-Gammon, R. McBride, Mathew D., H. Vindana, K. Venkatasamy, K. V. Lawler, A. Salamat, and R. P. Dias. Room-temperature superconductivity in a carbonaceous sulfur hydride. *Nature*, 586(7829):373–377, 2020.
- [13] S. Blundell. *Magnetism in Condensed Matter*. Oxford University Press, first edition, 2014.
- [14] D. C. Mattis. *The theory of magnetism made simple: An introduction to physical concepts and to some useful mathematical methods*. World Scientific, 2006.
- [15] N. D. Mermin and H. Wagner. Absence of ferromagnetism or antiferromagnetism in one- or two-dimensional isotropic Heisenberg models. *Physical Review Letters*, 17(22):1133–1136, 1966.
- [16] C. Lacroix, P. Mendels, and F. Mila. *Introduction to Frustrated Magnetism: Materials, experiments, theory*. Springer, first edition, 2011.
- [17] P. Fazekas and P. W. Anderson. On the ground state properties of the anisotropic triangular antiferromagnet. *Philosophical Magazine*, 30(2):423–440, 1974.
- [18] Y. Okamoto, M. Nohara, H. Aruga-Katori, and H. Takagi. Spin-liquid state in the  $S=1/2$  hyperkagome antiferromagnet  $\text{Na}_4\text{Ir}_3\text{O}_8$ . *Physical Review Letters*, 99:137207, 2007.
- [19] J. S. Gardner, M. J.P. Gingras, and J. E. Greedan. Magnetic pyrochlore oxides. *Reviews of Modern Physics*, 82(1):53–107, 2010.
- [20] M. J. P. Gingras and B. C. den Hertog. Origin of spin-ice behavior in Ising pyrochlore magnets with long-range dipole interactions: an insight from mean-field theory. *Canadian Journal of Physics*, 79(11-12):1339–1351, 2001.
- [21] S. V. Isakov, R. Moessner, and S. L. Sondhi. Why spin ice obeys the ice rules. *Physical Review Letters*, 95:217201, 2005.
- [22] A. P. Ramirez, A. Hayashi, R. J. Cava, and R. Siddharthan. Zero-point entropy in ‘ spin ice ’. *Nature*, 399(110):333–335, 1999.
- [23] D. J.P. Morris, D. A. Tennant, S. A. Grigera, B. Klemke, C. Castelnovo, R. Moessner, C. Czternasty, M. Meissner, K. C. Rule, J. U. Hoffmann, K. Kiefer, S. Gerischer, D. Slobinsky, and R. S. Perry. Dirac strings and magnetic monopoles in the spin ice  $\text{dy}_2\text{ti}_2\text{o}_7$ . *Science*, 326(5951):411–414, 2009.



- [24] I. Mirebeau and I. N. Goncharenko. Spin ice and spin liquid under pressure up to 8.6gpa: A powder neutron diffraction study of  $\text{R}_2\text{Ti}_2\text{O}_7$  (R=tb, ho). *Physica B: Condensed Matter*, 350(1):250 – 253, 2004. Proceedings of the Third European Conference on Neutron Scattering.
- [25] R. Edberg, L. Ørdu Sandberg, I. M. Bergh Bakke, M. L. Haubro, L. C. Folkers, A. Wildes, O. Zaharko, M. Guthrie, A. T. Holmes, M. H. Sørby, K. Lefmann, P. P. Deen, and P. Henelius. Dipolar spin ice under uniaxial pressure. *Physical Review B*, 100(14):144436, 2019.
- [26] M. Mito, S. Kuwabara, K. Matsuhira, H. Deguchi, S. Takagi, and Z. Hiroi. Uniaxial pressure effects on spin-ice compound  $\text{Dy}_2\text{Ti}_2\text{O}_7$ . *Journal of Magnetism and Magnetic Materials*, 310(2 SUPPL. PART 2):2006–2008, 2007.
- [27] L. D. C. Jaubert, J. T. Chalker, P. C. W. Holdsworth, and R. Moessner. Spin ice under pressure: Symmetry enhancement and infinite order multicriticality. *Phys. Rev. Lett.*, 105:087201, 2010.
- [28] Nist, neutron scattering lengths and cross sections. <https://www.ncnr.nist.gov/resources/n-lengths/>.
- [29] R. Edberg, I. M. B. Bakke, H. Kondo, L. Ø. Sandberg, M. L. Haubro, M. Guthrie, A. T. Holmes, J. Engqvist, A. Wildes, K. Matsuhira, K. Lefmann, P. P. Deen, M. Mito, and P. Henelius. Effects of uniaxial pressure on the spin ice  $\text{Ho}_2\text{Ti}_2\text{O}_7$ . *Phys. Rev. B*, 102:184408, Nov 2020.
- [30] A. Ghasemi, A. Scheie, J. Kindervater, and S. M. Koohpayeh. The pyrochlore  $\text{Ho}_2\text{Ti}_2\text{O}_7$ : Synthesis, crystal growth, and stoichiometry. *Journal of Crystal Growth*, 500(August):38–43, 2018.
- [31] S. W. Lovesey. *Theory of neutron scattering from condensed matter*. Clarendon, 1984.
- [32] T. Willis and C. J. Carlile. *Experimental neutron scattering*. Oxford University Press, 2009.
- [33] T. Chatterji. *Neutron scattering from magnetic materials*. Elsevier, 2006.
- [34] K. Lefmann. *Neutron Scattering: Theory, Instrumentation and Simulation*. Lecture notes, 2017.
- [35] G. L. Squires. *Introduction to the theory of thermal neutron scattering*. Cambridge University Press, 2012.

- [36] M. F. Collins. *Magnetic critical scattering*. Oxford series on neutron scattering in condensed matter 4. Oxford University Press, 1989.
- [37] J. R. Stewart, P. P. Deen, K. H. Andersen, H. Schober, J.-F. Barthélémy, J. M. Hillier, A. P. Murani, T. Hayes, and B. Lindenau. Disordered materials studied using neutron polarization analysis on the multi-detector spectrometer, D7. *Journal of Applied Crystallography*, 42(1):69–84, Feb 2009.
- [38] D7 - Diffuse Scattering Spectrometer. <https://www.ill.eu/users/instruments/instruments-list/d7/description/instrument-layout/>.
- [39] Benny Lautrup. *Physics of Continuous Matter: 2nd*. CRC Press, 2012.
- [40] N. J. Simon, E. S. Drexler, and R. P. Reed. *Properties of copper and copper alloys at cryogenic temperatures*. U.S. Dept. of Commerce, Technology Administration, National Institute of Standards and Technology, 1992.
- [41] Bill Toulas. Aisi 316 stainless steel: Specification and datasheet. <https://www.engineeringclicks.com/aisi-316-stainless-steel/>. Visited: 21/11/2020.
- [42] Sverdrup Steel. Titanium grade 2. <https://www.sverdrupsteel.com/products/products-titanium-grade-2>. Visited: 25/11/2020.
- [43] AZO materials. Tungsten carbide - an overview. <https://www.azom.com/properties.aspx?ArticleID=1203>. Visited: 21/11/2020.
- [44] Kmr strain gauge-based force washer for monitoring tasks. <https://www.hbm.com/en/2423/kmr-force-washer-for-force-monitoring-tasks/>, Jun 2020.
- [45] M. L. Haubro. Design and calibration of uniaxial pressure cell for neutron scattering. Project Outside the Course Scope, U.Cph., 2019.
- [46] Tokyo Measuring Instruments Lab. Cryogenic temperature strain gauges cf-series. [https://tml.jp/eng/documents/strain\\_gauge/CFseries.pdf](https://tml.jp/eng/documents/strain_gauge/CFseries.pdf). Visited: 25/11/2020.
- [47] Tokyo Measuring Instruments Lab. Strain gauge adhesives. [https://www.tml.jp/eng/documents/strain\\_gauge/adhesive\\_list.pdf](https://www.tml.jp/eng/documents/strain_gauge/adhesive_list.pdf). Visited: 25/11/2020.
- [48] Wheatstone bridge circuit and theory of operation. <https://www.electronics-tutorials.ws/blog/wheatstone-bridge.html>, Oct 2018.

- [49] Quantumx mx840b/mx440b: Universal data acquisition module. <https://www.hbm.com/en/2129/quantumx-mx840b-8-channel-universal-amplifier/>, Feb 2020.
- [50] R.J Corruccini and J.J Gniewek. *Thermal expansion of technical solids at low temperatures*. USGPO, 1961.
- [51] Material properties: Beryllium copper. [https://trc.nist.gov/cryogenics/materials/BerylliumCopper/BerylliumCopper\\_rev.htm](https://trc.nist.gov/cryogenics/materials/BerylliumCopper/BerylliumCopper_rev.htm).
- [52] Compute neutron attenuation and activation. <https://www.ncnr.nist.gov/instruments/bt1/neutron.html>.
- [53] Clifford W Hicks, Mark E Barber, Stephen D Edkins, Daniel O Brodsky, Andrew P Mackenzie, and Andrew P Mackenzie. Piezoelectric-based apparatus for strain tuning Piezoelectric-based apparatus for strain tuning. *Review of Scientific Instruments*, 065003(June 2014), 2019.
- [54] M. J. Coak, D. M. Jarvis, H. Hamidov, C. R. S. Haines, and P. L. Alireza. Tuning dimensionality in van-der-Waals antiferromagnetic Mott insulators TMPS<sub>3</sub>. *Journal of Physics: Condensed Matter*, 2019.
- [55] M. J. Coak, D. M. Jarvis, H. Hamidov, A. R. Wildes, J. A. M. Paddison, C. Liu, C. R. S. Haines, N. T. Dang, N. T. Kichanov, B. N. Savenko, S. Lee, M. Kratochvilova, S. Klotz, T. Hansen, D. P. Kozlenko, J.-G Park, and S. S. Saxena. Tuning dimensionality, magnetism and conduction in van-der-waals mott insulators, Oct. 2020. Talk given at the ESS-ILL Topical Workshop on Chemistry and Magnetism.

# Appendix A

## List of Publications

### Published

- Dipolar spin ice under uniaxial pressure.  
R. Edberg, L. Ørduk Sandberg, I. M. Bergh Bakke, M. L. Haubro, L. C. Folkers, L. Mangin-Thro, A. Wildes, O. Zaharko, M. Guthrie, A. T. Holmes, M. H. Sørby, K. Lefmann, P. P. Deen, and P. Henelius  
[Phys. Rev. B 100, 144436 \(2019\)](#)
- Effects of uniaxial pressure on the spin ice  $\text{Ho}_2\text{Ti}_2\text{O}_7$   
R. Edberg, I. M. B. Bakke, H. Kondo, L. Ørduk Sandberg, M. L. Haubro, M. Guthrie, A. T. Holmes, K. Matsuhira, J. Engqvist, A. Wildes, K. Lefmann, P. P. Deen, M. Mito, and P. Henelius  
[Phys. Rev. B 102, 184408 \(2020\)](#)

### Submitted

- Classical spin liquid or extended critical range in  $\text{h-YMnO}_3$ ?  
S. Janas, J. Lass, A. Tutueanu, M. L. Haubro, C. Niedermayer, U. Stuhr, G. Xu, D. Prabhakaran, P. P. Deen, S. Holm-Dahlin, and K. Lefmann  
**Submitted to PRL**

### Under Preparation

- Design, calibration, and performance of a uniaxial pressure cell for neutron scattering  
L. Ø. Sandberg, M. L. Haubro, R. Edberg, I. M. B. Bakke, M. Guthrie, A. T. Holmes, L. Mangin-Thro, A. Wildes, J. Oechsle, K.-E. Nielsen, D. W. Wistisen, K. Theodor, P. Henelius, K. Lefmann and P. P. Deen

# Appendix B

## CuBe Properties

The alloy used for the cell is CuBe 25 AT (c17200), this alloy contains 1.8 - 2.0 % Beryllium and approximately 98 % Copper, with small Co, Ni and Fe impurities. The mechanical properties can be found in figure B.1. The pressure cell has been heat treated for 3 hours at 315°C.

**Wertetabelle - Bänder**

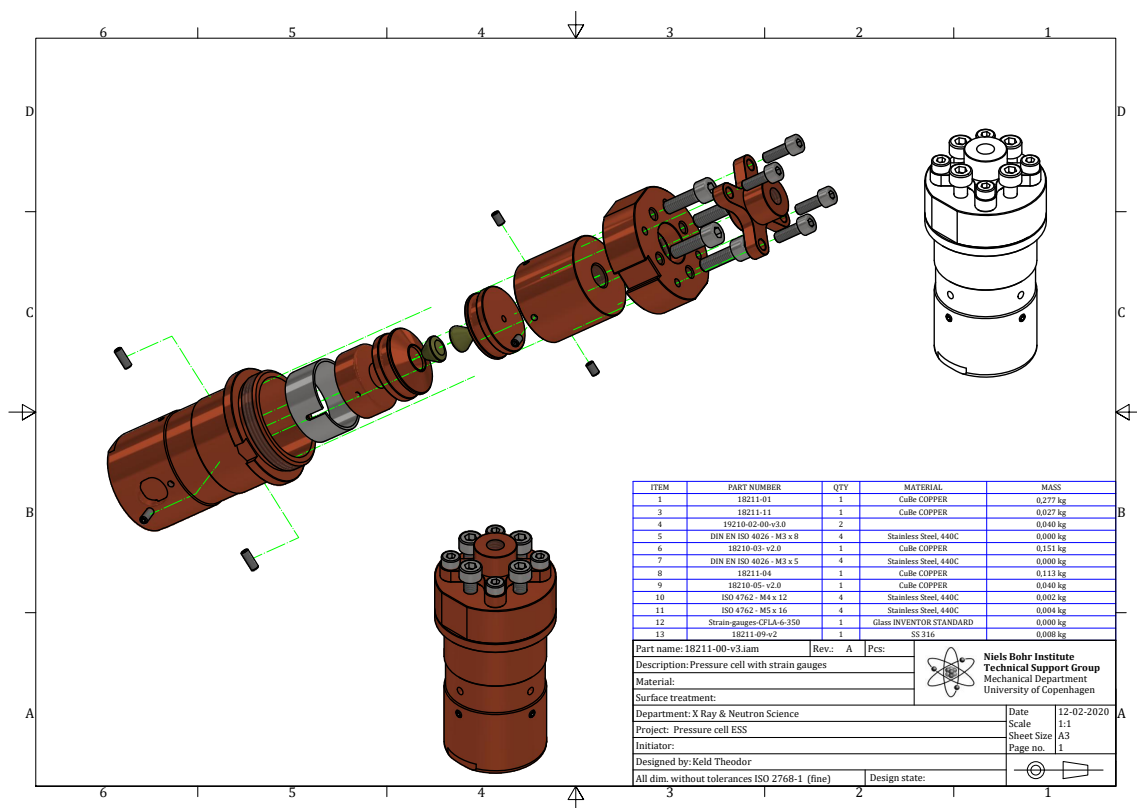
Zustand	Werkstoffnummer EN	Werkstoffnummer DIN	Wärmebehandlung bei (h)/(°C)	Zugfestigkeit Rm [N/mm <sup>2</sup> ]	Dehngrenze Rp 0,2 [N/mm <sup>2</sup> ]	Federbiegegrenze $\sigma_{FB}$ min. N/mm <sup>2</sup> für Dicken (mm)* 0,10-0,25 / 0,25-1,0	% Dehnung A ML=50 mm	Vickers Härte (HV)	Elektrische Leitfähigkeit ( $\frac{\sigma}{\sigma_{min}}$ ) <sup>z</sup>	Verformbarkeit RS Verhältnis 90° Quer/Parallel
<b>Brush Legierung 25 CuBe 2, W.Nr.2.1247.CW 101 C</b>										
<b>vor dem Aushärten</b>										
A R 410	2.1247.40	-	410 - 540	190 - 380	- / -	35 - 60	90 - 150	9	0,0 / 0,0	
1/4 H R 510	2.1247.54	-	510 - 610	420 - 560	- / -	10 - 35	130 - 190	9	0,0 / 0,0	
1/2 H R 580	2.1247.55	-	580 - 690	530 - 660	- / -	8 - 25	180 - 220	8	0,8 / 1,5	
H R 680	2.1247.56	-	680 - 830	650 - 800	- / -	2 - 8	215 - 270	8	2,5 / 5,0	
<b>nach dem Aushärten (vom Kunden)</b>										
AT R 1130	2.1247.60	3 h / 315	1130 - 1350	960 - 1210	780 / 830	3 - 10	350 - 410	13	- / -	
1/4 HT R 1190	2.1247.74	2 h / 315	1190 - 1420	1050 - 1300	820 / 910	3 - 6	360 - 430	13	- / -	
1/2 HT R 1270	2.1247.75	2 h / 315	1270 - 1490	1100 - 1350	880 / 980	1 - 5	370 - 440	12	- / -	
HT R 1310	2.1247.76	2 h / 315	1310 - 1520	1150 - 1420	920 / 1020	1 - 3	380 - 450	12	- / -	

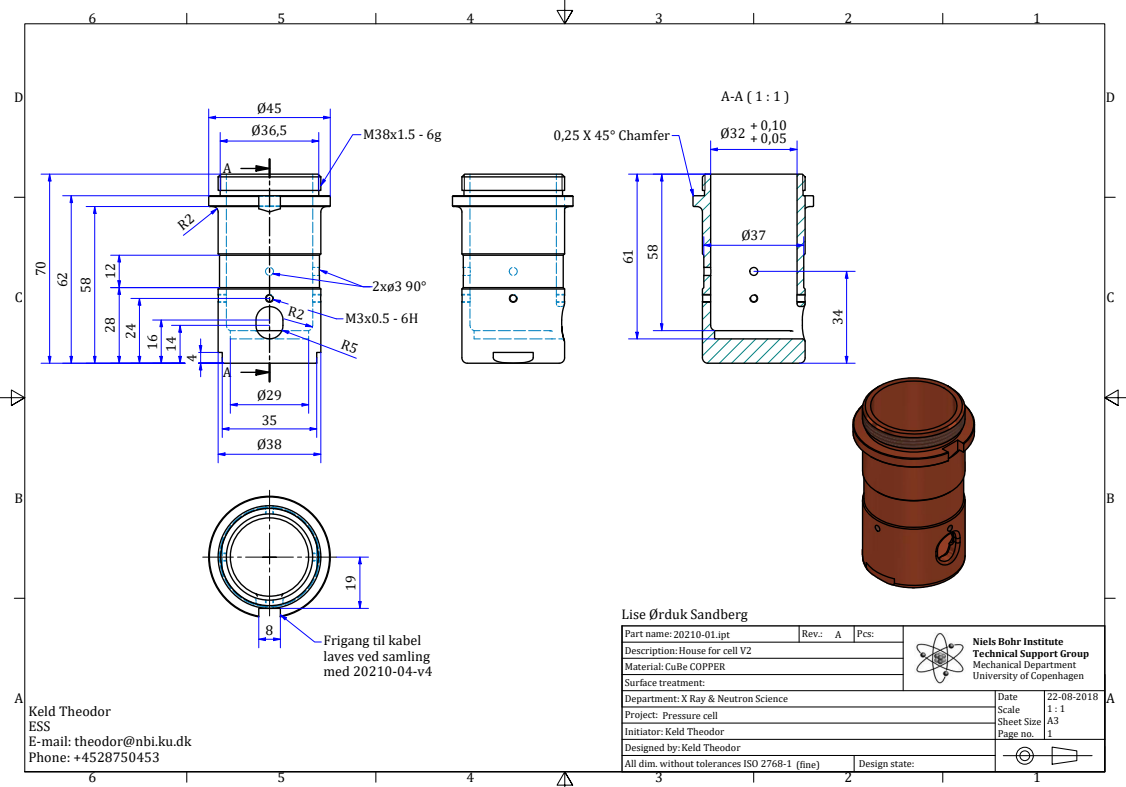
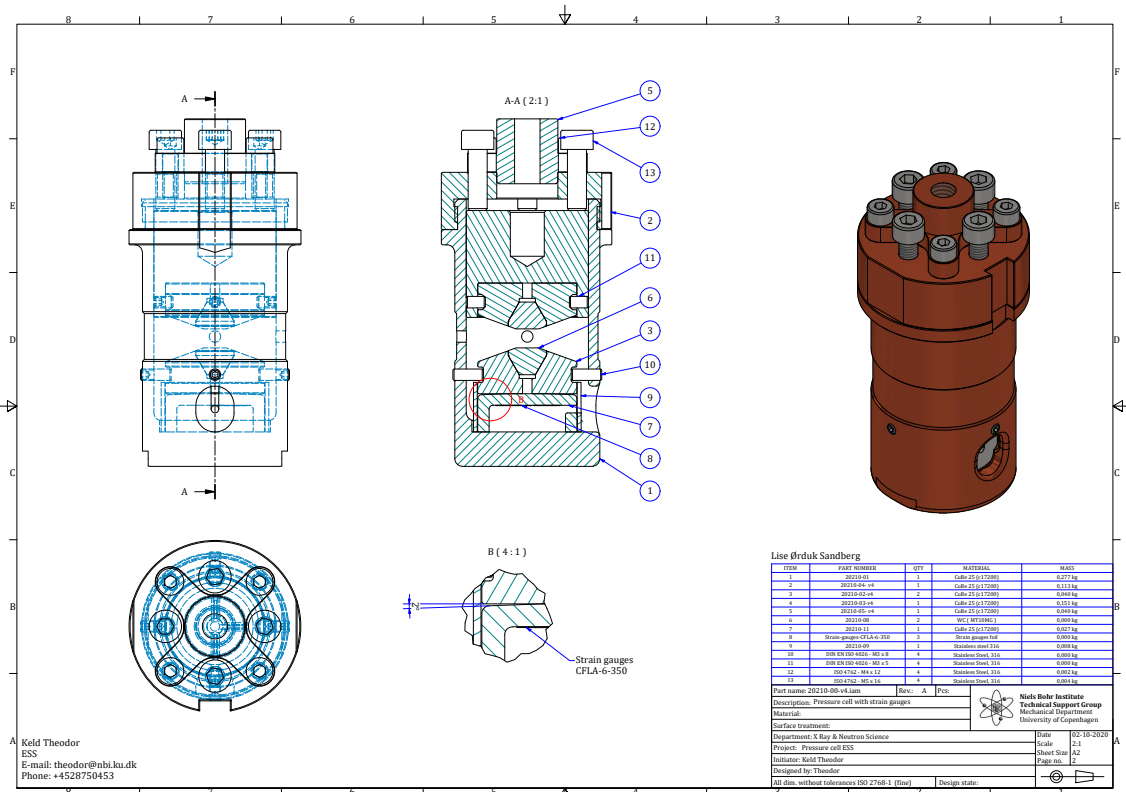
**Figure B.1:** Copper Beryllium properties, the alloy used is marked in red.

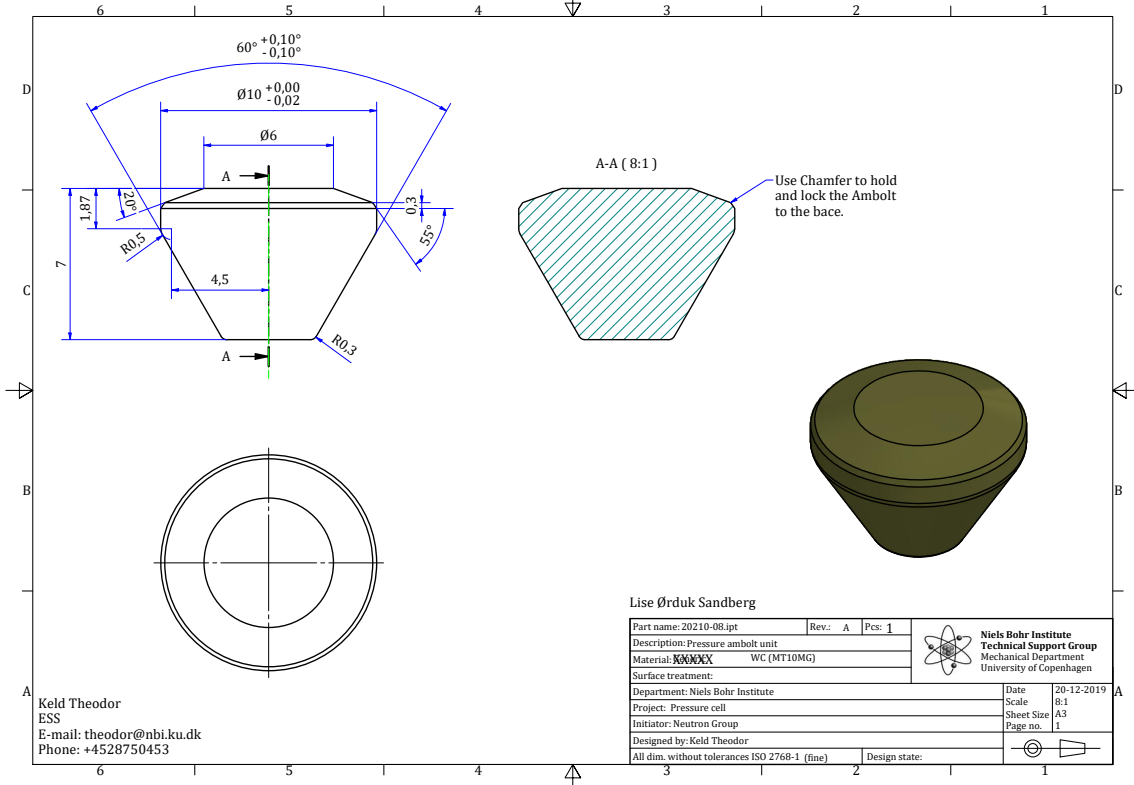
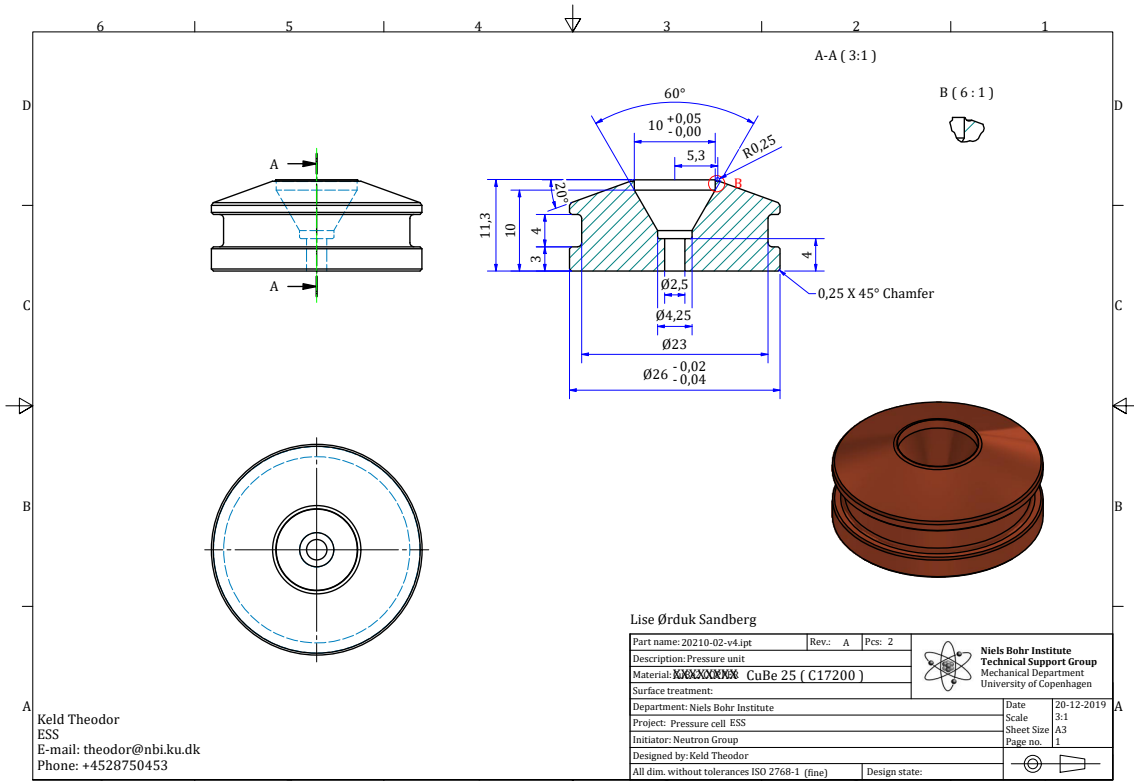
# Appendix C

## Cell Drawings

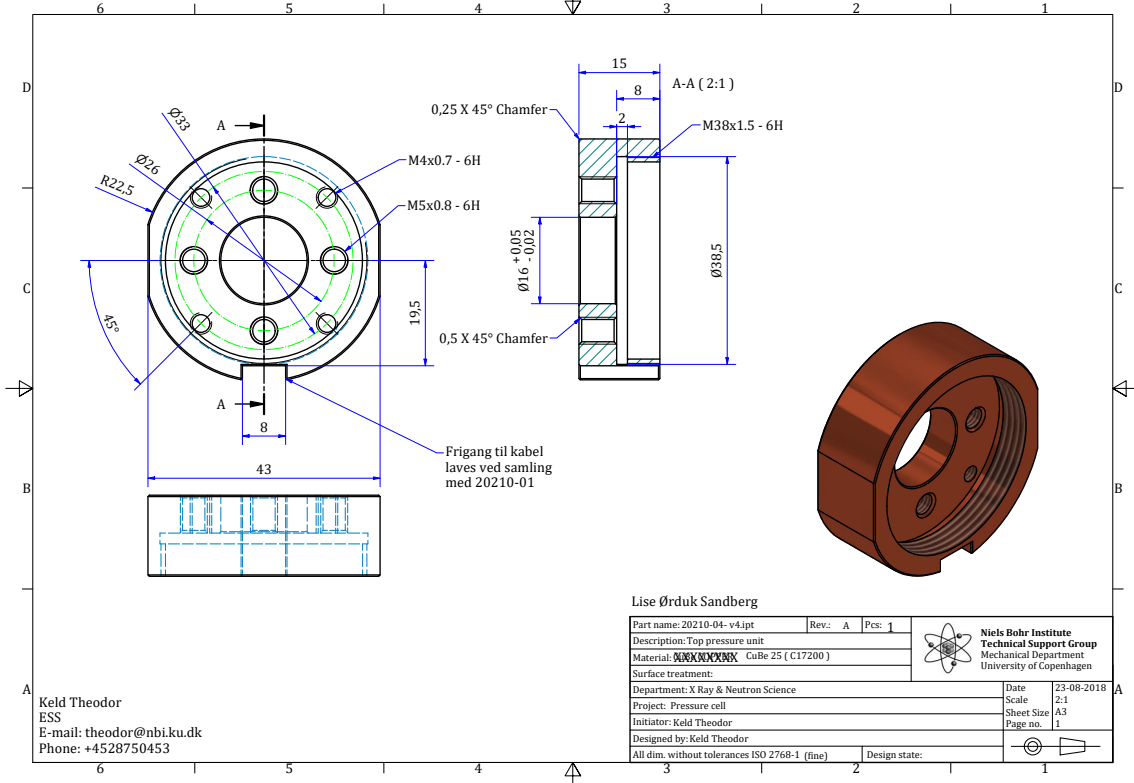
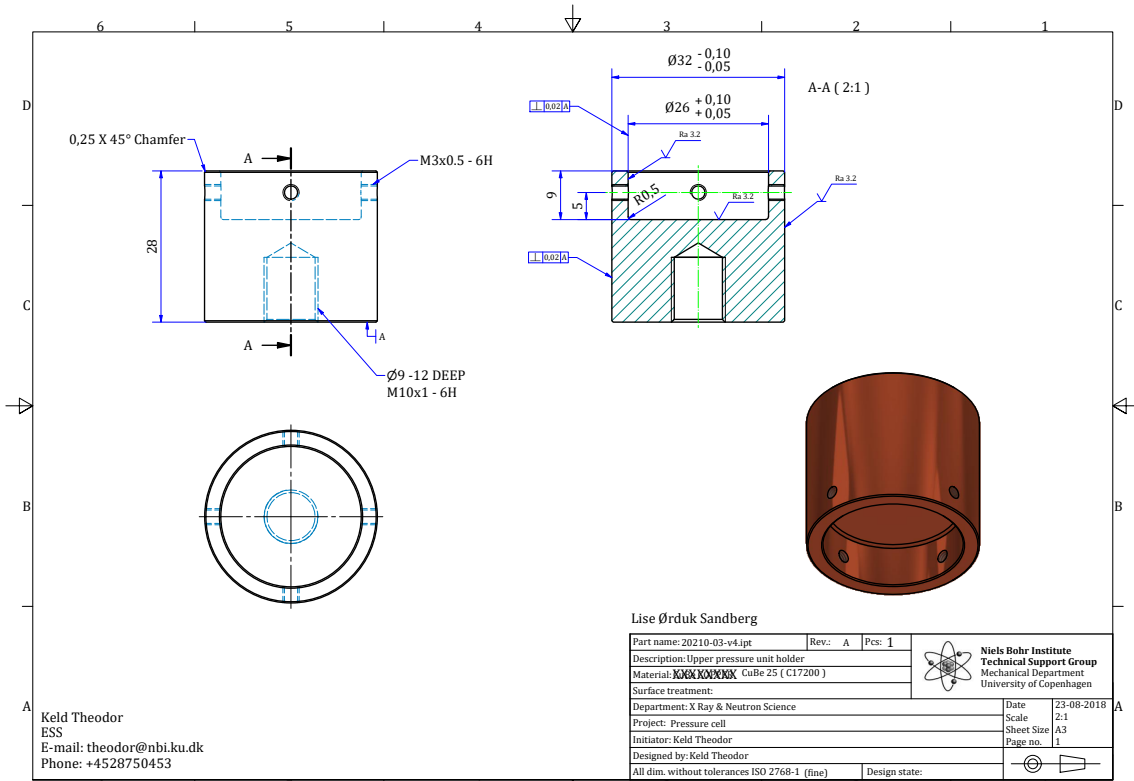
The drawings here have been made by Keld Theodor and the designs have been realised by the workshop at NBI.

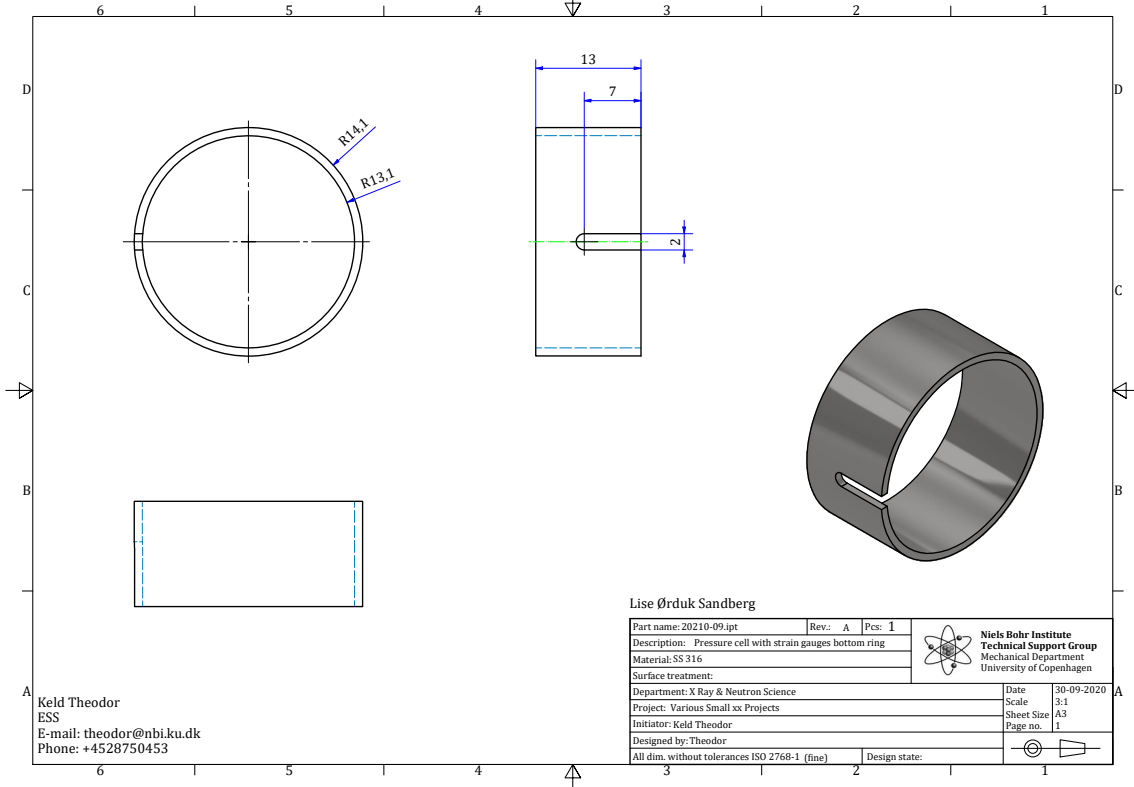
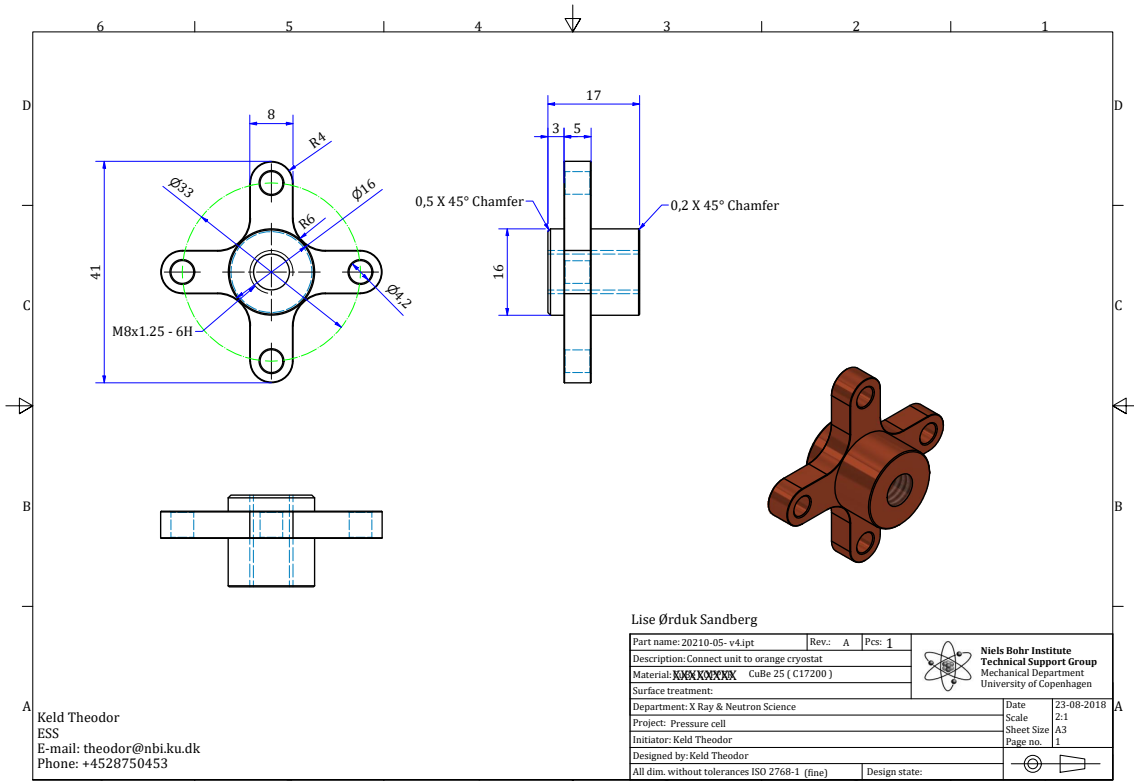


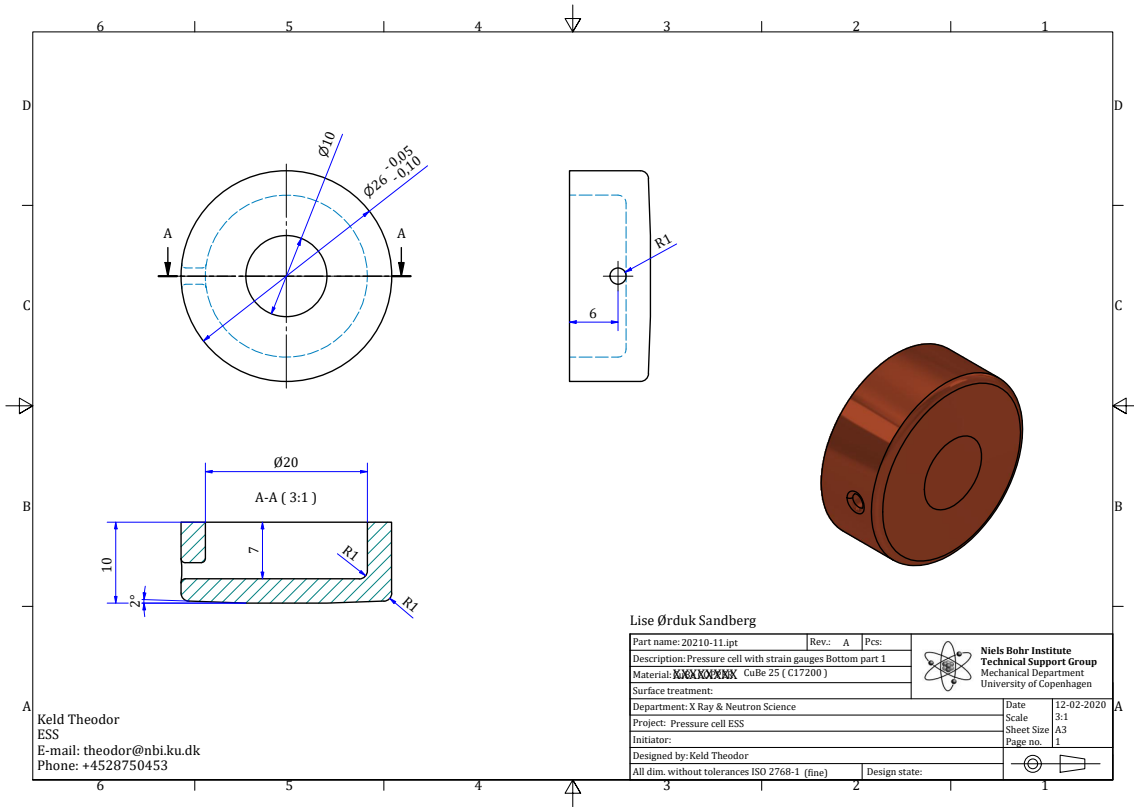







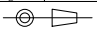






Keld Theodor  
 ESS  
 E-mail: theodor@nbi.ku.dk  
 Phone: +4528750453

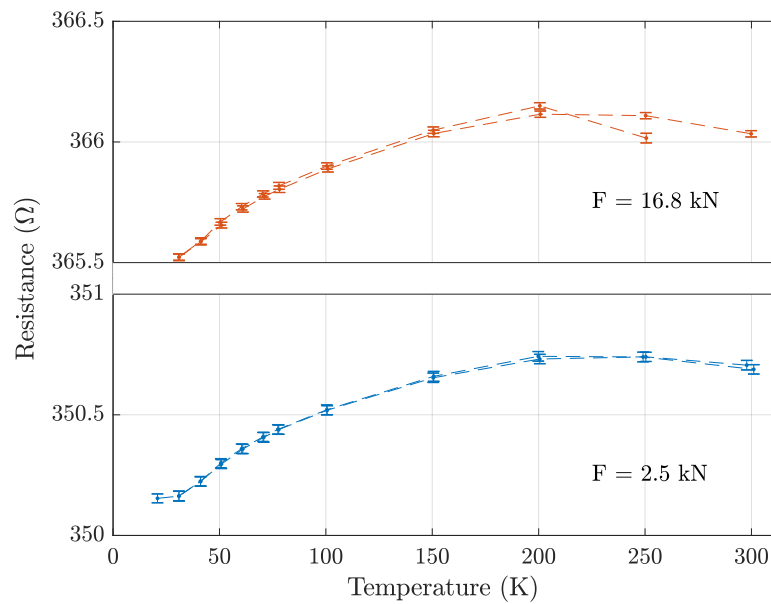
Lise Ørduik Sandberg

Part name: 20210-11.ipt	Rev.: A	Pcs:	 <b>Niels Bohr Institute</b> <b>Technical Support Group</b> Mechanical Department University of Copenhagen
Description: Pressure cell with strain gauges Bottom part 1			
Material: <del>CuBe 25</del> CuBe 25 ( C17200 )			
Surface treatment:			
Department: X Ray & Neutron Science	Date:	12-02-2020	
Project: Pressure cell ESS	Scale:	3:1	
Initiator:	Sheet Size:	A3	
Designed by: Keld Theodor	Page no.:	1	
All dim. without tolerances ISO 2768-1 (fine)		Design state:	

# Appendix D

## Resistance Calibration

Measurements of the total resistance of the Wheatstone bridge was done in the CCR. The resulting curves corroborate the assumption that the resistivity of the strain gauges has a small temperature dependence. The measurements are presented in figure D.1. The resistance change of the bridge over the entire temperature range is  $\sim 0.5\Omega$ , corresponding to  $\sim 0.1\%$ .



**Figure D.1:** Resistance as a function of temperature, during the first measurement, the gauge was loaded to 2.5 kN, during the second it was loaded with 16.8 kN. Both of these were the initial forces at room temperature.